Computational Modeling of Arteriovenous Fistula Hemodynamics in Pulmonary Hypertension Patients

By
Kaitlin Southern
July 2023
Directed by: Stephanie George, Ph.D.
Department of Engineering

In the United States, approximately 50 million people suffer from chronic kidney disease, which over time progresses to end-stage renal disease (ESRD). Care for these patients is typically managed by dialysis with the surgical creation of an arteriovenous fistula. Even though fistula formation is a common and an effective treatment it has been suggested as a risk factor for developing pulmonary hypertension (PH). The objective of this research was to understand the relationship between fistula and pulmonary artery hemodynamics in patients with pulmonary hypertension. The completion of this objective was achieved through three aims: 1) develop protocol for creating subject-specific computational fluid dynamics (CFD) models of fistulas in patients with PH; 2) correlate fistula hemodynamics with clinical measures of pulmonary hypertension; and 3) investigate impact of fistula banding on fistula hemodynamics. Magnetic resonance images (MRI) of the fistula were obtained and processed to build a model of the fistula using Mimics software. Velocity measurements from MRI were used as boundary conditions for the CFD model. The model was then meshed, and the 3D velocity field was solved using ANSYS Workbench. Fistula data, geometric and hemodynamic, was compared with clinical data from the pulmonary artery, amongst the same patient. Multiple mini studies were performed during this project including geometry length comparisons, boundary condition comparisons, and fistula banding comparisons. For the preliminary geometry length comparison study, a shortened model

was chosen and utilized throughout the duration of the simulations for reduced computational cost with little to no effect on the results. For the boundary condition comparison study, the split flow outlet condition was deemed the most physiologically accurate, but minor differences were observed between the split flow and pressure with targeted mass flow rate simulations. Zero pressure outlet conditions were found to be physiologically inaccurate and do not depict realistic flow. Computational arteriovenous fistula results indicated areas of low wall shear stress and recirculation along the anastomosis may cause endothelial dysfunction and fistula failure. Additionally, high output fistulas may lead to cardiac overload and elevated pulmonary artery pressures, from increased venous return and cardiac output. Lastly, the banding comparison study was able to mimic the role of fistula banding by restricting excessive flow and diverting more flow distally. It was concluded that the flow management technique's effectiveness depends on the band's size and location. This project presented a unique opportunity to study both the pulmonary artery and fistula within the same patient, simultaneously. Eventually, this type of modeling will provide insight to the link between fistulas and pulmonary hypertension; thus, identifying key monitoring parameters. Improved monitoring will allow physicians to intervene; thereby preventing the development of pulmonary hypertension.

Computational Modeling of Arteriovenous Fistula Hemodynamics in Pulmonary Hypertension Patients

A Thesis
Presented to the Faculty of the Department of Engineering
College of Engineering and Technology
East Carolina University

In Partial Fulfillment of Requirements for the Degree
Master of Science in Biomedical Engineering

By
Kaitlin Southern
July 2023

Director of Thesis: Stephanie George, Ph.D.

Thesis Committee Members:

Ali Vahdati, Ph.D.

Veeranna Maddipati, M.D.

ACKNOWLEDGEMENTS

This work was supported in part by the Division of Research, Economic Development, and Engagement, and the Undergraduate Research and Creative Achievement Award at East Carolina University. I would like to additionally acknowledge Constantin B. Marcu, MD for image acquisition; Veeranna Maddipati, MD for his pulmonary artery and arteriovenous fistula expertise; Keith Thomson for the constant technical support; the prospective patients for their involvement in the study; Dr. Ali Vahdati for his computational modeling proficiency and strong words of encouragement; and Dr. Stephanie George for continuously providing wisdom and support throughout my time at East Carolina University.

TABLE OF CONTENTS

LIST OF TABLES

LIST OF FIGURES

LIST OF ABBREVIATION

2D – Two-Dimensional

3D – Three-Dimensional

4D – Four-Dimensional

AVF – Arteriovenous Fistula

CFD – Computational Fluid Dynamics

CKD – Chronic Kidney Disease

CO – Cardiac Output

CT – Computed Tomography

DE – Transthoracic Doppler Echocardiography

ESRD – End-Stage Renal Disease

FEA – Finite Element Analysis

FSI – Fluid Structure Analysis

GFR – Glomerular Filtration Rate

IRB – Institutional Review Board

mPAP – Mean Pulmonary Artery Pressure

MRI – Magnetic Resonance Imaging

NIH – Neointimal Hyperplasia

OSI – Oscillatory Shear Index

PA – Pulmonary Artery

PC – Phase-Contrast

PCWP – Pulmonary Capillary Wedge Pressure

PH – Pulmonary Hypertension

PVR – Pulmonary Vascular Resistance

RHC – Right Heart Catheterization

SVR – Systemic Vascular Resistance

sPAP – Systolic Pulmonary Artery Pressure

TAWSS – Time-Averaged Wall Shear Stress

TR – Tricuspid Regurgitant

VR – Venous Return

WSS – Wall Shear Stress

CHAPTER 1. INTRODUCTION

1.1 Overview and Proposed Work

Over 15% of adults in the United States have chronic kidney disease (CKD) caused by permanent structural damage to the kidneys that results in impaired renal function defined by a glomerular filtration rate (GRF) ≤ 60 mL/min [1]. As this condition progresses, kidney function will continue to suffer. Once a patient's GFR falls below 15 mL/min, individuals are classified as having reached end-stage renal disease (ESRD). The most common form of disease management for ESRD patients is replacement therapy. Hemodialysis accounts for over 64% of renal replacement therapy plans and requires creation of an arteriovenous fistula (AVF) [2]. While dialysis can work indefinitely to prolong patient's lives, serious comorbidities can develop during this treatment. One of these conditions is pre-capillary pulmonary hypertension (PH), clinically diagnosed by a mean pulmonary artery pressure (mPAP) ≥ 20 mmHg [4]. Several recent studies have explored connections between matured AVFs and pre-capillary PH development in ESRD patients. Recent clinical research studies observed a PH prevalence of 40% in hemodialysis patients with fistulas [3]. However, there is conflicting evidence in the available literature pertaining to this problem. This work will ultimately provide physicians with clinically useful parameters for monitoring fistulas in patients at risk of developing PH. These parameters may help physicians more closely monitor problematic fistulas requiring surgical intervention to limit their size and flow rates and in turn may lead to a decrease in PH prevalence for ESRD patients. Prevention of PH is crucial not only for elevated arterial pressure, but also because end stage renal disease patients with pulmonary hypertension may be removed from the kidney transplant list.

1.2 Thesis Organization

Chapter 1 of this document provides an overview of the project and an outline for the proceeding sections. Chapter 2 contains anatomy and physiology pertaining to chronic kidney disease, end stage renal disease, and pulmonary hypertension; screening techniques for diagnosing pulmonary hypertension; applications of computational fluid dynamics; and a literature review of arteriovenous fistula hemodynamic modeling. Chapter 3 provides the methodology for patient recruitment and selection, image analysis and geometry formation, velocity waveform creation, transient model set up and analysis, and validation. Chapter 4 presents the results discovered using this methodology. Chapter 5 discusses the results and significance of the findings, limitations, and future directions of the project. Lastly, Chapter 6 concludes the thesis work. A list of references, supplemental tables, and IRB documentation will follow.

CHAPTER 2. BACKGROUND

This section serves as an overview of kidney anatomy and physiology, chronic kidney disease and end stage renal disease, and possible treatment protocols. It will also discuss pulmonary hypertension development, screening techniques for diagnosing pulmonary hypertension, and clinical implications of using computational fluid dynamics to model arteriovenous fistulas. Additionally, the effects of elevated pulmonary artery (PA) pressures will be explored, as well as diagnosis criteria for pulmonary hypertension patients.

2.1 Kidney Anatomy and Physiology

The renal system is comprised of two kidneys, ureters, a bladder, and urethra for the passage, storage, and release of urine. The kidneys, shown in Figure 2.1, are located behind the peritoneum, at the back of the abdominal cavity, where the right kidney lies slightly lower than the left, due to the position of the liver [5]. The kidneys, covered by a fibrous capsule, serve to filter blood received from the descending aorta, renal artery, and renal arterioles and provide a stable environment for tissue and cell metabolism by balancing water transport, excreting waste products, conserving nutrients, and regulating acid-base balance in the body [5].

Blood delivered to the kidneys flows into the encapsulated glomerulus and is either filtered through a nephron or continues flowing through a connected arteriole. A nephron, shown in Figure 2.2, is the working filtration unit of a kidney, with approximately 400,000 to 800,000 nephrons present within each kidney, however this number progressively declines with age [5].

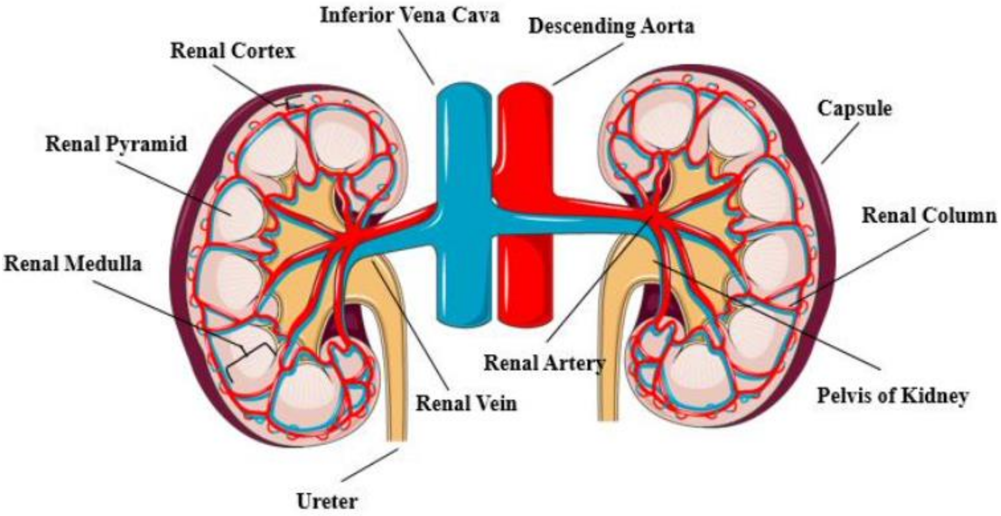

Figure 2.1. Human kidney anatomy.

This image was taken from Servier Medical Art by Les Laboratoires Servier under a Creative Commons License [6]. License available at: https://creativecommons.org/licenses/by/3.0/us/legalcode.

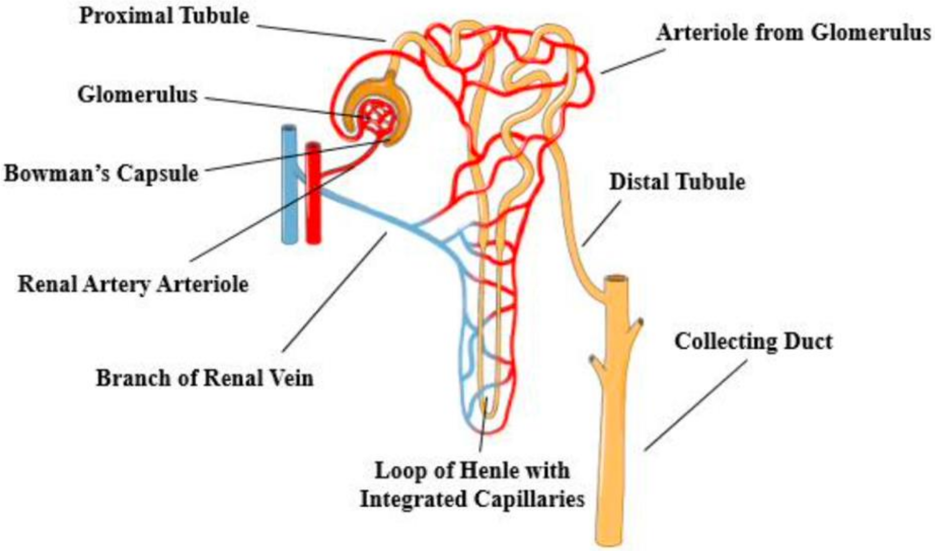

Figure 2.2. A nephron.

This image was taken from Servier Medical Art by Les Laboratoires Servier under a Creative Commons License [6]. License available at: https://creativecommons.org/licenses/by/3.0/us/legalcode.

Unfiltered blood initially enters the Bowman's Capsule, a hollow capsule of the tubular epithelium, and flows through the glomerulus, a ball of capillaries. Filtered blood then passes through the proximal convoluted tubule, where ions are absorbed, and into the Loop of Henle for water reabsorption. The blood then flows through the distal convoluted tubule and into the collecting duct, which collects the urine filtrate [5]. Urine flows in the renal pelvis, through the ureter, and is eventually excreted from the bladder.

Kidney performance is typically measured by glomerular filtration rate (GFR) and is defined by the total amount of fluid filtered through all functioning nephrons per unit of time. GFR is either measured by exogenous markers (i.e., DTPA, iohexal), or estimated using equations. For healthy individuals, GFR typically ranges from 90-120 mL/min per 1.73 m^2 [5]. Kidney function can be compromised by diabetes, high blood pressure, and various environmental factors and lifestyle choices.

2.2 Chronic Kidney Disease and End-Stage Renal Disease

More than 15% of adults in the United States are diagnosed with chronic kidney disease, which is caused by structural damage to the kidneys and defined by a GFR $\leq$ 60 mL/min [1]. With continuous worsening of the kidneys, individuals are classified as having end-stage renal disease (ESRD), when their GFR falls below 15 mL/min. Meaning their kidney function is no longer able to sustain life long-term. Complications of CKD and ESRD development include nausea, central nervous system depression, anemia, various cardiovascular disease, and, if unresolved, death [1]. People with CKD are five to ten times more likely to die prematurely than they are to progress to ESRD. Individuals with diabetes, elevated blood pressures, cardiovascular diseases, and genetic predispositions are all at higher risks of developing ESRD; however, the prevalence and progression of CKD and ESRD can vary within countries by ethnicity and social class.

2.3 ESRD Management and Pulmonary Hypertension

ESRD management is a very demanding field, with an estimated cost of $25 billion on care treatments in 2013 [7]. The most common form of treatment plan is replacement therapy, such as total organ transplant, peritoneal dialysis, and hemodialysis, which is the most common. Total organ transplant is the most ideal form of treatment, providing patients with new, functioning kidneys. This method is ultimately limited to the number of donors, where demand usually exceeds supply [7]. Peritoneal dialysis, which involves waste filtration through a catheter from the abdomen, has been seen to have better clinical outcomes than hemodialysis. However, not all patients are eligible for this management option. Resulting in hemodialysis being the most used method for ESRD management [7]. The preferred method of dialysis is typically determined in association with a nephrologist, considering the patient's lifestyle and other medical conditions. Especially for ESRD patients, early nephrological evaluation can allow for timely establishment of a permanent and functioning access.

Hemodialysis requires the surgical creation of an arteriovenous fistula, shown in Figure 2.3, to allow for increased blood flow through a dialysis machine and back to the right side of the heart [2]. Fistulas are created by invasively connecting an artery and a vein.

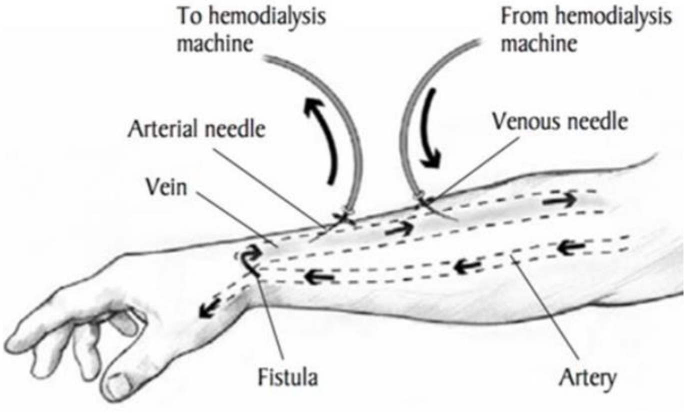

Figure 2.3. Arteriovenous fistula [12].

Radiocephalic fistulas are created by anastomosing the end of the cephalic vein to the side of the radial artery and are recommended as the first choice for fistula creation since it preserves future options for access sites. Most fistulas mature within six weeks of creation and roughly 90% of all AVFs are developed and able to be used for dialysis within eight months of creation [2]. While dialysis can work indefinitely to prolong patient's lives, serious comorbidities can develop during this treatment, one of them being *pulmonary hypertension*.

Healthy individuals tend to have a mean pulmonary arterial pressure (mPAP) between 12-16 mmHg, usually measured using right heart catheterization (RHC) at the base of the PA; pulmonary capillary wedge pressure (PCWP) between 2-14 mmHg, and pulmonary vascular resistance (PVR) less than 1 Woods Unit [8]. PVR, similar to Ohm's Law, is defined by the resistance against blood flow from the PA to the left atrium. PVR is calculated by Equation 1:

$$PVR = \frac{mPAP - PCWP}{CO} \tag{1}$$

Where CO is the cardiac output in L/min. PVR is typically given in Woods units but can be multiplied by 80 to receive units in $\frac{\mathrm{dyn \cdot s}}{\mathrm{cm}^5}$ [8].

As previously stated, PH is diagnosed by right heart catheterization. RHC is an invasive procedure in which a physician guides a special catheter to the right side of the heart. The catheter then passes into the pulmonary artery, where blood pressures are measured along the way. mPAP is measured in the PA, and PCWP is measured in the PA after the catheter balloon is inflated [8]. PCWP is frequently used to access and estimate left ventricle pressure. Using these invasive measurements and individual's cardiac output, PVR can be estimated from Equation 1.

These measurements are especially useful in diagnosing PH and discriminating between PH types; pre-capillary PH, post-capillary PH, and combined PH groups (Groups 1 – 5). The determination is crucial because treatments for Group 1 could be harmful to individuals in other groups [9]. The different PH groups are shown below in Table 2.1. Group 1 PH consists of individuals with pulmonary arterial hypertension or pre-capillary PH, Group 2 PH is PH due to left heart disease, Group 3 PH is PH due to lung diseases, Group 4 PH is caused by PA obstructions, and Group 5 PH is comprised of unclear and multifactorial cases of PH [9]. End-stage renal disease patients fall under PH clinical Group 5, these clinical measurement indicators can be seen in Table 2.1.

Table 2.1. PH classifications [10].

Type	**Clinical Measurement Indicators**	**Clinical Groups**
Pre-Capillary PH	mPAP > 20 mmHg, PCWP ≤ 15 mmHg, PVR ≥ 3 Woods Units	1, 3, 4, and 5
Isolated Post-Capillary PH	mPAP > 20 mmHg, PCWP > 15 mmHg, PVR < 3 Woods Units	2 and 5
Combined Pre- and Post-Capillary PH	mPAP > 20 mmHg, PCWP > 15 mmHg, PVR ≥ 3 Woods Units	2 and 5

In 2003, Yigla et al. [3] observed a PH occurrence of nearly 40% in hemodialysis patients with fistulas, diagnosed by echocardiography. However, echocardiography, which will be discussed further, tends to overestimate the pulmonary pressure [11]. They also found ESRD patients with

PH to have higher cardiac output compared to normotensive patients (6.9 L/min v. 5.5 L/min), leading them to claim that dialysis may promote endothelial dysfunction. The exact causes of developing pre-capillary PH in ESRD patients are unclear, shown with conflicting literature findings. For example, Acarturk et al. [12] and Unal et al. [13] both reported no correlation between AVF blood flow rates and increases in mPAP. While some studies have reported that AVF flow rates are correlated with increased pulmonary artery pressures ($p < 0.001$), insufficient studies have explored connections between fistula creation and performance and the development of PH in ESRD patients. Few to no studies have offered numerical data suggesting a direct connection between fistula and PA hemodynamics in PH patients.

2.4 Screening Techniques for Pulmonary Hypertension

There are many non-invasive methods for screening and detecting pulmonary hypertension. Techniques used include echocardiography, magnetic resonance images (MRI), and 4D MRI. Right heart catheterization, discussed previously, is routinely used, and considered the gold standard for diagnosing PH. However, the procedure is invasive and has significant mortality and morbidity, 0.055% and 1.1%, respectively [14]. This section serves to fully define the alternative ways to screen for pulmonary hypertension.

2.4.1 Echocardiography

The Transthoracic Doppler echocardiography (DE) is the recommended initial screening method for evaluation of PH, because it is non-invasive, safe, and accessible. Echocardiography can be used to determine right-side chamber size and function and the presence of pericardial effusion [15]. DE estimates right ventricular systolic pulmonary artery pressure (sPAP), by calculating the pressure gradient between right ventricular and the right atrium using the modified Bernoulli equation, (Equation 2):

$$sPAP = 4v_{tr}^2 + RAP \tag{2}$$

Where v is the velocity of the tricuspid regurgitant (TR) jet. Estimated right atrial pressure (RAP) is added to this number to equal the sPAP, which is used to diagnose pulmonary hypertension [15]. Due to errors in right atrial pressure estimation and poor imaging of the TR jet, it has been suggested that echocardiography may be inaccurate for estimating PA pressures. In a study with 65 patients, Fisher et al. found that DE was inaccurate 48% of the time. Inaccuracy was defined by greater than ±10 mmHg from the invasive measurement [15]. Shujaat et al. found that DE measurements seemed to differ for patients with severe cases of tricuspid regurgitant and pulmonary hypertension. This is important because significant under and over estimation can lead to misdiagnosis and inappropriate treatment [16]. Augustine et al. suggested DE should be used to estimate the probability of PH rather than estimating pulmonary artery pressures. The outlined approach, seen in Figure 2.4, first considers the peak TR velocity (TRV), where a TRV greater than 3.4 m/s indicates a high probability of PH. If the TRV is less than 3.4 m/s, the probability of PH should be assessed in conjunction with other echocardiographic markers, such as early diastolic pulmonary regurgitation (PR) velocity or PA diameter [17].

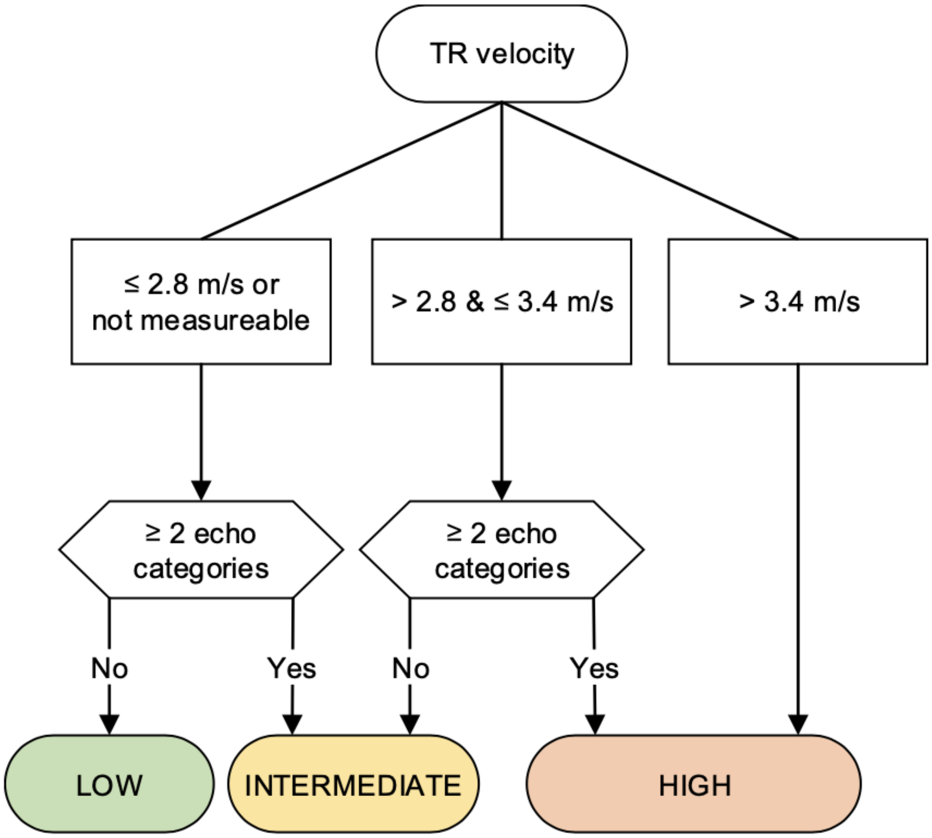

Figure 2.4. Peak TRV approach to predict the probability of PH.

Original image published by Augustine et al. [17] in The Journal of Echo Research and Practice under a Creative Commons Attributions License. Published 2019. No changes were made to this image. License available at: https://creativecommons.org/licenses/by-sa/4.0/legalcode.

2.4.2 Magnetic Resonance Imaging (MRI)

Magnetic resonance imaging has been suggested as an alternative to echocardiography and RHC to screen for pulmonary hypertension, due to its existing use for characterizing right ventricular (RV) anatomy and function, however, is typically limited for research investigations [18]. Johns et. al. performed an analysis study with 300 patients suspected of having pulmonary hypertension that underwent both RHC and MRI. Using a cardiac MRI multiparametric model with parameters such as the interventricular septal angle, ventricular mass index, and black blood slow flow score, the group generated a regression equation ($\mathrm{mPAP} = -179 + \log_e(\text{interventricular septal angle}) \times 42.7 + \log_{10}(\text{ventricular mass index}) \times 7.57 + \text{black blood slow flow score } \times 3.39$) to estimate mPAP with a sensitivity and specificity of 93% and 79%, respectively [19].

Additionally, Lunga et al. (2014) found that MRI measurements taken in the main pulmonary artery (MPA) together with interpretation provided by computational Windkessel models can provide quantitative diagnostic parameters for detecting PH. They discovered statistically significant differences in these parameters for normal patients, mild PH patients, and severe PH patients, and concluded that this methodology could be used to further develop a non-invasive diagnostic test for patients suffering from PH [20]. Years later, Lunga et al. (2016) demonstrated that combining the Windkessel computation-derived metrics (i.e., total pulmonary compliance and distal and characteristic resistance) characterizing hemodynamic changes in the pulmonary vasculature with right ventricular morphology and function (i.e., right ventricle end-diastolic volume index, right ventricle ejection fraction, and ventricular mass index) measures in a decision support algorithm (random forest classification algorithm) provides a method to noninvasively diagnose PH with 92% accuracy [18].

Despite promising results, MRI diagnosis is difficult in patients with PH due to left-sided heart disease, because of non-specific symptoms and the difficulty of interpreting test results. There are further advancements for MRI imaging, including 4D MRI, which can provide additional defined data for characterizing PH.

2.4.3 4D MRI

A recently advanced non-invasive screening method is the four-dimensional (4D) MRI. Although, 4D MRI scanners are not available in most clinics and are primarily seen at research intensive hospitals, which limits widespread accessibility. Compared to traditional MRI, 4D MRI adds a fourth dimension of movement, allowing clinicians to better visualize blood flow. This technique estimates pulmonary vascular resistance using blood flow measurements extracted from 3D velocity-encoded phase contrast magnetic resonance images [21]. PVR is determined by the cross-sectional area of the distal pulmonary vascular bed, and is known to decrease in hypertensive individuals, due to vascular hypertrophy and vasoconstriction. Studies suggest the 4D MRI is a good diagnostic tool for PH due to the assessment of hemodynamic measurements and cardiopulmonary markers [21]. Kheyfets et al. presented an equation to estimate PVR, with $R^2 = 0.94$, obtained from the velocity encoded MRI measurements. Sieren et al. compared 4D and 2D phase contrast MRI between normotensive and hypertensive patients and found good agreement in measurements, such as maximum velocity and flow rate between techniques, despite 4D flow results revealing a considerable spread in measurements. 4D velocity fields of the pulmonary artery, shown in Figure 2.5, indicate a) a normotensive subject with physiological laminar flow and b) a hypertensive subject with a vortex in the main PA, associated with increased mPAP [22].

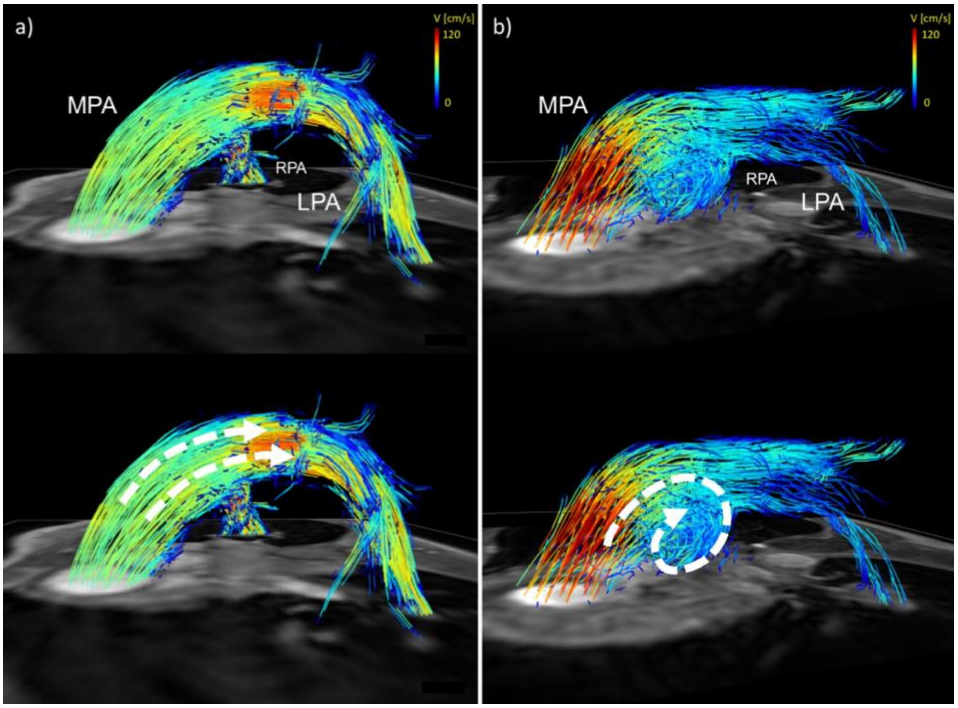

Figure 2.5. 4D MRI of pulmonary artery. a) Normotensive, b) Hypertensive.

Original image published by Sieren et al. [22] in PLoS One under a Creative Commons Attributions License. No changes were made to this image. Published 2019. License available at: https://creativecommons.org/licenses/by-sa/4.0/legalcode.

This method does not require the estimation of TR velocities and is a clear advantage over previous techniques. However, there are large errors in estimating velocity gradients, requiring further research and investigation.

2.5 Computational Fluid Dynamics (CFD)

The section serves to discuss the workflow and applications of computation fluid dynamics models, as well as current limitations and assumptions.

2.5.1 CFD Modeling

Another technique for detecting PH involves modeling patient specific blood flow using computational fluid dynamics. CFD refers to the computer software and algorithms that offer estimated solutions to partially solved Navier-Stokes and continuity equations [23]. CFD software allows for user-defined geometry, fluid properties, and boundary conditions to model continuous fluid flow. CFD uses the following equations (Equation 3, Equation 4), derived from the assumptions that mass and momentum are conserved:

$$\frac{\partial(p)}{\partial t} + \nabla \cdot \left(\rho \vec{V}\right) = 0 \tag{3}$$

$$\rho\left[\frac{\partial \vec{V}}{\partial t} + (\vec{V} \cdot \nabla)\vec{V}\right] = -\nabla p + \nabla \cdot \bar{\bar{\tau}} + \rho \vec{f} \tag{4}$$

Where ρ is density of the fluid, $\vec{V}$ is the velocity vector, p is the pressure, $\bar{\bar{\tau}}$ is the viscous stress tensor, and $\vec{f}$ is the body force per unit mass [24]. These relationships are converted into algebraic expressions and solved element by element through a finite volume method. CFD, or *in silico*, models have immense potential for patient specific medicine that offer more cost effective and timely information than many *in vitro* and *in vivo* experiments [24]. The workflow for CFD projects will be discussed below.

2.5.2 Segmentation

The development of a 3D computational model begins with image acquisition, or medical imaging of the desired anatomy. Various non-invasive image modalities can be used, such as magnetic resonance imaging or computed tomography (CT), that distinguish between tissues and structures by differences in brightness or greyscale. MR images utilize magnetic fields and radio waves to obtain cross-sectional images of a body, whereas CT scans use x-ray images taken at thin cross-sections along the area of interest, forming slices. These scanning images are exported in a

DICOM format, containing image data and patient information. A completed stack of 2D cross-sectional images can be assembled to provide 3D volumetric information. Semi-automatic meshing software such as Mimics, ImageJ, and CVIPTools can be used to create 3D anatomical geometries through a process known as segmentation [25].

Segmentation refers to the process of extracting regions of interest to represent an individual anatomical body, based upon discontinuity or similarity criterion. The process is more closely defined by labeling image pixels based on criterion where those pixels with the same label are connected to form the region of interest, resulting in a patient-specific anatomical structure (i.e., blood vessel, organ). Adjacent pixels not belonging to the desired anatomical body will display values outside of the criterion. Segmentation can be performed manually by selecting individual pixels or automatically through pixel based (thresholding), edge based, or region-based techniques. “Thresholding” identifies the desired anatomical region of interest and “isolation” separates this region from the remaining image [25].

MRI and CT with a contrasting agent is preferred for better reconstruction accuracy, however contrast-enhanced imaging can present risks, such as allergic reactions, exposure to ionized radiation, and damage to the kidneys [26]. Realistically, the accuracy of the segmentation and pixel labeling are limited by the resolution of the image modality, where a large slice thickness can cause the artificial appearance of vessel continuities and incomplete detection of small vasculature. It is important to obtain a slice thickness relative to the size of the anatomical structure of interest to allow for practical clinical implementation [27].

2.5.3 Meshing

After the anatomical body is segmented and constructed, the 3D models can be imported into a software, such as ANSYS Workbench, for meshing or discretization. A mesh is expressed as a number of small finite elements or grid cells, connected to each other by nodes, which overlay an entire domain geometry. The computational domain is divided into many finite elements to solve the equations of motion (Equation 3, Equation 4) using a method known as finite element analysis (FEA) [25].

Meshes can be comprised of tetrahedral, hexahedral, or polyhedral elements. Tetrahedral elements are most common for anatomical structures, particularly because hexahedral elements are not practical for capturing small pulmonary vasculature with many bifurcations, leading to exceptionally large or exceedingly small aspect ratios. Multiple layers of prism or wedge elements can be applied around the edges of body, known as inflation or boundary layers, to estimate fluid wall mechanisms and wall sheer stresses (WSS) more accurately [25].

Mesh quality is assessed by two metrics: skewness and orthogonal quality, both ranging from 0 to 1. As seen in Figure 2.6, a mesh with excellent quality is suggested to have a mean skewness from 0 to 0.25 and mean orthogonal quality from 0.95 to 1.00. Additionally, the maximum skewness should never exceed 0.95 and minimum orthogonal quality should not fall below 0.1 [25].

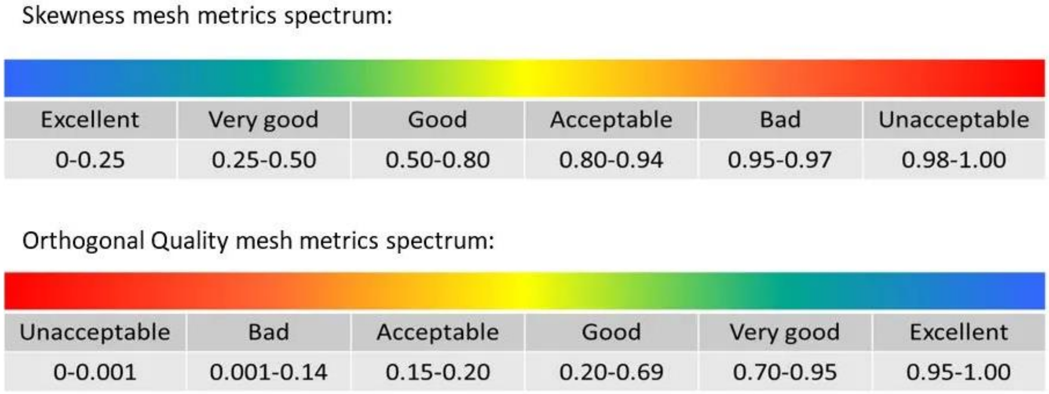

Skewness mesh metrics spectrum:

Excellent	Very good	Good	Acceptable	Bad	Unacceptable
0-0.25	0.25-0.50	0.50-0.80	0.80-0.94	0.95-0.97	0.98-1.00

Orthogonal Quality mesh metrics spectrum:

Unacceptable	Bad	Acceptable	Good	Very good	Excellent
0-0.001	0.001-0.14	0.15-0.20	0.20-0.69	0.70-0.95	0.95-1.00

Figure 2.6. Mesh metrics [28].

A mesh independence analysis should be performed to ensure that the results of an analysis are independent of the size of the mesh. The best method to test for mesh independence is to gradually refine or coarsen the mesh, and then compare the results (i.e., WSS) and plot the difference [29]. At least three significantly different mesh sizes, usually a factor of 1.5 times the element size, should be tested. It is ideal to achieve values that do not change with an increase in mesh size [25]. After achieving a quality mesh, models can be imported into software capable of solving the partial continuity and momentum equations.

2.5.4 Boundary Conditions

After importing discretized geometries into a CFD analysis software, such as Fluent, boundary conditions are applied. Boundary conditions include mass flow rates, velocity waveforms, and flow split or pressure outlets. Patient specific inlet waveforms can be obtained invasively through right heart catheterization or noninvasively with phase-contrast (PC) MRI or echocardiography. Outlet conditions for patient-specific models usually include mass flow rate outlets, pressure outlets, and outflow boundary conditions. Zero traction outlets allow for users to set each outlet pressure to a constant value; however, this can result in nonphysiologically flow, with the flow split directed solely by the segmented geometry and ignoring downstream resistance [25]. To accurately represent flow dynamics, the pressure and flow should be coupled at each outlet, achieved by applying pure resistance outflow boundary conditions. This type of boundary condition does not account for distal vasculature compliance, keeps pressure and flow in phase, and ensures mass conservation is kept [27]. Lastly, a more complex outflow condition, the three-element Windkessel model, accounts for the upstream resistance and the resistance and compliance of the downstream vasculature. Additionally, vessel walls are assumed to be rigid, meaning no deformation occurs, and nonslip, where the velocity of the fluid at the wall is zero in magnitude.

Deformations of the vessel wall can be studied using fluid structure interaction (FSI) modeling [30].

2.5.5 Fluid Properties

Fluid properties also need to be defined for the fluid domain before approximating the solution. Viscosity is a material-dependent property and refers to the fluids' ability to resist deformation under shear forces. Fluids with constant viscosity are characterized as Newtonian, and fluids, such as blood, with varying viscosity are defined as non-Newtonian. However, hemodynamic studies usually characterize blood as an incompressible and Newtonian fluid with constant viscosity, 3.2 cP, and density, 1060 kg/m•s [25]. When velocity is constant, blood behaves as a Newtonian fluid, but when large velocity fluctuations occur blood cells deform and impact viscosity. The viscosity is also influenced by vessel diameter and the shear stresses caused by the walls. A decrease in vessel diameter causes a gradual decrease in blood viscosity, however the effect on red blood cells is not significant and viscosity remains relatively constant, allowing us to classify blood as Newtonian in computational studies [27].

2.5.6 Solver Preferences

In computational modeling, two solver technologies are available: pressure-based, and density-based. The solvers differ based on the method the continuity, momentum, and (if applicable) energy equations are approximated. Pressure-based solvers are typically used for incompressible fluids, and when blood is assumed to be incompressible, whereas density-based solvers grant better accuracy for high-speed compressible fluids. For pressure-based solvers, a pressure-velocity coupling method or pressure-based segregated algorithm is set. Multiple options are available such as Semi-Implicit Method for Pressure Linked Equations (SIMPLE) and Pressure Implicit with

Split Operator (PISO). Users must also determine the time step size, total number of time steps, and the iterations per time step [31]. An adequate number of iterations is needed to sufficiently reach convergence. Convergence is frequently determined by the level of residuals, the amount by which the partial differential equations are not satisfied, or simply the error in the solution [32]. Residual levels of 1×10^{-4} are considered loosely converged, 1×10^{-5} well converged, and 1×10^{-6} tightly converged. However, convergence is deemed sufficient by the analyst [33].

2.5.7 Post Processing and Parameters of Interest

When blood flows through the vessels, stresses are placed along the walls and endothelial lining. There are two types of superficial stresses near the vessel walls: 1) circumferential stress, which is due to the pulse pressure change within the vessel, and 2) shear stress or wall shear stress, which is created by the tangential force of blood flowing against the vessel wall [34]. Shear stresses at arterial walls range from 10 to 70 dynes/cm^2, with lower shear stresses found in the veins, at 1 to 6 dynes/cm^2. Elevated WSS can cause increases in the thickness of vessel walls and increased flow velocity, where decreased WSS is frequently associated with turbulent flow, regions of blood circulation, vortex formation, and ‘stagnant’ blood areas. In regions of anastomoses, thrombosis or hyperplasia have been seen, primarily due to the presence of low wall shear stress [34].

WSS is calculated based on the velocity profile near the wall; where most imaging modalities do not have sufficient spatial resolution to capture this profile [35]. Thus, a benefit to CFD is the ability to capture the time varying WSS which has important physiologic implications linking mechanics to biology. Since these parameters (i.e., WSS) can be estimated non-invasively by MRI or echocardiography, connections can be established to allow physicians to monitor AVF use and the development of pulmonary hypertension more effectively.

2.5.8 Computational Limitations

CFD analysis provides many advantages as described before; however, there are errors and limitations associated with the technique. Computational methods provide numerical approximations of the model, meaning an exact answer is not reached. The estimated solution is dependent upon a series of initial user-defined approximations. The imported patient specific geometries help to provide more clinically relevant solutions but are still limited by the spatial resolution of imaging machines, such as MRIs [36]. Also, boundary conditions are limited by knowledge about the specific mechanical properties of the vasculature being studied. Computational power to run these simulations is also another limitation, such as limited processing and storage capabilities. Model validation and verification is necessary to ensure accurate and reliable CFD simulation results.

2.6 Existing Models of Arteriovenous Fistulas

Computational fluid dynamics has been widely used to model idealized and patient specific AVFs. Modeling has focused on human patients with some groups incorporating animal subjects into their simulations. The following section will summarize existing models of arteriovenous fistulas, which will later be compared to identify limitations and literature gaps.

Many studies have indicated that high wall shear stress along the AVF walls causes vessel wall stiffness. the development of neointimal hyperplasia (NIH), and fistula failure.

Pike et. al created CFD models of AVF blood flow in two mice models, due to their availability of high-resolution hemodynamics characterization. The hollow AVF geometry was constructed using non-contrast two dimensional T2-weighted fast spin echo MR images [37]. Time dependent blood inflow and outflow rates were extracted from the gradient echo velocity mapping sequence. Blood was characterized with standard density and viscosity values, walls were assumed to be rigid, and no- slip conditions were applied [37]. Using the extracted data, CFD modeling was performed and blood flow velocity and hemodynamics factors including wall shear stress, spatial averaged wall shear stress (SPWSS), oscillatory shear index (OSI), and various volumetric properties (i.e., vorticity, helicity, and Q-criterion) were analyzed [37]. The results indicated increased AVF flow velocity, WSS, SPWSS, and OSI for AVF three weeks-post, compared to presurgical intervention [37]. At 21 days post-operative, the velocity and WSS reached maximum values of approximately 50 cm/s and 200 dyne/cm^2, respectively, compared to maximums of approximately 4 cm/s and 10 dyne/cm^2 in the non- surgery veins [37]. Post-operative characteristics, such as flow disturbances, were also seen to increase, indicated by the increased volumetric properties. Additionally, this group reported increased levels of both blood recirculation and vortex formation in AVF veins [37]. WSS color maps, comparing AVF and nonsurgical controls, can be seen in Figure 2.7.

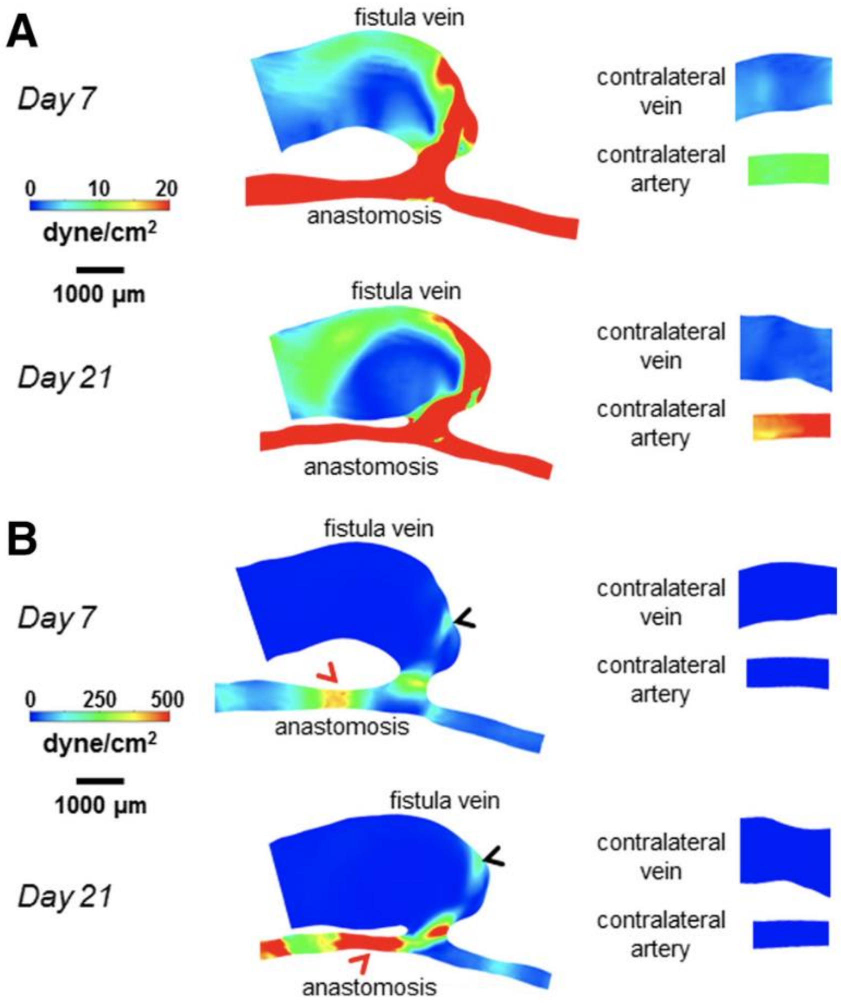

Figure 2.7. Wall shear stress in mouse AVF [37].

Carroll et al. investigated the shear forces and hemodynamic properties within a constructed geometry of a mature patient specific AVF using CFD modeling. The 3D AVF geometry was compared to a patient with a healthy vein geometry, both created using a series of 2D MRI scans [38]. In contrast to the Pike et al. study, flow waveforms obtained from echocardiography were used as inlet flowrate conditions, which have been shown to have good agreement with flow rate information from phase-contract MRI [37, 38]. CFD analysis was conducted, and results showed a significant increase in mean flow velocity entering the vein of the AVF and high wall shear stress gradients [38]. The mean cross-sectional area, inlet velocity, and WSS for the AVF was 317.1 mm^2, 620 mm/s, and 3.311 Pa, respectively, compared to 8.6 mm^2, 31.4 mm/s, and 0.14 Pa, respectively for the health vein. This group theorized that vessel remodeling and continuous non-physiologically elevated WSS can lead to AVF stenosis development. This theory was supported by Manos et al. who found that high wall shear stress, and high WSS gradients are related to vessel wall stiffening and NIH or thickening and narrowing of the vessel walls [39].

Additionally, Van Tricht et al. studied hemodynamic differences in arteriovenous fistula grafts between a straight 6 mm graft and a tampered 4-7 mm graft. Three-dimensional geometries of a forearm vascular access were created in SolidWorks and discretized in Gambit 2.0.4. A periodic velocity signal was assigned at the arterial inlet and a periodic pressure waveform at the outlet, achieving a flowrate of 1000 ml/min [40]. Post processing was executed with ANSYS Fluent and in-house MATLAB files. Results indicated physiologically high WSS levels (>3 Pa), found in the critical range for stenosis development in both AVF geometries. These zones that reached extreme hemodynamic values correspond to locations of NIH formation in literature [40].

Despite these findings that support high WSS leading to fistula failure, many studies have found that low wall shear stress, as a result of recirculating flow, is at fault for stenosis and neointimal hyperplasia development.

The most significant longitudinal study was carried out by Sigovan et al. who investigated the changes in hemodynamic parameters during AVF development, to improve the understanding of fistula maturation. The group utilized MRI sequence images from three patients to create the AVF geometry and extract velocity and flowrate data for boundary conditions [41]. CFD simulations were completed, and results showed decreased wall shear stresses post AVF creation. From the initial point until 3 months post operation patient 1 observed a 31.4 Pa to 9 Pa decrease in WSS, patient 2 a 51 to 11 Pa decrease, and no considerable change in mean WSS values was observed for patient 3 (108.4 to 110.3 Pa). Additionally, Sigovan et al. observed that disturbed flow and levels of recirculation in the outflow vein were associated with non-uniform vessel remodeling and stenosis development in areas of low WSS [41]. Clinically, only one fistula was determined mature (patient 1) and the other two fistulas failed after 3 months. Comparison of the velocity streamlines and WSS contours for patient 1 can be seen in Figure 2.8. From top to bottom: 5 days, 1 month, 3 months. The cross sections were taken at the anastomosis (a), in the swing segment (b), and in the vein portion of the swing segment (c).

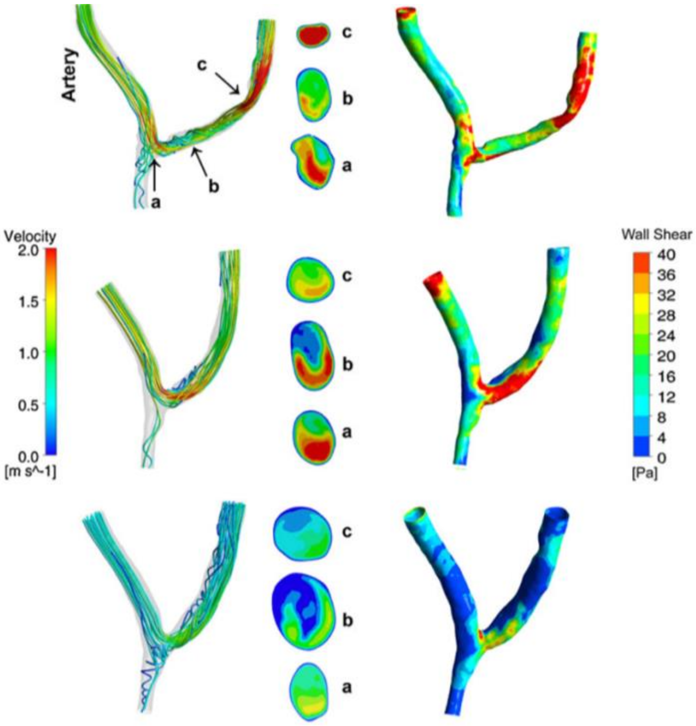

Figure 2.8. Decreased WSS post AVF creation.

Reprinted by permission from Springer Nature: Springer, Annals of Biomedical Engineering, *Vascular Remodeling in Autogenous Arterio-Venous Fistulas by MRI and CFD* by Sigovan et al. [41]. Copyright 2012, Published 2012. No changes were made to this image.

Jia et al. observed the effects of WSS in 20 canine subjects with ‘end to side’ AVFs, surgically created between the right femoral artery and vein [42]. Three-dimensional models were segmented from Phillips ultrasound scanning images, 28 days post-operation. A fine, unstructured tetrahedral mesh was generated in ICEMCFD. Velocity boundary conditions we;8e set at the proximal artery and vein, and a flow boundary condition was placed at the distal artery. Modeling was performed in ANSYS Fluent using the finite element method and a second order upwind scheme [42]. Computational wall shear stress and velocity results were compared to intima-media thickening measurements in the vessel. Similar to Sigovan et al., results indicated that neointimal hyperplasia was associated with low and disturbed WSS sites (along the inner proximal vein wall) compared to areas of high or laminar WSS (along the outer proximal vein wall) [41]. Jia et al. found NIH is not only affected by WSS, but also flow patterns [42].

Bozzetto et al. observed the transition from laminar to turbulent flow, developing in the anastomotic vein of an AVF [43]. MR images from a single 39-year-old human patient were used to reconstruct the AVF geometry using the Orobix Vascular Modeling Toolkit package. The patient had a distal radiocephalic AVF surgically created in the forearm. The model was discretized using meshing software from Open FOAM 4 software suite. Volumetric flowrate information was extracted from MR scans and was applied as boundary conditions at the proximal artery (inlet) and distal artery (outlet). A zero-traction boundary condition was assigned to the proximal vein (outlet) [43]. The walls were assumed to be rigid, and non-slip conditions were applied. Blood was assumed to be non-Newtonian using the Bird-Carreau rheological model [43]. The researchers found recirculation levels in low-WSS regions and a decreased level of WSS (0-0.2 mmHg) in the venous segment of the AVF.

These results were also supported by Ene-Iordache et al. who found localization of low and oscillating shear stress in post-operative flow conditions, potentially triggering the formation of NIH with subsequent increase of wall thickness and stenosis development [44]. Connections between velocity and areas of recirculation and stenosis development can be seen in Figure 2.9.

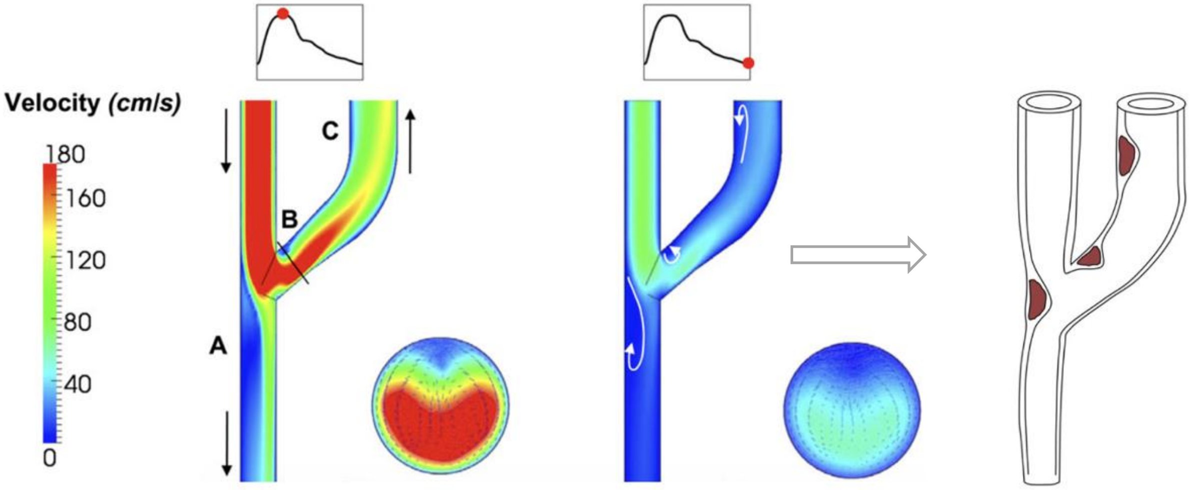

Figure 2.9. Velocity measures and their connection to stenosis development.

Reprinted by permission from Oxford University Press, Nephrology Dialysis Transplantation, *Disturbed flow in radial-cephalic arteriovenous fistulae for haemodialysis: Low and oscillating shear stress locates the sites of stenosis* by Ene-Iordache et al. [44]. Copyright 2011, Published 2012. Figures were combined to compare fistula flow hemodynamics and stenosis development.

Geometry reconstructions were created based on intraoperative measurements taken by Sivanesan et al. using duplex and color-flow ultrasonography [45]. A velocity waveform boundary condition was set at the proximal artery inlet and flow split outflow conditions were assigned at the proximal vein and distal artery (81% PV, 19% DA) [44].

A few studies have found both high and low wall shear stress to contribute to stenosis development and fistula failure.

One in particular, Kim et al. studied AVF models with three different anastomotic angles; 20^o, 30^o, and 40^o. 3D modeling was performed in Design Modeler and a structured mesh was generated with ICEMCFD using the finite element method [46]. The mesh was comprised of 351,584 elements and 323,907 nodes. Blood was characterized as Newtonian and modeled using the Carreau model, with viscosity defined as a function of shear rate. The inflow and outflow boundary conditions were applied with clinical blood flow data, and the walls were assumed non-slip and rigid. Recirculation flow, low WSS, and high OSI were found in the venous anastomosis segment in the 30^o and 40^o models [46]. Additionally, areas of recirculation, high WSS, and high OSI were found in all models. They concluded that a higher anastomosis angle in the venous segment causes stenosis development, but stenosis along the arterial side occurs regardless of the anastomosis angle [46].

2.6.1 Summary of Existing AVF Models

Overall, research done to characterize hemodynamics in AVFs has drawn three main conclusions. The first conclusion, supported by Pike et al., Carroll et al., Manos et al., and Van Tricht et al., is that an increase in overall WSS, or high WSS gradients, during fistula maturation is associated with vasculature remodeling and stenosis development, leading to fistula failure [37-40]. This draws a second conclusion; it appears that blood flow velocity and WSS decrease in the venous segments of AVFs following creation, supported by Sigovan et al., Jia et al., Bozzetto et al., and Ene-Iordache et al. [42-46]. Additionally, this research has revealed that areas of low WSS are subjected to elevated blood recirculation, which may lead to impaired endothelial function. Lastly, a third conclusion simply states that both low and high values of WSS lead to stenosis development and NIH formation. The following table, Table 2.2, is helpful for summary and comparison of the literature previously discussed.

Table 2.2. Summary of arteriovenous fistula models [47].

Group	Relevant Findings
Pike et al. (2017) [37]	Post-operative increases in flow disturbances and vortices with elevated WSS and WSS gradients
Carroll et al. (2011) [38]	High shear stress, elevated WSS gradient and reversed flow can lead to venous NH development and vascular access failure
Manos et al. (2010) [39]	High shear stress and high WSS gradient correlate with areas of NIH development and vessel wall stiffening
Van Tricht et al. (2006) [40]	Found a correlation between areas of high shear and the locations of NIH formation
Sigovan et al. (2013) [41]	Low wall shear stress occurred at zones of recirculating flow, correlating with stenosis development
Jia et al. (2015) [42]	NIH was more obvious in areas of low/disturbed shear compared to areas that experienced high shear
Bozzetto et al. (2016) [43]	Concludes that the occurrence of transitional flow can lead to the development of AVF stenosis
Ene-Iordache et al. (2012) [44]	Found that areas exposed to low/oscillating shear and multidirectional flow correlate closely with sites of potential stenosis
Kim et al. (2012) [46]	Supports findings that recirculating flow, low shear, high shear and high OSI lead to stenosis

2.6.2 Limitations and Literature Gaps

Considering the existing computational models presented above, there are limitations and numerous opportunities for improvement. There are conflicting opinions in literature about the underlying cause of pulmonary hypertension development and involvement of AV fistula flow rates and wall shear stresses. The most noticeable area of improvement in the literature is the comparison of AV fistula and pulmonary artery modeling results of the same patient within the same session. No studies to date have looked specifically at AVF CFD modeling and PH. Modeling hemodynamics in both anatomical structures can help to reveal a trend between high output (defined in this study as those with flow rates greater than 1.5 L/min) fistulas and the development of pulmonary hypertension in ESRD patients. To reveal this connection, trends must be found between hemodynamic properties in AVFs and PAs of ESRD patients. Should a correlation be found, parameters can be provided to physicians to help monitor fistulas and allow for the detection of PH. This can allow physicians to take early surgical precautions to prevent the development of hypertensive conditions. Early precautionary measures can help ESRD patients remain on the kidney donor list, and inevitably reduce the health disparities associated with ESRD.

CHAPTER 3. METHODS

This section defines the specific aims of study, the methods used to develop patient-specific models, and the process to compare and evaluate the results from the proposed study. IRB acquisition will also be discussed due to human subject involvement in the study.

3.1 Aims of Study

Overall, the purpose of this project was to provide physicians with clinically useful parameters for identifying problematic AVFs to decrease the prevalence of PH. With the ability to achieve this objective, there is hope for ESRD patients to have better healthcare opportunities and inevitably prevent their removal from the kidney transplant list. To achieve this goal, there were three aims to be considered during the completion of the study:

1. Develop a protocol for creating subject-specific computational fluid dynamics (CFD) models of fistulas in patients with PH;
2. Correlate fistula hemodynamics with clinical measures of PH;
3. Investigate the impact of fistula banding on fistula hemodynamics.

These aims were chosen to drive the project's completion and ultimately advance literature on this clinical issue. Further explanation of the relationship between patients with arteriovenous fistulas and the development of pulmonary hypertension will be assessed by analyzing fistula hemodynamic estimations and right heart catheterization clinical measurements.

3.2 IRB Approval

This study was approved by the East Carolina University Internal Review Board (IRB) (UMCIRB 19-000708). The IRB Approval can be viewed in Appendix B. Precautions were put into place to ensure no more than minimal risk was presented to the patients. Enrolled patients were given a subject ID. Personally identified information was removed from imaging data and clinical data obtained from medical records. All data was stored on a password protected and secure network drive (Piratedrive).

3.3 Inclusion Criteria and Subject Recruitment

The inclusion criteria for this study were as follows: patients must be over the age of 18, have an arteriovenous fistula actively being used for dialysis, have been diagnosed with PH by right heart catheterization (RHC), have no contraindications for MRI, have not been diagnosed with connective tissue disease, and do not have advanced left heart disease. The target prospective patient recruitment was five ($n = 5$) patients however, due to the COVID-19 pandemic, the study was able to achieve one (n=1) prospective patient enrolled to date.

3.4 Image Acquisition

The prospective patient underwent MR imaging with a Siemens Aera 1.5 Tesla MR machine, located at ECU Health Hospital. No contrast agent was used during this imaging session. Scans were completed of the fistula to obtain geometry and velocities in the proximal arterial and venous segments. Additional scans of the pulmonary artery and cardiac measures were obtained. During this procedure, the subject lied in the supine position and held their breath while imaging was completed. An example image can be seen in Figure 3.1. For the pulmonary artery and fistula, the slice thickness was 8 mm with no gaps between slices, allowing 22 slices to be collected. An echo time of 1.34 ms was used, with a repetition time of 289.5 ms. Pixel spacing was 1.61 mm. This series of images were used to recreate the geometry of the fistula.

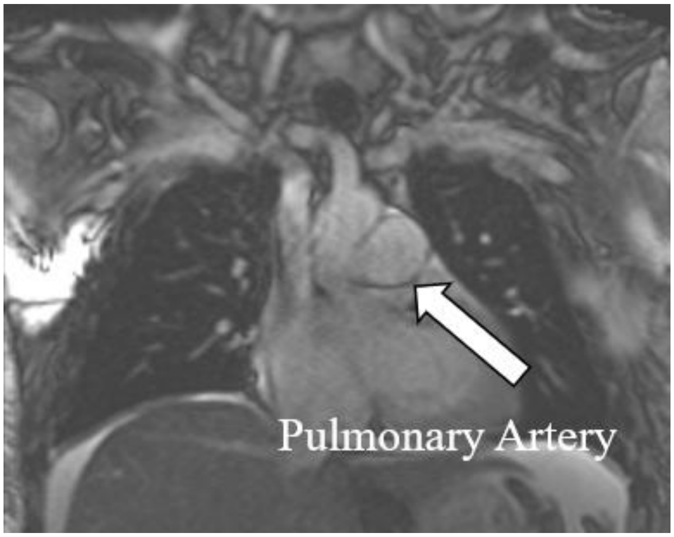

Figure 3.1. Example MR captured image of the pulmonary artery [10].

The patient also underwent phase-contrast MR imaging (PCMRI) for the calculation of a transient velocity waveform of fistula blood flow throughout the cardiac cycle (Figure 3.2). Thirty timepoints were captured of blood flowing through the midplane of the AVF. The echo time of the imaging set was 3.01 ms, the repetition time was 42.96 ms, and the pixel spacing was 1.77 mm. The velocity encoding number used for this session was 100 cm/s.

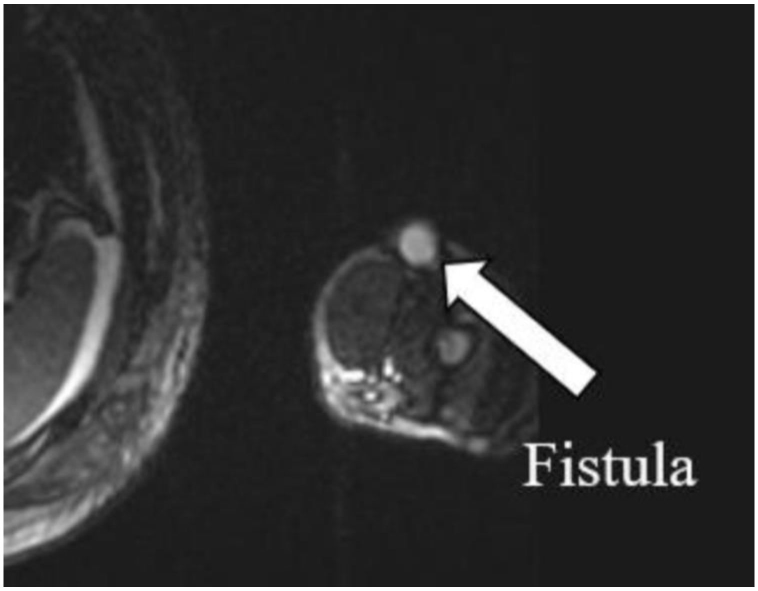

Figure 3.2. Example MR image to capture fistula flow [10].

This is the first study to acquire both pulmonary artery and fistula flow data during the same imaging session, occurring also on the same day as dialysis.

3.5 MRI Velocity Waveform Creation

The transient velocity waveform boundary condition defined at the proximal artery inlet was created using the PCMRI data taken along the midplane of the fistula (Figure 3.3)

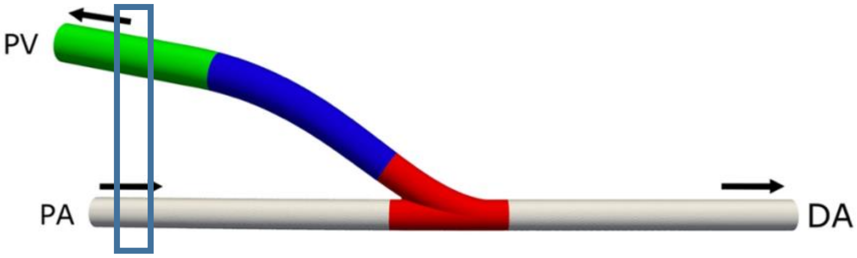

Figure 3.3. The location of PCMRI slice used to calculate velocities in proximal vein and artery. PV: proximal vein. PA: proximal artery. DA: distal artery.

Reprinted by permission from John Wiley and Sons, International Journal for Numerical Methods in Biomedical Engineering, *The presence of helical flow can suppress areas of disturbed shear in parameterised models of an arteriovenous fistula* by Cunnane et al. [48]. Copyright 2019, Published 2019. Image was cut to elicit the fistula geometry. The blue box was added to indicate the location of the MRI slice taken along the AVF.

The MRI waveform was created with in house MATLAB files to crop and isolate cross sections of the AVF from the MRI, segment the AVF cross sections across 30 timesteps in the cardiac cycle, and lastly multiply the segmented AVF cross section images with the phase part of the images to calculate fluid velocity based on the phase shift of rotating particles. Outputs from this process included velocity, flow rate (Figure 3.4), mass flow rate, and vessel diameter and area across 30 time points. Additionally, wall shear stress was estimated using Poiseuille's equation (Equation 5):

$$WSS = \frac{4\mu Q}{\pi r^3} \tag{5}$$

Where μ is the fluid viscosity, Q is the volumetric flowrate, and r is the vessel radius.

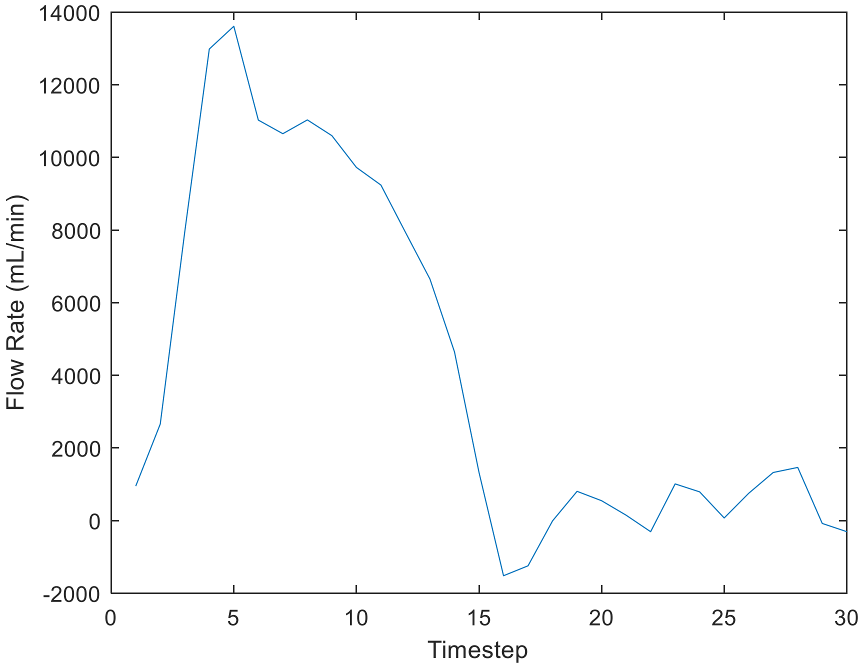

Figure 3.4. Sample fluid flow rate waveform using MRI data [10].

The volumetric flow rate values across all 30 time points were divided by the AVF cross sectional area captured from MR imaging (equivalent to the inlet area for the CFD model) and were then imported into an additional MATLAB code. Here, a velocity profile was created by linearly interpolating a specified number of velocity values between each 30 time points, capturing three full cardiac cycles with many more velocity values in between each MRI velocity value [10]. Three full cardiac cycles were modeled to prevent transient effects at the beginning of the simulations [49], where results were only interpreted during the third cardiac cycle. This process can be outlined in Figure 3.5. The velocity profile was formatted as a .C file, to be interpreted and applied as a user-defined boundary condition in FLUENT.

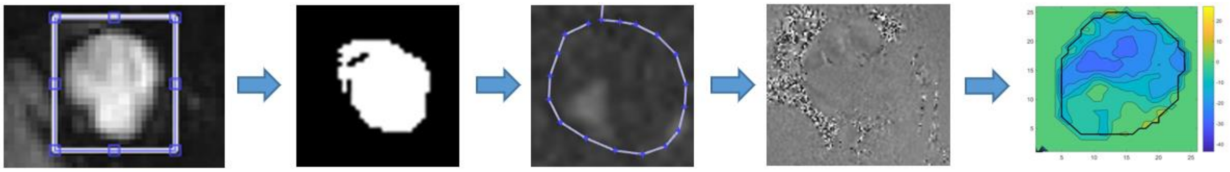
Cropping Segmenting Manual Editing Applying Phase Velocity Contour

Figure 3.5. Workflow for creating transient velocity waveform and contour [10].

Because the PCMR images were taken along the midplane of the AVF the same process was completed for the other imaging sets of the proximal vein, which was then used to validate the computational models.

3.6 Segmentation and 3D Geometry Creation

MR images were imported into Mimics 20.0 for model creation (Figure 3.6). A thresholding technique was used to segment the anatomical geometry captured in each MR slice and the “Calculate 3D” function was used to create a three-dimensional model of the highlighted region.

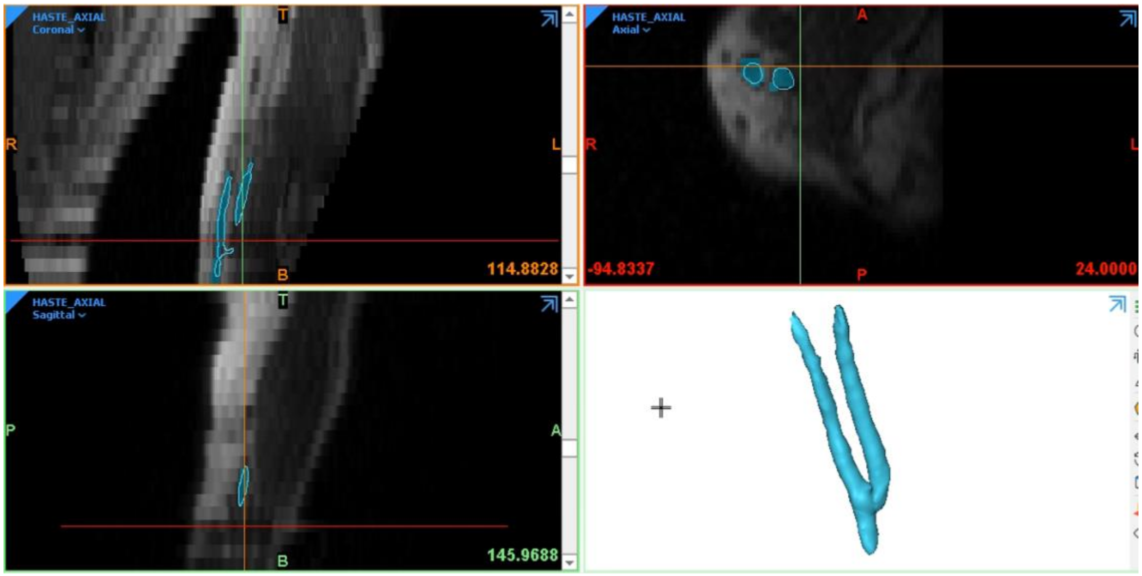

Figure 3.6. Anatomical segmentation of an arteriovenous fistula in Mimics 20.0.

The model was then smoothed in Mimics 20.0 (0.4 smooth factor, 25 iterations) and exported to 3-matic 12.0 where models were trimmed to define inlets and outlets, with perpendicular cross-sectional cuts (Figure 3.7) Lastly, these models were exported to ANSYS Workbench for analysis, in .step file format.

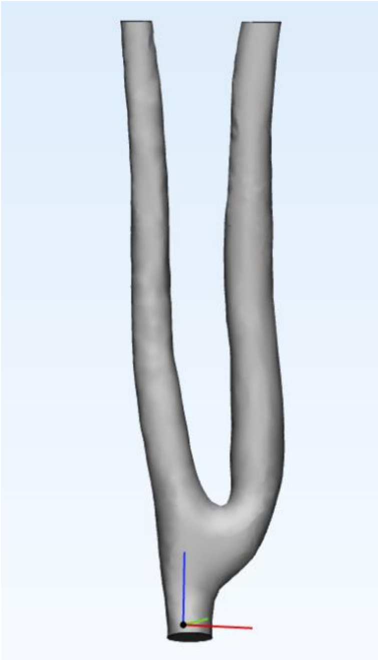

Figure 3.7. A smoothed, three-dimensional AV fistula model created in 3-matic.

3.7 Meshing

The model was uploaded into ANSYS Workbench 19.1, where it was discretized (Figure 3.8), using tetrahedral (Tet4) and wedge (Wed6) elements. A course mesh size was initially applied, and then refined further to achieve results independent of mesh quality. Details of the mesh independence analysis can be found in Appendix A (Table 8.1, 8.2). Additionally, the mesh was increased at the boundary layer, to capture wall mechanics more closely. Metrics such as element quality, orthogonal quality and skewness were used to assess the mesh quality. The constructed mesh had an average element quality, orthogonal quality, and skewness of 0.607 ± 0.31, 0.800 ± 0.11, and 0.199 ± 0.11, respectively, resulting in a model comprised of 1,242,404 elements and 388,355 nodes. This mesh size agreed with previous studies, which used between 1.2 and 1.6 million elements [38].

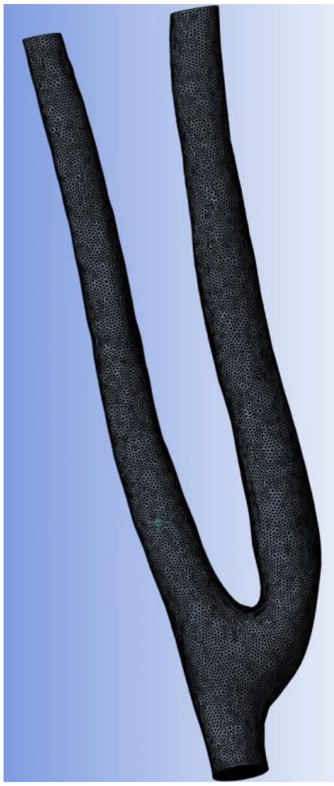

Figure 3.8. Discretized AVF model in ANSYS Meshing.

3.8 Boundary Conditions & Solver Preferences

Blood was characterized as an incompressible, Newtonian fluid with viscosity, 3.2 cP, and density, 1060 kg/m3. The inlet, or the proximal artery, boundary condition was defined by the patients-specific velocity waveform from the MRI. This condition was achieved by applying a blunt constant velocity at each time point to model pulsatile flow. The distal artery and proximal vein were assigned varying boundary conditions dependent on the model, which will be discussed in Section 3.12. These included zero pressure, split flow, or pressure with a targeted mass flow rate. Boundary conditions are shown below in Figure 3.9. A rigid wall assumption and non-slip boundary conditions at the wall were also applied.

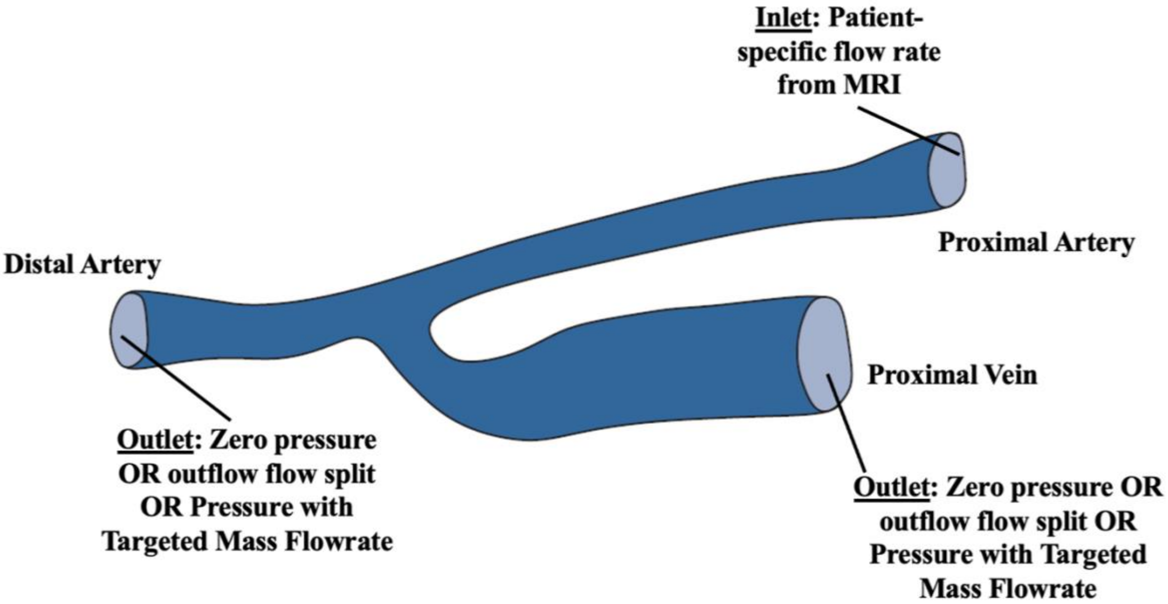

Figure 3.9. Boundary conditions for AVF models.

A double precision, second order, transient flow pressure-based solver was used during CFD analysis. Specifically, a viscous laminar model with a SIMPLE pressure-velocity coupling scheme was used. This coupling scheme included a second order scheme for pressure and a second order upwind scheme for momentum [10]. Times steps for each subject were calculated by multiply the

RR interval, which is the times elapsed between two consecutive R waves of a QRS signal from an ECG, by three to achieve three full cardiac cycles. The total simulation time was 2.343 s, with a single cardiac cycle of 0.781 s, and a time step duration of 0.5849 ms. The Courant number, defined as a dimensionless value representing the number of mesh cells traveled at a given time step, was used to evaluate the time step requirements for the model. The formula considers the velocity magnitude of the flow, the time step size, and the length between mesh elements. An initial time step size was calculated to achieve a Courant number less than 1, meaning particles will not skip a neighboring mesh cell after a single time step [52]. A timestep independence test was then completed, located in Appendix A. The solution was found to be independent of time step size with 4006 time-steps. Lastly, residual values were set to default, 1×10^{-4}. Models were run on a Dell Optiplex 9020 desktop with an Intel i7-4770 3.40 GHz CPU with four cores, six logical processors, and 16 GB of RAM [10].

3.9 Post-Processing and Data Analysis

Post-processing included velocity streamline plots, velocity volume rendering, and WSS contours, all visualized using CFD Post. These measurements were compared and analyzed using maximum, minimum, and volume weighted averaged velocities, and maximum, minimum, and area averaged WSS values. Additionally, time averaged WSS (TAWSS) and oscillatory shear index (OSI) were calculated. The values were compared between the varying fistula geometry lengths and boundary conditions, and with pulmonary artery hemodynamic and clinical measures. Figure 3.10 illustrates the terminology used when comparing section or areas of the fistula and anastomosis [44].

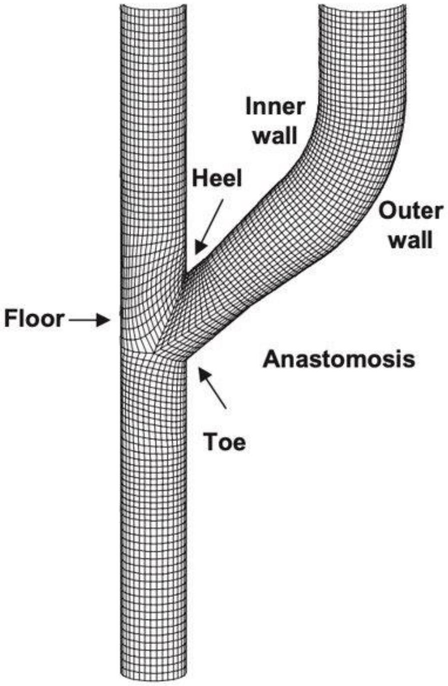

Figure 3.10. Fistula geometry terminology.

Reprinted by permission from Oxford University Press, Nephrology Dialysis Transplantation, *Disturbed flow in radial-cephalic arteriovenous fistulae for haemodialysis: Low and oscillating shear stress locates the sites of stenosis* by Ene-Iordache et al. [44]. Copyright 2011, Published 2012. Figure was cut to highlight the AVF terminology for the end-to-side fistula geometry.

3.10 Model Validation

The model was validated at a plane along the proximal vein outlet. Cross sectional velocity contours produced by the MATLAB code discussed in Section 3.5 were compared to velocity contours generated from CFD-Post at a similar location along the proximal vein. Validation was completed to ensure hemodynamic velocity measures were similar amongst the CFD simulation results and MRI cardiac measures.

3.11 Employed Computational Models

Multiple models were run and compared to accomplish the three outlined aims (Table 3.1). To accomplish Aim 1, a preliminary study was completed to construct and compare fistula CFD models with geometry length variations (Simulations 1-3). The lengths of the models were determined by multiplying the diameter of the proximal artery from the 64 mm model by 12 and 17 and subtracting that length from the 64 mm model. This resulted in models with lengths of 64 mm, 51 mm, and 36 mm, respectively. These lengths were chosen to represent a large range in geometry variations to hopefully elicit noticeable similarities and differences. For these models, the proximal vein and distal artery were prescribed outflow conditions (81% PV, 19% DA) obtained from literature [44]. For the additional simulations, a model with a shortened geometry length was used. A more simplified geometry provided a model with fewer mesh elements, reduced computational cost, and more efficient simulations. Following this preliminary work, models with varying boundary conditions were constructed to compare flow patterns (Simulations 4-6). The outflow split for Simulation 5 was calculated from the PCMR images, by dividing the flow rate from the proximal vein by the flowrate from the proximal artery (inlet) to get a percentage of flow that goes through the proximal vein. The remainder of the flow then travels through the distal artery. Additionally, a two-dimensional model was constructed with the patient specific outflow conditions (Simulation 7). Data from the simulations were correlated and compared to clinical parameters of PH and with AVF models from previous literature (Aim 2).

Interestingly, pulmonary hypertension can be reversed if the AVF is closed or after kidney transplantation. Rao et al, observed decreased atrial volume, cardiac output, and left ventricular end-systolic and diastolic dimensions following kidney transplantation and AVF ligation [50]. Flow management techniques such as precision banding are known to be safe and effective in reducing AVF venous flow output. This procedure involves creating an adjustable band (usually polyester-urethane) with Doppler ultrasound-guided flow measurements to determine the optimal band diameter for desired flow restriction [51]. With the band placed along the vein, more blood flow is directed to the distal artery. To accomplish Aim 3, a three-dimensional model with a theoretical band was constructed to investigate the impact of fistula banding on fistula hemodynamics (Simulation 8-10). The size and placement of the band was based upon a study completed by Lee et al. They found a band of 4 mm produced adequate fistula blood flow reduction for patients with symptomatic high-flow AVFs [51]. The banded geometry can be seen in Figure 3.11.

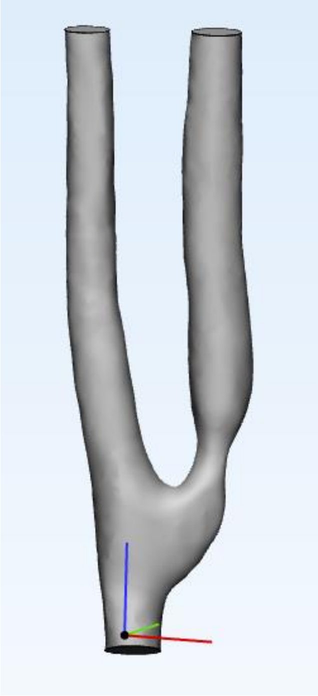

Figure 3.11. A Three-dimensional banded AV fistula geometry created in 3-matic.

From literature, the underlying principle of fistula banding is to limit the output of the fistula without compromising access function or stenosis development [50]. To mimic this occurrence, three simulations were run with different output split flows: 1) 84% PV, 16% DA, 2) 81% PV, 19% DA, and 3) 78% PV, 22% DA.

Table 3.1. Summary of performed simulations.

Simulation	Model Geometry	Outlet Boundary Conditions
1	64 mm	Outflow: 81% PV, 19% DA
2	51 mm	Outflow: 81% PV, 19% DA
3	36 mm	Outflow: 81% PV, 19% DA
4	51 mm	Zero Pressure
5	51 mm	Outflow: 84% PV, 16% DA
6	51 mm	Pressure w/ Targeted Mass Flow rate
7	2D 51 mm	Outflow: 84% PV, 16% DA
8	51 mm banded	Outflow: 84% PV, 16% DA
9	51 mm banded	Outflow: 81% PV, 19% DA
10	51 mm Banded	Outflow: 78% PV, 22% DA

The workflow steps outlined in the previous sections (meshing, fluid properties, solver preferences, and post-processing) are consistent for all simulations constructed above.

CHAPTER 4. RESULTS

This chapter will present the results found using the methodology outlined in the previous chapter. Findings from each simulation were grouped to compare geometry lengths, varying boundary conditions, a two-dimensional model, and fistula banding models. Subject recruitment, MRI analysis, and validation results will also be discussed.

4.1 Subject Recruitment

Due to the COVID-19 pandemic, subject recruitment was limited to one (n=1). The subject was an African American male, 41 years old at the time of imaging, diagnosed with pulmonary hypertension by RHC numerous months before the time of imaging, and had an arteriovenous fistula actively being used for dialysis. Via RHC this subject had a mPAP of 54 mmHg, a PCWP of 35 mmHg, a PVR of 2.07 Wood Units, and a CO of 8.2 L/min. Up to the imaging session the subject was still undergoing dialysis with the AVF imaged in this study. The subject was not undergoing hemodialysis while inside the MRI machine.

4.2 MRI Velocity Analysis

From the PCMRI data, the average RR interval was 0.781 ± 0.005 seconds, spanning across 22 heart beats. Table 4.1, shown below, includes the patient specific AVF mean vessel area, velocity, flow rate, and diameter across the 30 time points of one cardiac cycle. The entire output from the MATLAB code across all 30 time points can be viewed in Appendix A (Table 8.5). The equivalent MATLAB outputs for the pulmonary artery are included in Table 4.2. The estimated WSS, using Equation 5, is also found in the tables.

Table 4.1. Mean AVF MATLAB output data at the proximal artery from PCMRI across one cardiac cycle.

Vessel Area (cm^2)	Velocity (cm/s)	Flow Rate (mL/min)	Diameter (mm)	Average WSS ($dyne/cm^2$)
0.075	17.609	1967.494	0.308	40.9

Table 4.2. Mean pulmonary artery MATLAB output data from PCMRI across one cardiac cycle.

Vessel Area (cm^2)	Velocity (cm/s)	Flow Rate (mL/min)	Diameter (cm)	Average WSS ($dyne/cm^2$)
10.243	6.756	4146.751	3.611	57.0

The patient specific flowrate plotted across one cardiac cycle is displayed in Figure 4.1. This patient had a mean AVF flow rate of 1.97 L/min. Additionally, the proximal artery inlet velocity waveforms for each geometry length can be seen in Figure 4.2. The waveforms were adjusted based upon the cross-sectional area of the proximal artery, to ensure the same flow rate was achieved for all models.

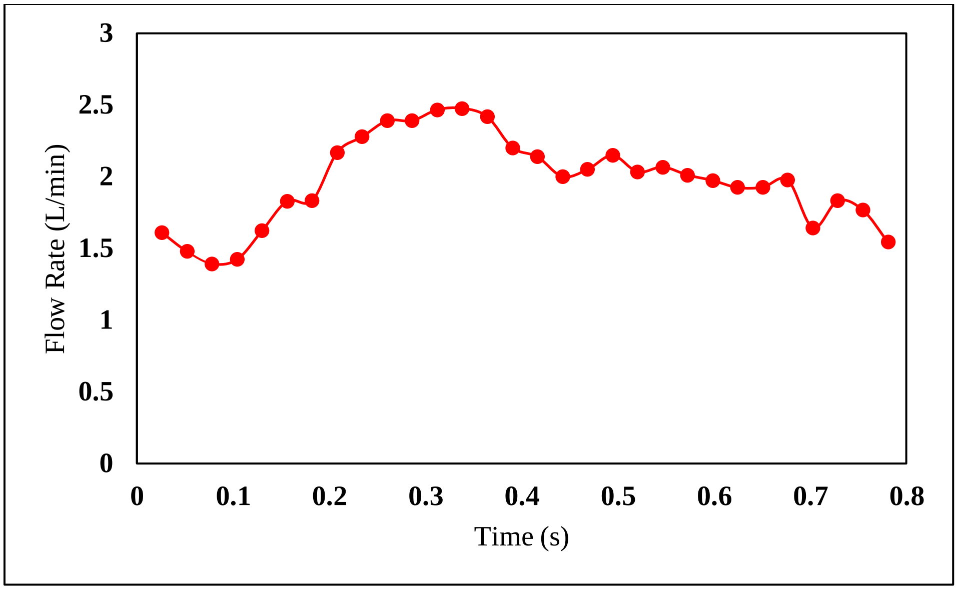

Figure 4.1. Flowrate waveform at proximal artery across one cardiac cycle.

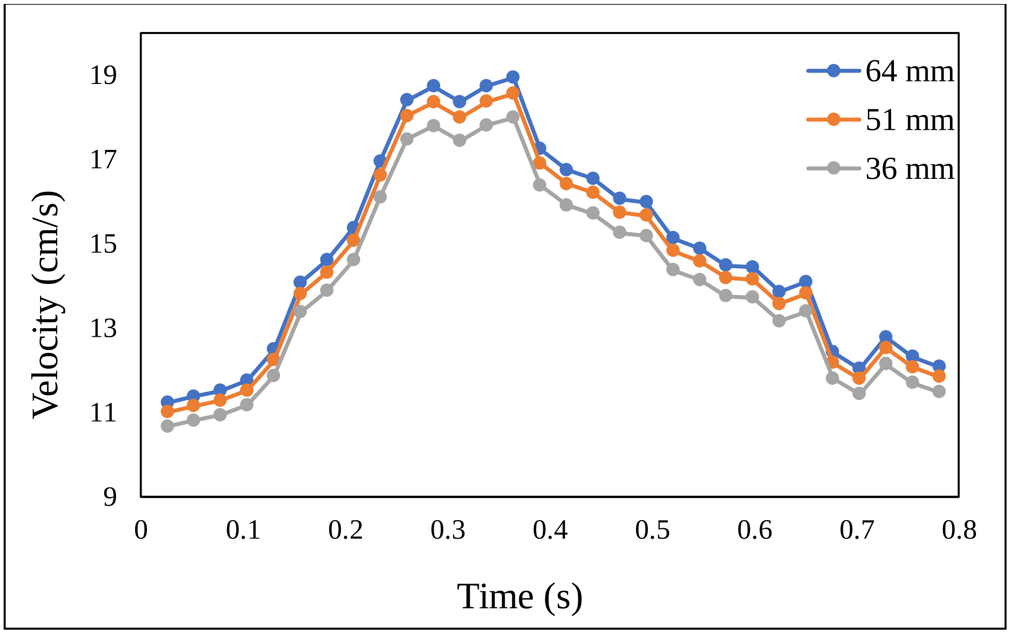

Figure 4.2. Proximal artery inlet velocity waveforms for each geometry length model.

4.3 Model Validation

Before analyzing the simulation results, model validation was performed to ensure rational results. Figure 4.3 indicates the location of the slice, along the proximal vein, which was used to validate the model. In CFD-Post, cross sectional planes with velocity contours were generated and compared with the cross sections generated by MRI analysis (Figure 4.4). Velocity contours were evaluated at two-time points A) peak systole, and B) the start of diastole. At Point A, MRI calculations revealed an average thru plane velocity of 26.27 cm/s and CFD-Post indicated an average velocity magnitude at the contour slice of 21.45 cm/s. At Point B, MRI and CFD-Post estimated an average velocity of 20.96 cm/s and 19.26 cm/s, respectively. Also, similar velocity distributions were seen for both cross sections, but the area of relative maximum velocity is different. The MRI generated contours indicated a maximum velocity towards to bottom of the cross section, compared to the CFD-Post maximum velocity in the center. Overall, between the MRI analysis and CFD-Post velocity estimations, there is an underestimation present. However, quantitatively similar trends in velocity and fluid flow development are seen across the two time points, and they do not appear otherwise different.

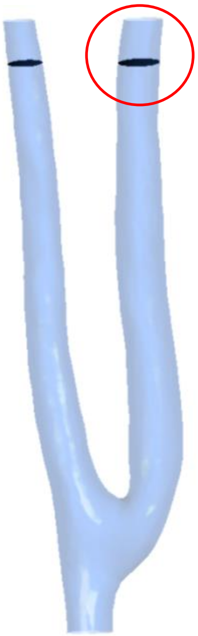

Figure 4.3. Location of CFD-Post cross-sectional plane along the proximal vein (circled in red) for validation.

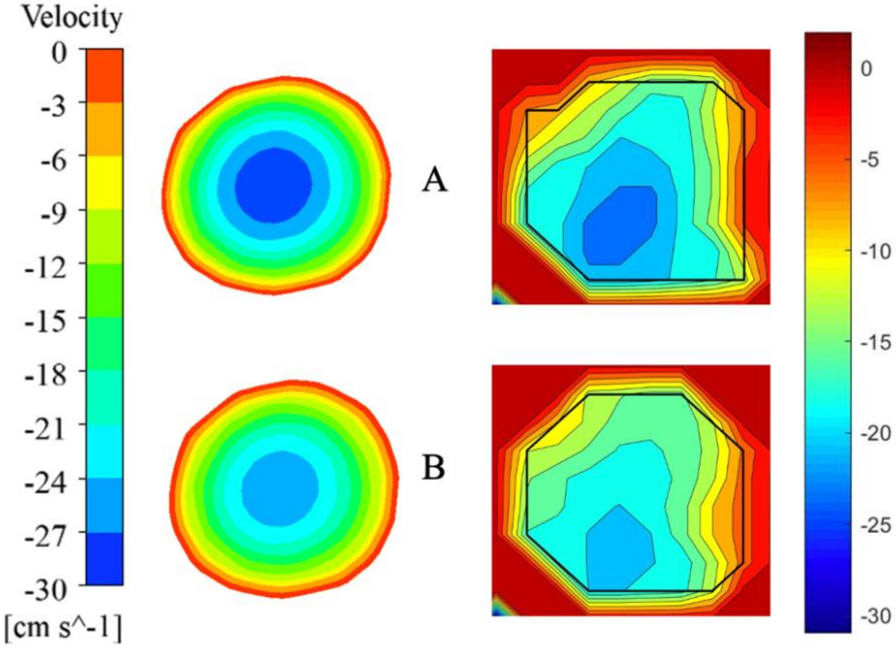

Figure 4.4. A comparison of MRI (right) and CFD-Post (left) cross-sections along the proximal vein for model validation. A) Peak systole, B) Start of diastole.

4.4 Geometry Comparison Models

The following section presents the results collected from the FLUENT models with varying geometry lengths. These models can be seen in Figure 4.5.

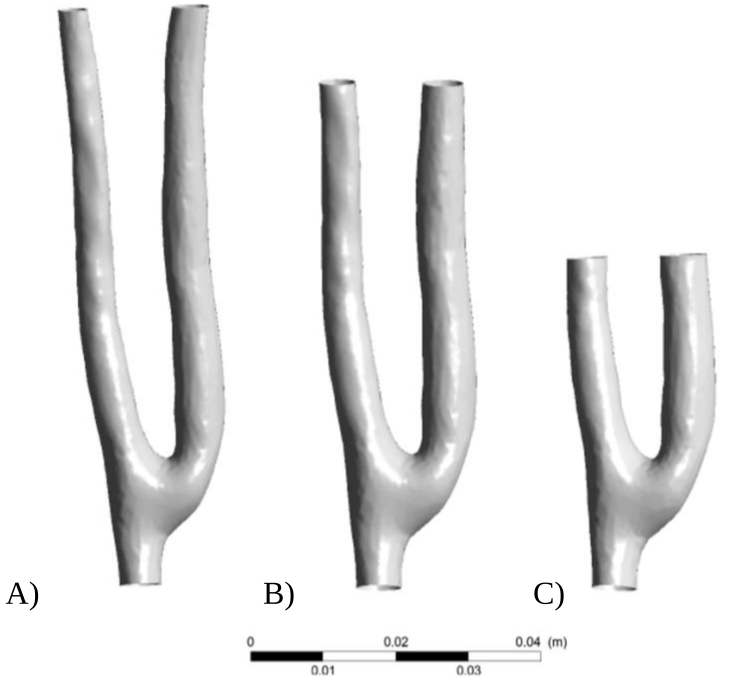

Figure 4.5. 3D geometries of A) 64 mm, B) 51 mm, and C) 36 mm models.

Figures 4.6 and 4.7 show velocity streamlines and velocity volume renderings taken at peak systole for the three models. For the 64 mm model, the maximum velocity was 31.79 cm/s and the volume weighted average velocity was 9.64 cm/s. For the 51 mm model, a maximum velocity of 26.24 cm/s and a volume weighted average velocity of 8.81 cm/s were found. Lastly, for the 36 mm model the maximum velocity was 22.19 cm/s and the volume weighted average velocity was 8.50 cm/s. A minimum velocity of 0.00 cm/s was computed for each model.

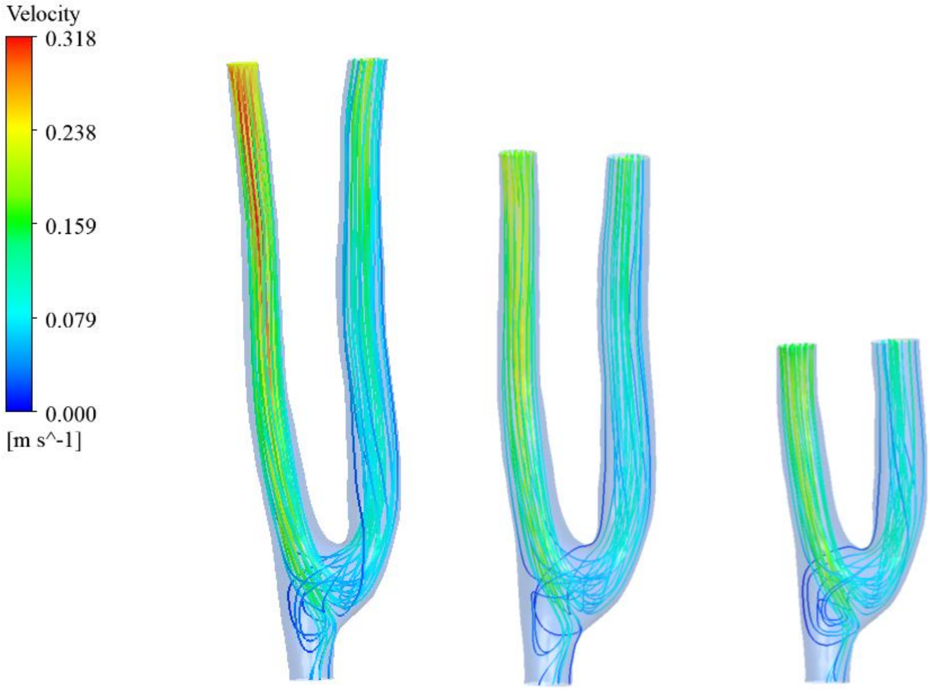

Figure 4.6. Velocity streamlines for the varying geometry length models at peak systole. From left to right: 64 mm, 51 mm, 36 mm.

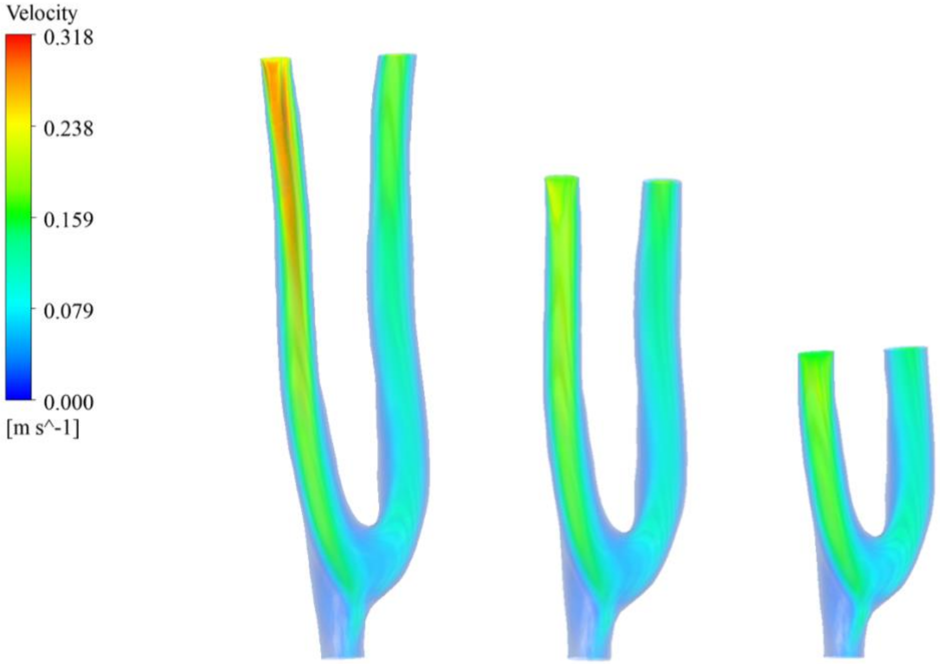

Figure 4.7. Velocity volume renderings for the varying geometry length models at peak systole. From left to right: 64 mm, 51 mm, 36 mm.

Velocity patterns were similar for all models, with the 64 mm model having the greatest velocity.

For comparison, cross sectional planes of velocity contours were taken along the same location for all three models. The location of the cross-sectional planes can be viewed in Figure 4.8 and the velocity contours at peak systole and the start of diastole are shown in Figures 4.9 and 4.10, respectively. At peak systole, the area averaged planar velocity for the 64 mm, 51 mm, and 36 mm models were found to be 8.05 cm/s, 8.08 cm/s and 8.98 cm/s, respectively. At the start of diastole, the area averaged planar velocity for the 64 mm, 51 mm, and 36 mm models were 6.97 cm/s, 6.99 cm/s, and 7.80 cm/s, respectively.

Figure 4.8. Location of cross sectional plane, used to compare the three models. From left to right: 64 mm, 51 mm, 36 mm.

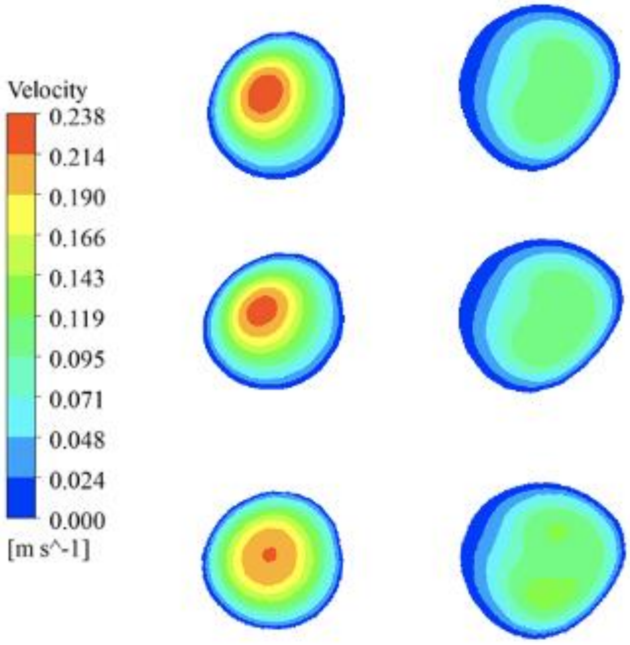

Figure 4.9. Cross-section plane with velocity contours at peak systole. From top to bottom: 64 mm, 51 mm, 36 mm.

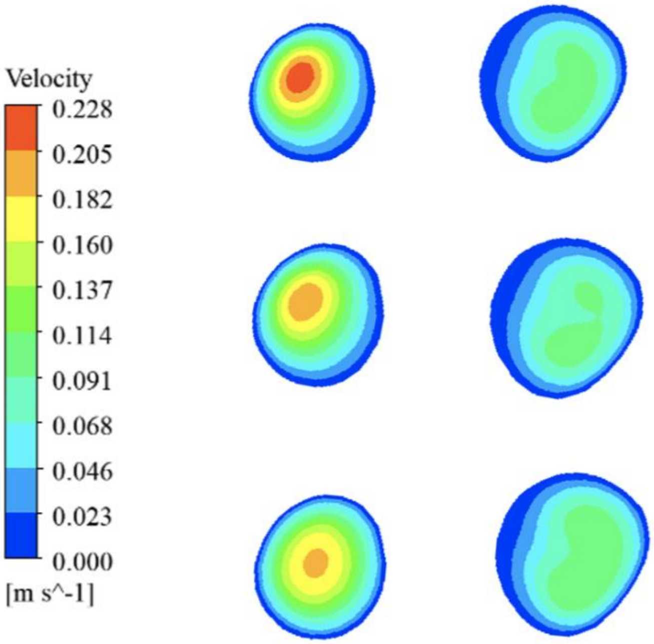

Figure 4.10. Cross section plane with velocity contours at the start of diastole. From top to bottom: 64 mm, 51 mm, 36 mm.

Maximum and area averaged planar velocity along the cross section were very similar between the 64- and 51- mm models.

Table 4.3 represents maximum velocity and area averaged velocity, along the cross section slice, taken at peak systole and the start of diastole for the three models.

Table 4.3. Velocity measurement results along the cross section plane at peak systole and diastole for the geometry length comparison models.

	Time Point	Maximum Velocity Magnitude (cm/s)	Area Average Velocity (cm/s)
64 mm	Peak Systole	22.88	8.05
	Diastole	22.40	6.97
	Average	**22.64**	**7.51**
51 mm	Peak Systole	22.99	8.08
	Diastole	21.11	6.99
	Average	**22.05**	**7.54**
36 mm	Peak Systole	21.50	8.98
	Diastole	19.50	7.80
	Average	**20.50**	**8.39**

Figure 4.11 depicts the wall shear stress experienced at peak systole for each model. For the 64 mm model, a maximum WSS of 3.65 Pa, a minimum WSS of 0.00836 Pa and an area averaged WSS of 0.647 Pa was calculated. For the 51 mm model, a maximum WSS of 3.44 Pa, a minimum WSS of 0.00922 Pa, and an area averaged WSS of 0.607 Pa was found. Lastly the 36 mm model experienced, a maximum WSS, minimum WSS, and area averaged WSS of 2.77 Pa, 0.00601 Pa, and 0.595 Pa, respectively. The maximum WSS for each model occurred at the proximal artery inlet and the areas of minimum WSS occurred along the anastamosis floor and heel. A zoomed in capture of the anasatomosis region for each model, seen in Figure 4.12, shows these similaries.

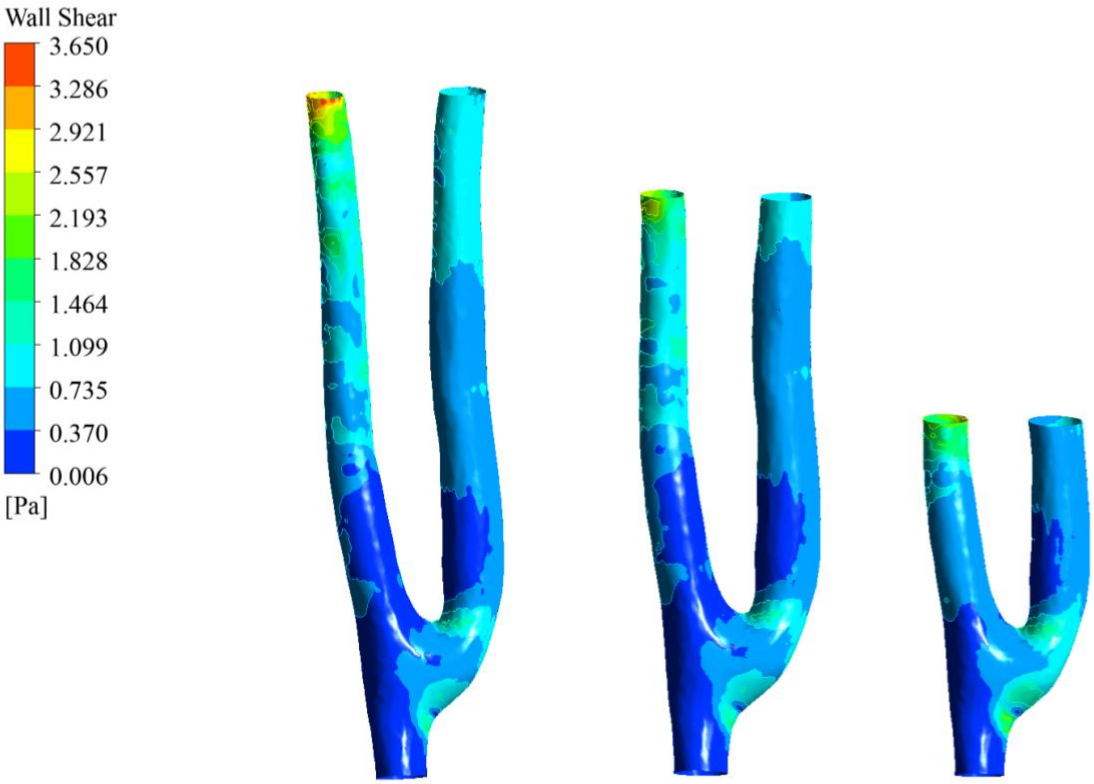

Figure 4.11. Wall shear stress contours, at peak systole, for the varying geometry length models. From left to right: 64 mm, 51 mm, 36 mm.

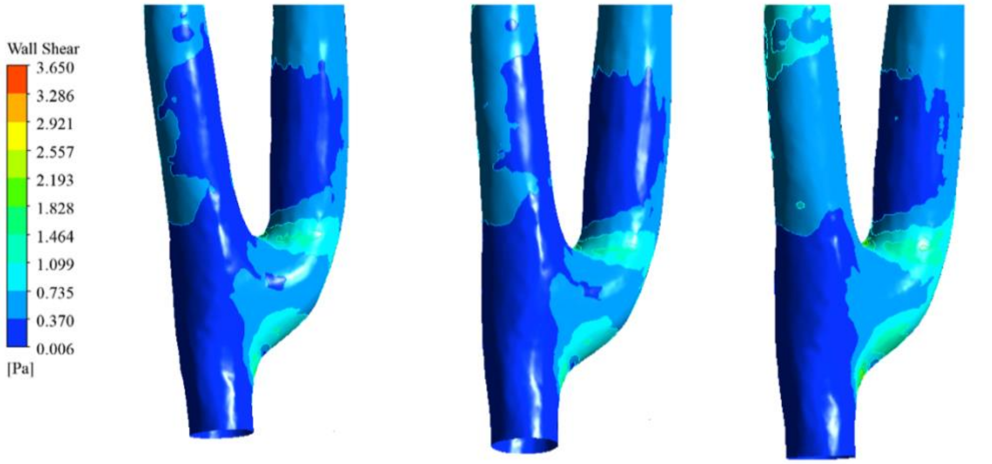

Figure 4.12. Zoomed in capture of anastamosis region, at peak systole, for the varying geometry length models. From left to right: 64 mm, 51 mm, 36 mm.

WSS patterns are similar for all models, especially along the anastomosis region.

Table 4.4 provides a summary of the significant results from the models with varying geometry lengths. Results include parameters such as maximum velocity, maximum and minimum wall shear stress, as well as simulation information such as the number of mesh elements and run time. Comparing the three models, it is worth pointing out the minute differences in parameters between the 64 mm model and the 51 mm model. Even though maximum velocities varied in each model, maximum WSS only varied slightly. Recognizing the significant differences in run time and the minimal dissimilarities in the parameters of interest, the 51 mm model represents a viable option for a simplified AVF geometry. Simulations for the duration of the project were completed using the simplified 51 mm geoemtry for a more rapid time to CFD solutions with negligeable impact on the results.

Table 4.4. Summary of geometry length comparison models. Results taken at peak systole along the entire geometry.

	64 mm	**51 mm**	**36 mm**
Mesh Elements	1,243,742	1,071,531	776,111
Run Time (hh:mm)	6:49	5:47	4:37
Maximum Velocity (cm/s)	37.19	26.24	22.19
Volume Weighted Average Velocity (cm/s)	9.64	8.81	8.50
Minimum WSS (Pa)	0.00836	0.00922	0.00601
Maximum WSS (Pa)	3.65	3.44	2.77
Time Averaged WSS (Pa)	0.655	0.629	0.610
Area Averaged WSS (Pa)	0.647	0.607	0.595

4.5 Boundary Condition Comparison Model

This section presents the results of the simulations with three different outlet boundary conditions: zero pressure, patient specific outflow flow split (84% PV, 16% DA), and pressure with targeted mass flow rate. The velocity waveform applied at the proximal artery inlet is consistent in all simulations. For each boundary condition simulation, velocity contours, velocity volume renderings, and wall shear stress contours were generated.

For the zero pressure outlet condition simulation, velocity streamlines, velocity volume renderings, and WSS coutours generated at peak systole and the start of diastole can be seen in Figures 4.13, 4.14. an 4.15, respectively. At peak systole the maximum velocity was 26.19 cm/s where as, at the start of diastole the maximum velocity was 23.64 cm/s. The volume weighted average velocity at peak systole and diastole were caculated at 6.07 cm/s and 5.27 cm/s, respectively. At peak systole, the maximum WSS, minimum WSS, and average WSS was 2.45 Pa, 0.00183 Pa, and 0.358 Pa. At the start of diastole, the maximum WSS, minimum WSS, and average WSS was 2.00 Pa, 0.000980 Pa, and 0.284 Pa. During both peak systole and the start of diastole, small WSS and velocity measures dominated the proximal vein.

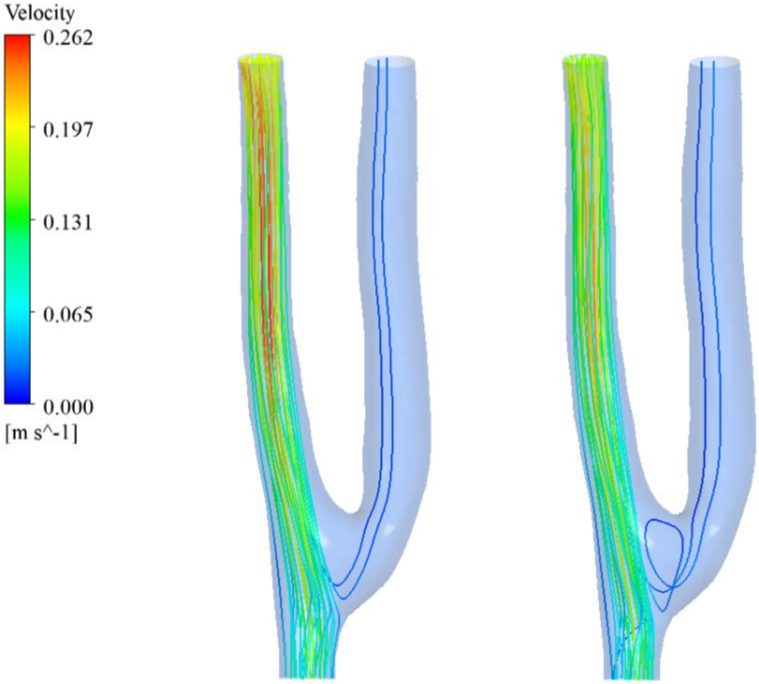

Figure 4.13. Velocity streamlines with zero pressure outlets. From left to right: Peak systole, diastole.

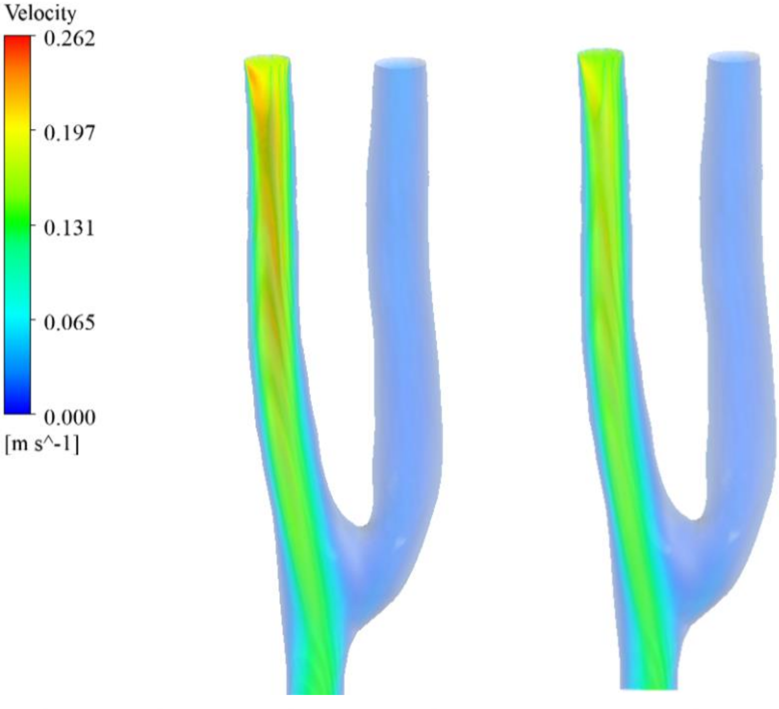

Figure 4.14. Velocity volume renderings with zero pressure outlets. From left to right: Peak systole, diastole.

Almost no flow occurred along the proximal vein.

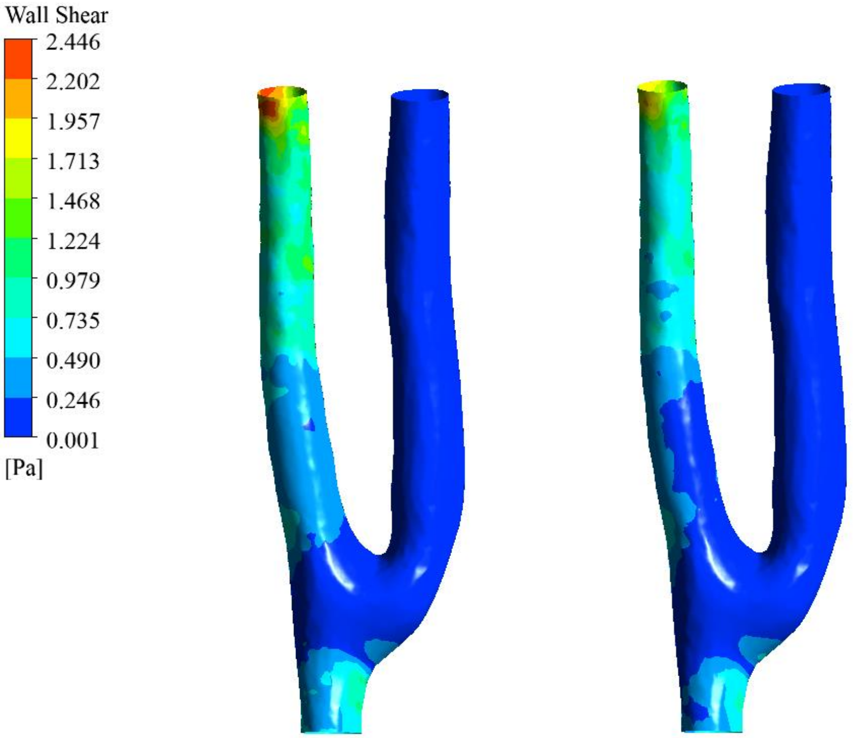

Figure 4.15. WSS contours with zero pressure outlet conditions. From left to right: Peak systole, diastole.

No flow along the proximal vein resulted in low WSS values.

With the zero pressure outlets, the patient specific flow split was not achieved with only 11.4% exiting the proximal vein and 88.6% through the distal artery. Zero or relative pressure outlets do not model physiologically accurate flow and assume the vessel is cut and exposed to atmospheric air conditions (1 atm). This outlet condition is primarily used for simplicity and does not account for the backwards pressure and flow rate wave reflection from downstream vessels [49].

For the patient specific split flow outlet condition simulation, 84% of flow is directed towards the proximal vein with 16% to the distal artery. This type of boundary condition is used to model flow outlets where the flow velocity and pressure are not known [31]. For the split flow simulation velocity streamlines, velocity volume renderings, and WSS coutours generated at peak systole and the start of diastole can be seen in Figures 4.16, 4.17. an 4.18, respectively. At peak systole, the maximum velocity was 26.19 cm/s whereas, at the start of diastole the maximum velocity was 23.61 cm/s. A volume weighted average velocity at peak systole and diastole of 8.95 cm/s and 7.89 cm/s were computed. At peak systole, the maximum WSS, minimum WSS, and average WSS was calculated at 2.44 Pa, 0.00785 Pa, and 0.597 Pa. At the start of diastole, the maximum WSS, minimum WSS, and average WSS was 2.12 Pa, 0.00685 Pa, and 0.498 Pa. Area averaged WSS and volume weighted average velocity increased by 41.4% and 50.5%, respectively, compared to the zero pressure outlet simulation. Figure 4.19 depicts the those areas of physiologically low WSS, or WSS < 1 Pa. The grey areas indicate regions with WSS > 1 Pa.

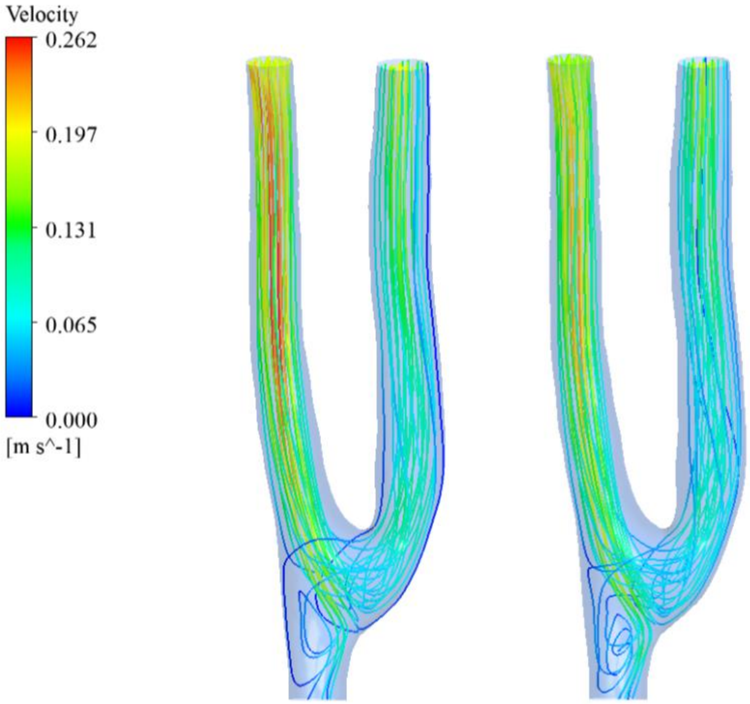

Figure 4.16. Velocity streamlines with split flow outlet conditions. From left to right: Peak systole, diastole.

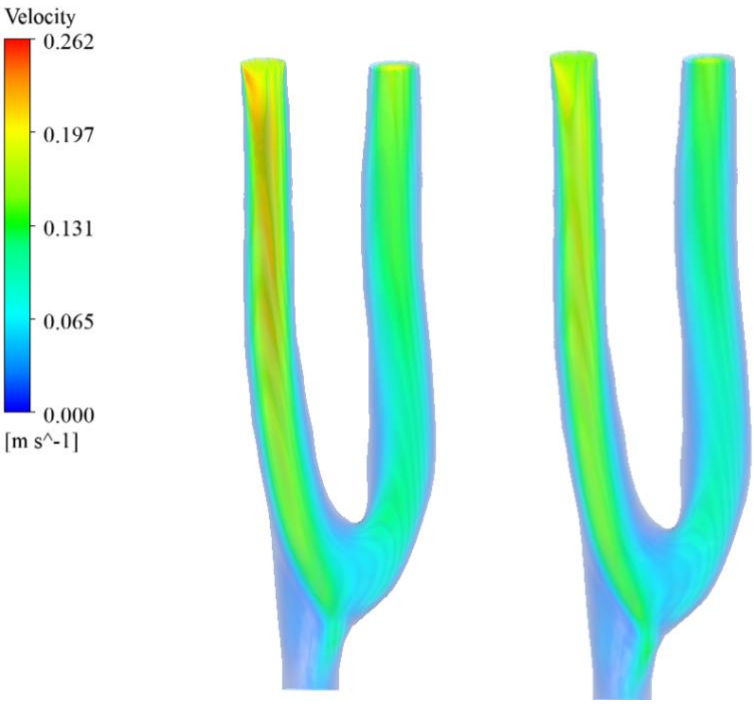

Figure 4.17. Velocity volume renderings with split flow outlet conditions. From left to right: Peak systole, diastole.

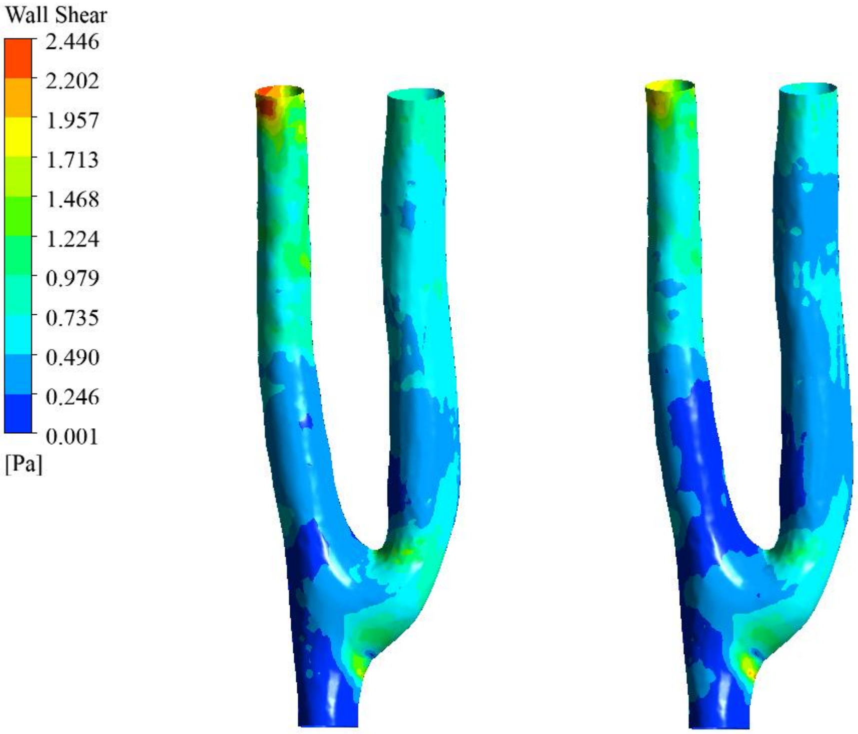

Figure 4.18. WSS contours with split flow outlet conditions. From left to right: Peak systole, diastole.

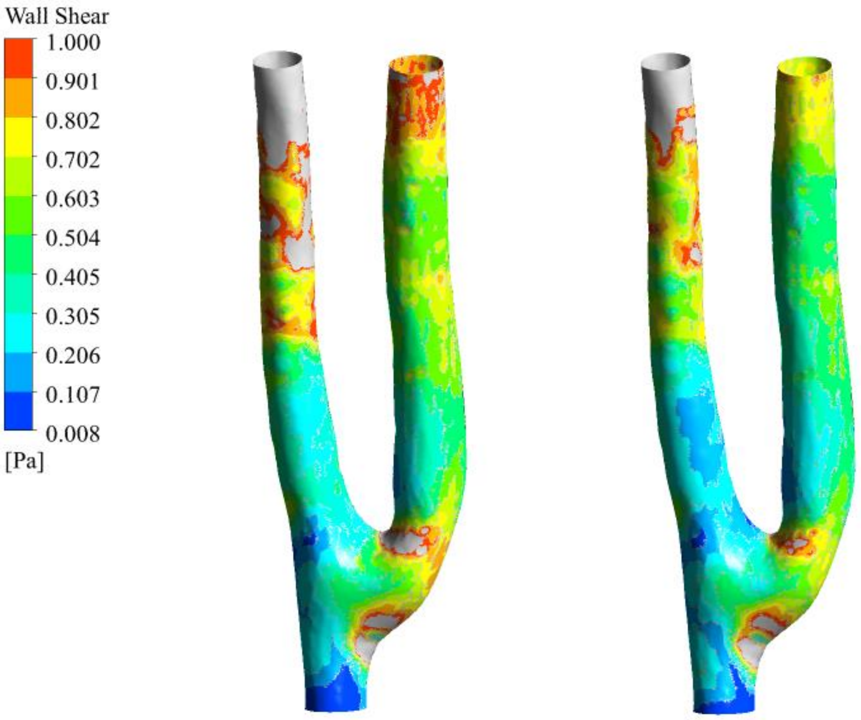

Figure 4.19. Physiologically low WSS (<1 Pa) contours split flow outlet conditions. From left to right: Peak systole, diastole.

A vast majority at the fluid wall has WSS values < 1 Pa.

This patient specific split flow simulation resulted in a mass flow rate of 0.029086 kg/s at the proximal vein, and 0.00554 kg/s at the distal artery. These mass flow rates were used as boundary conditions in the next simulation (pressure with targeted mass flowrate). In FLUENT, the target mass flow rates are achieved by adjusting the pressure value at the pressure-outlet up and down at every iteration, based on the simple Bernoulli's equation [31].

For the pressure with targeted mass flow rate outlet condition simulation, velocity streamlines, velocity volume renderings, and WSS coutours generated at peak systole and diastole can be seen in Figures 4.20, 4.21. an 4.22, respectively. At peak systole the maximum velocity was 26.20 cm/s whereas, at the start of diastole the maximum velocity was 23.62 cm/s. The volume weighted average velocity at peak systole and diastole was calculated at 8.98 cm/s and 8.42 cm/s, respectively. At peak systole, the maximum WSS, minimum WSS, and average WSS was calculated at 2.44 Pa, 0.00357 Pa, and 0.602 Pa. At the start of diastole, the maximum WSS, minimum WSS, and average WSS was 2.02 Pa, 0.00278 Pa, and 0.555 Pa. Similiar to the split flow outlet simulation, the maximum WSS occurred at the proximal artery and minimum WSS occurred along the anastamosis floor and heel. Relative to the split flow model, the pressure with a targeted mass flow rate simulation returned a 0.333% and 0.836% difference in peak systolic volume weighted average velocity and area averaged WSS, repsectively. Additionally, areas of recirculation along the anasatomosis floor were only present in the flow split and pressure with targeted mass flow rate simulations.

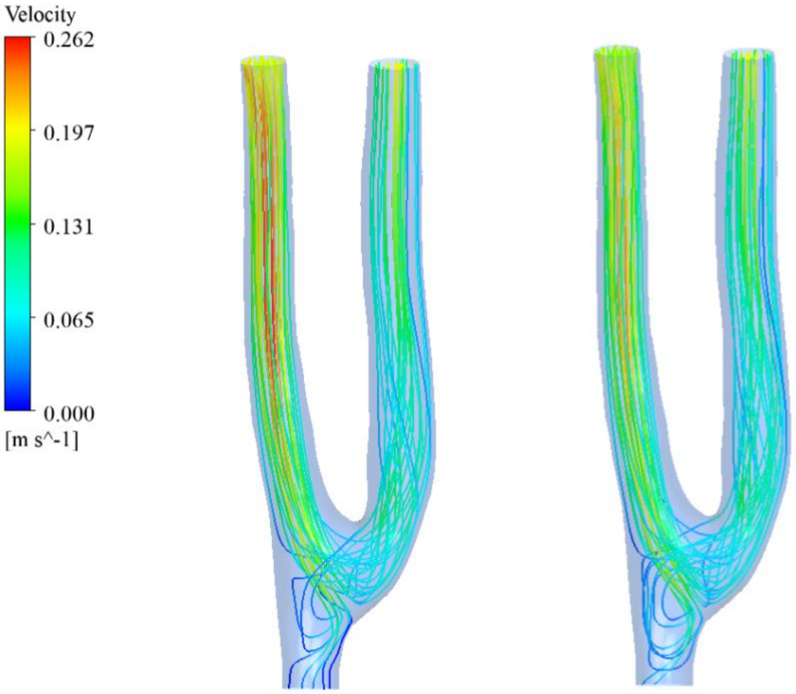

Figure 4.20. Velocity streamlines for the pressure with targeted mass flow rate outlet conditions. From left to right: Peak systole, diastole.

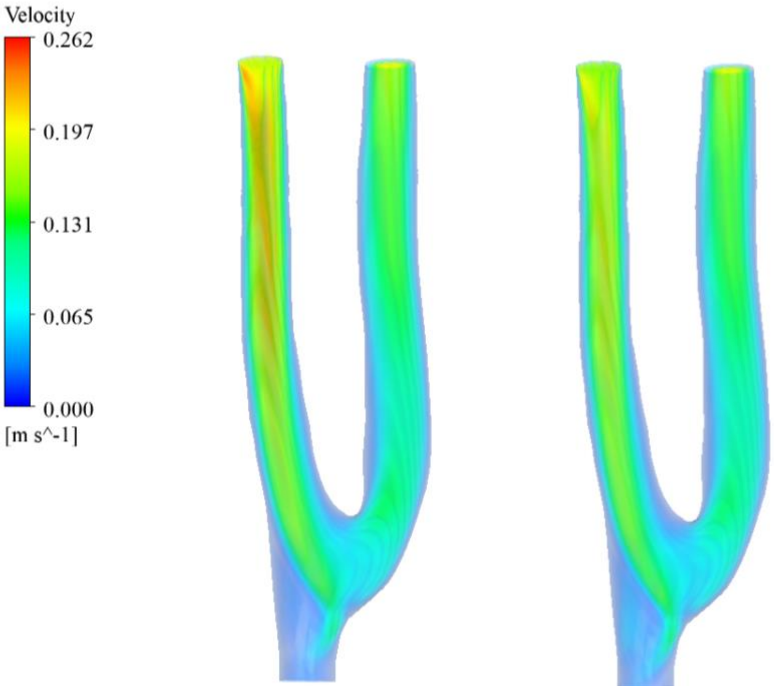

Figure 4.21. Velocity volume renderings for the pressure with targeted mass flow rate outlet conditions. From left to right: Peak systole, diastole.

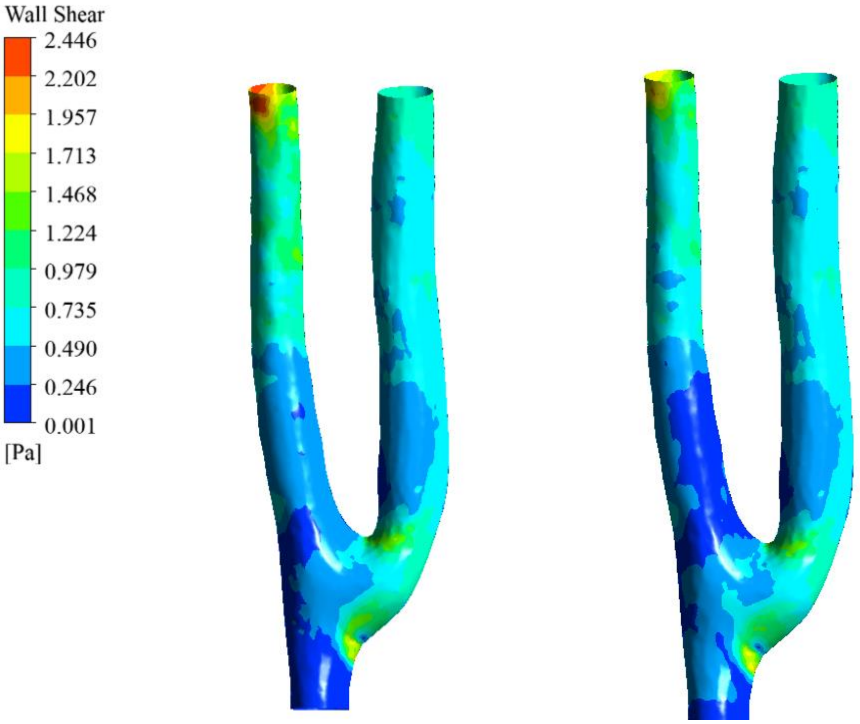

Figure 4.22. WSS contours for the pressure with targeted mass flow rate outlet conditions. From left to right: Peak systole, diastole.

Maximum and average WSS over the third cardiac cycle for each outlet condition model are plotted in Figures 4.23 and 4.24. Averaged TAWSS for the zero pressure, split flow, and pressure with targeted mass flow rate simulations were 0.264 Pa, 0.441 Pa, and 0.517 Pa, respectively. Additionally, OSI was estimated at 0.0784, 0.123, 0.0713. Maximum WSS over the cardiac cycle for the boundary conditions models is very similar however, average WSS varies sgnificantly, with the zero pressure outlet simulation resulting in lower WSS values.

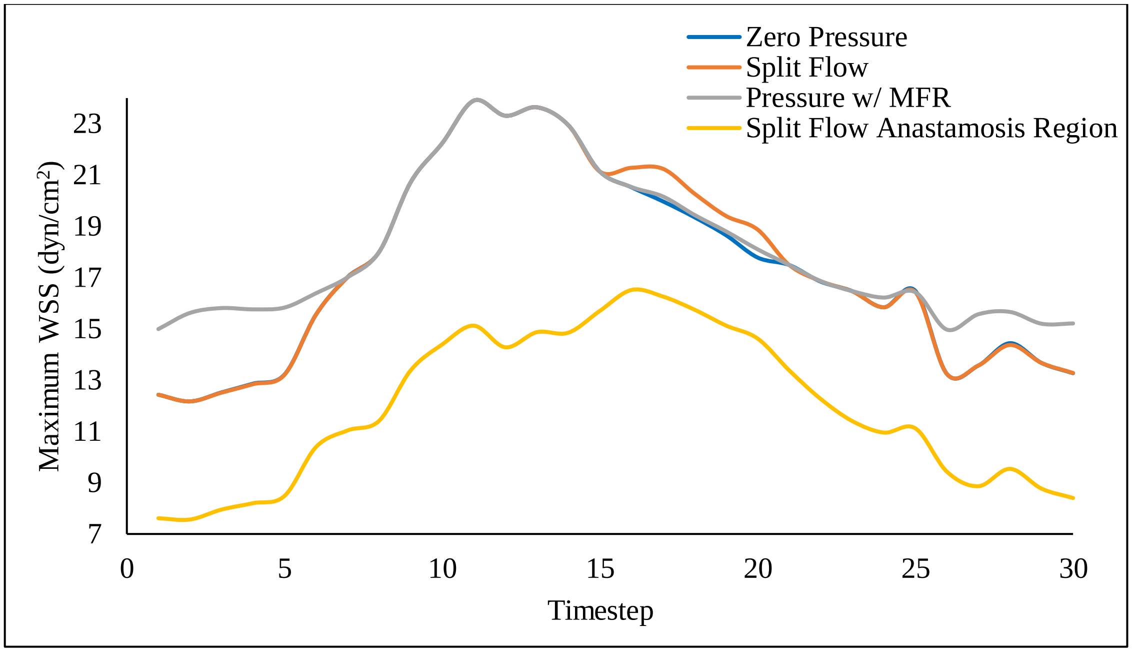

Figure 4.23. Maximum WSS for each outlet boundary condition plotted across 30 time points for the third cardiac cycle. The anastamosis region of the split flow model is also included.

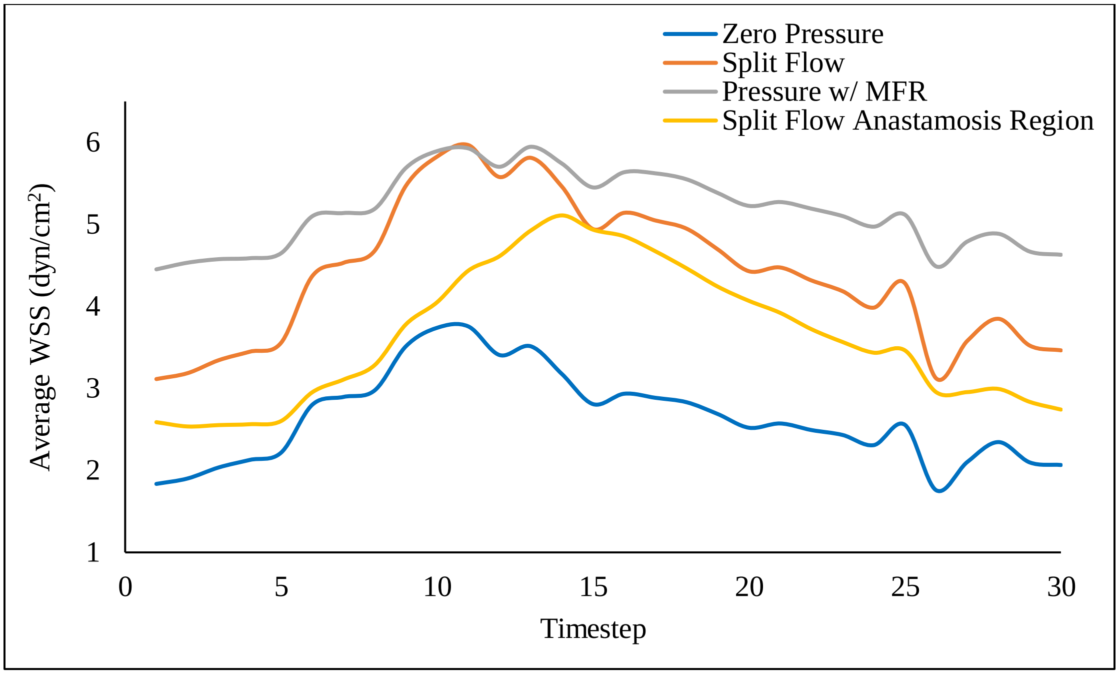

Figure 4.24. Average WSS for each outlet boundary condition, plotted across 30 time points for the third cardiac cycle. The anastamosis region of the split flow model is also included.

Table 4.5 summarizes the significant findings for all boundary condition models. It is important to point out the minimal differences in maximum velocity and WSS, occurring along the proximal artery, between all models. Additionally, small dissimilarities in the volume weighted average velocity and area averaged WSS occur amongst the split flow and pressure w/ targeted mass flow rate simulations. Inexplicable differences in minimum WSS occurred between all models.

Table 4.5. Summary of boundary condition comparison model results.

		Peak Systole				Diastole
Model Type	**Run Time (hh:mm)**	**Maximum Velocity (m/s)**	**Volume Weighted Average Velocity (cm/s)**	**Maximum WSS (Pa)**	**Area Averaged WSS (Pa)**	**Minimum WSS (Pa)**
Zero Pressure	6:12	26.19	6.07	2.446	0.358	0.00098
Split Flow: 84% PV, 16% DA	8:49	26.19	8.95	2.442	0.597	0.00685
Pressure w/ Targeted Mass Flowrate	9:10	26.2	8.98	2.441	0.602	0.00275

4.6 2D Fistula Model

A 2-D model of the 51 mm geometry was created to determine if a more simplified and computationally affordable model could predict the same findings achieved with the 3-D model. The 2-D geometry was created using the Sketch toolbox in ANSYS SpaceClaim. As stated previously, the 2D model was computed with an 84% PV and 19% DA split flow outlet condition. Figure 4.25 shows the velocity streamlines for the two-dimensional model taken at peak sytole and diastole. For comparision, Figure 4.26 displays velocity streamlines from a cross sectional plane taken along the midplane of the 3D model. Additionally, Figure 4.27 displays velocity volume renderings of the 2D model. At peak systole, a maximum and area averaged velocity of 27.71 cm/s and 8.32 cm/s were computed. At the start of diastole, the maximum and area averaged velocity was 25.56 cm/s and 7.24 cm/s, respectively.

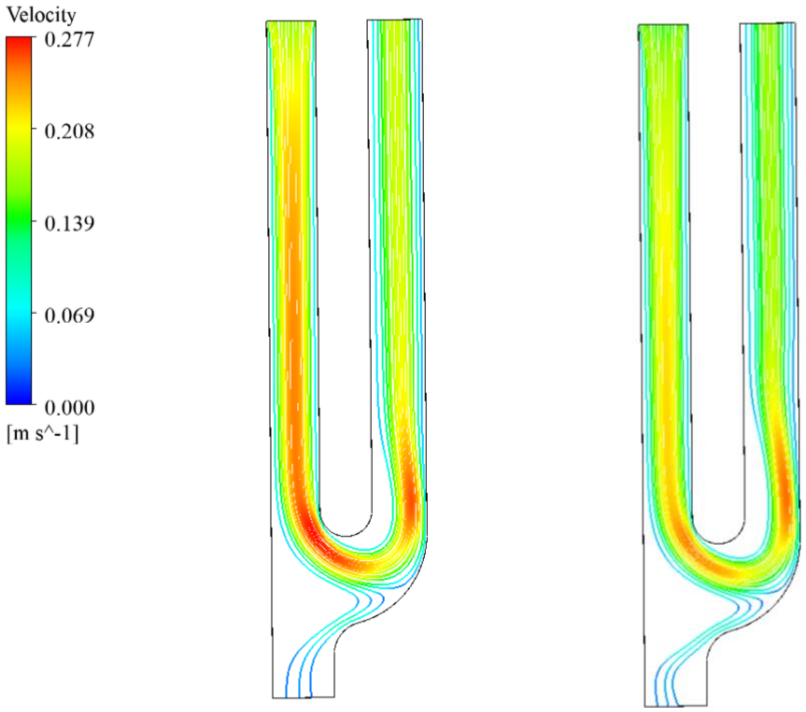

Figure 4.25. Velocity streamlines for the 2-D model. From left to right: Peak systole, diastole.

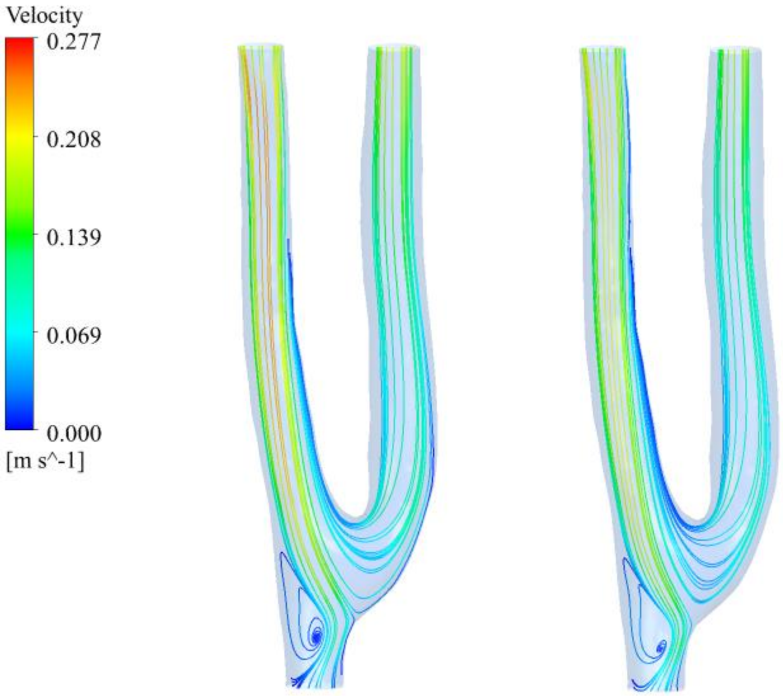

Figure 4.26. Velocity streamlines of a cross section taken along the midplane of the 3D model. From left to right: Peak systole, diastole.

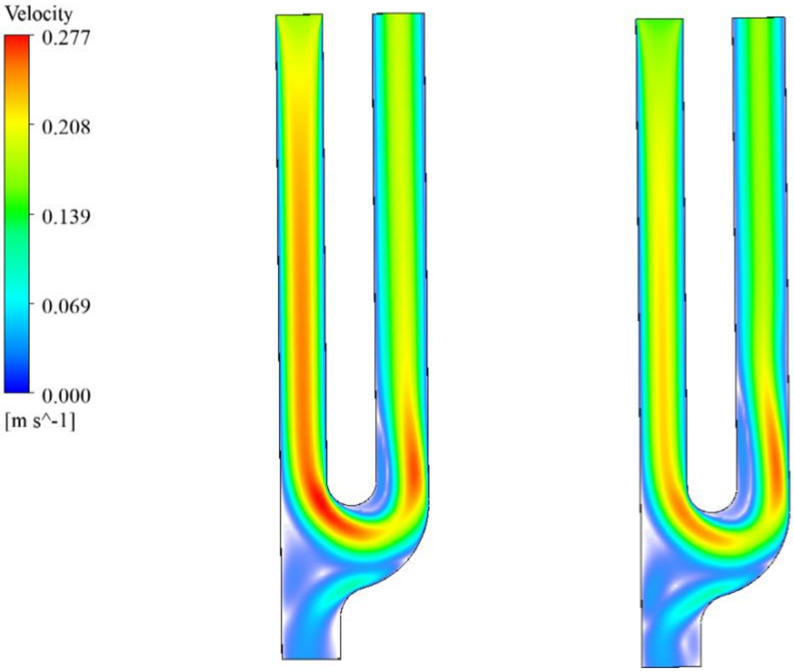

Figure 4.27. Velocity volume renderings for the 2-D model. From left to right: Peak systole, diastole.

Similar velocity flow patterns were found between the 2D and 3D models.

Figures 4.28 and 4.29 highlight the differences in maximum and average WSS for the 2D and 3D split flow simulations. The averaged TAWSS and OSI for the 2D split flow model was estimated at 0.625 Pa and 0.182. The 2D model significantly over-estimated the maximum shear stress occuring along the vessel wall. The pattern of TAWSS over the third cardiac cyle for the 2D model was very similar to the 3D model, however still over estimated by 50%.

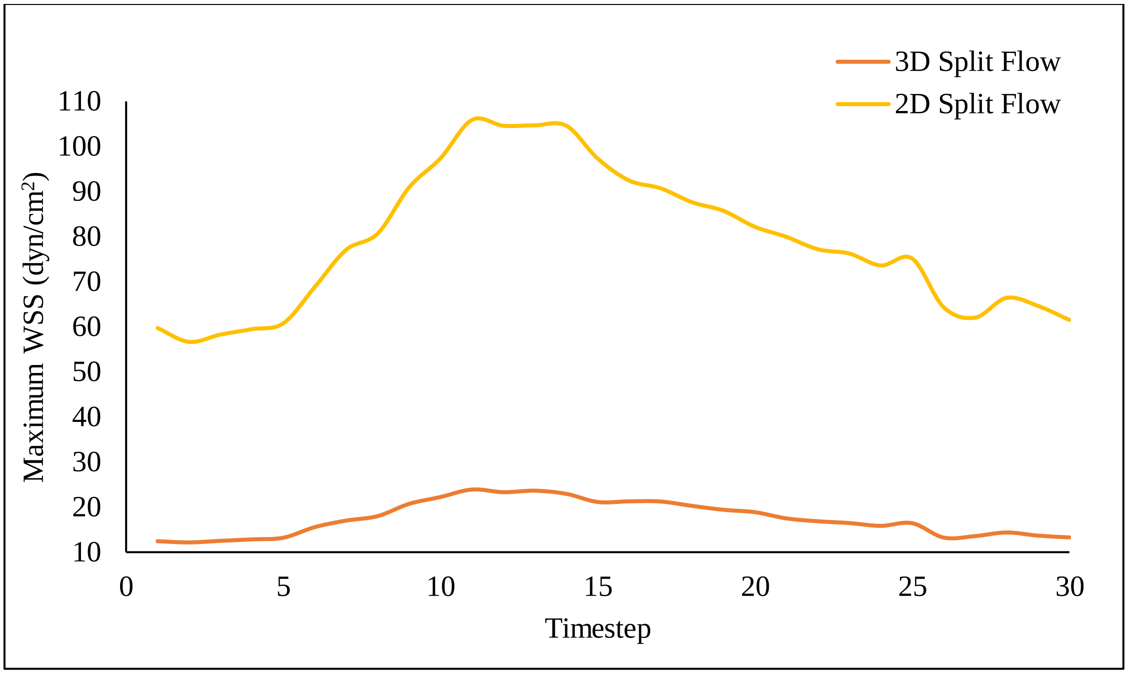

Figure 4.28. Maximum WSS for the 2D and 3D split flow models, plotted across 30 time points for the third cardiac cycle.

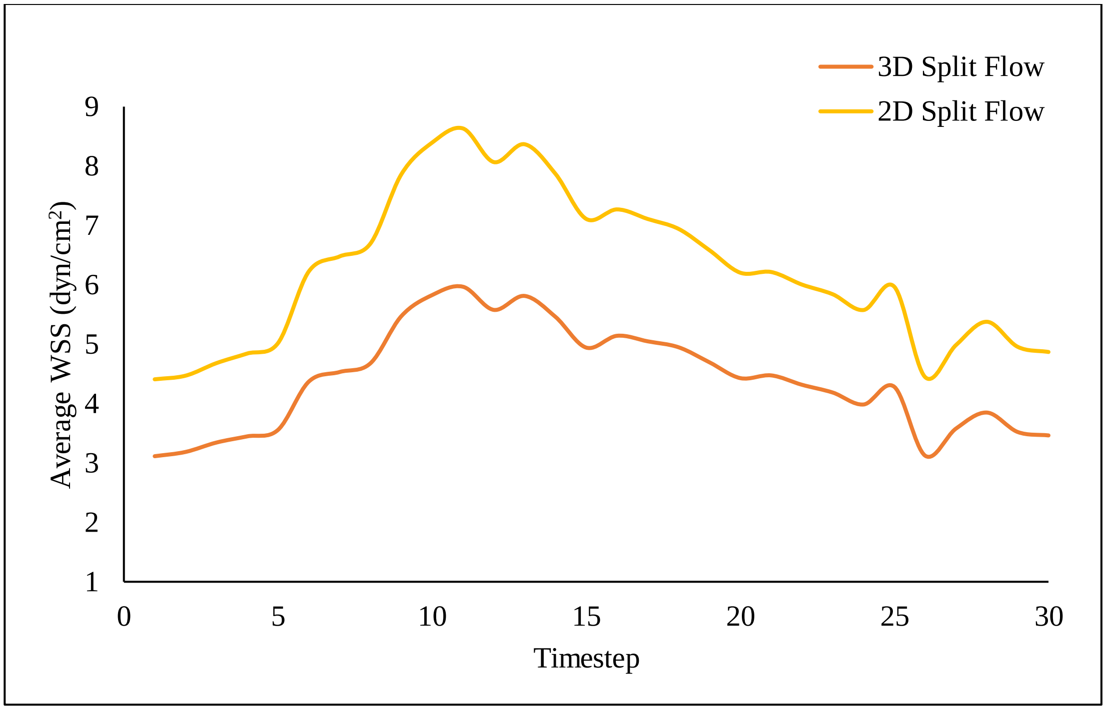

Figure 4.29. Average WSS for the 2D and 3D split flow models, plotted across 30 time points for the third cardiac cycle.

Table 4.6 provides a summary of results for the 2D and 3D split flow simulations. Minimal distinctions occurred in maximum velocity, average velocity, and minimum WSS results, however there are major differences in maximum WSS. Despite the expoentially faster run time and computational savings, the 2D model does not fully capture 3D model hemodynamics due to the diferentiations in findings.

Table 4.6. Summary of 2D and 3D split flow model results.

		Peak Systole				Diastole
Split Flow: 84% PV, 16% DA	**Run Time (hh:mm)**	**Maximum Velocity (cm/s)**	**Average Velocity (cm/s)**	**Maximum WSS (Pa)**	**Area Averaged WSS (Pa)**	**Minimum WSS (Pa)**
3D	8:49	26.19	7.58	2.442	0.597	0.00685
2D	1:05	27.71	8.33	10.863	0.868	0.00439

4.7 Fistula Banding Models

A fistula banding geometry was created from the 51 mm geometry, to investigate its impact on fistula hemodynamics. Three flow splits were applied to analyze the bandings' goal of limiting output.

Figures 4.30, 4.31, and 4.32 display velocity streamlines, velocity volume renderings, and WSS contours at both peak systole and diastole for the 84% PV, 16% DA split flow model. At peak systole, the maximum velocity was 41.23 cm/s where as, at the start of diastole the maximum velocity was 36.28 cm/s. The volume weighted average velocity at peak systole and diastole was calculated at 9.83 cm/s and 8.68 cm/s, respectively. At peak systole, the maximum WSS, minimum WSS, and average WSS was calculated at 7.92 Pa, 0.00201 Pa, and 0.806 Pa. At the start of diastole, the maximum WSS, minimum WSS, and average WSS was 6.46 Pa, 0.00385 Pa, and 0.701 Pa.

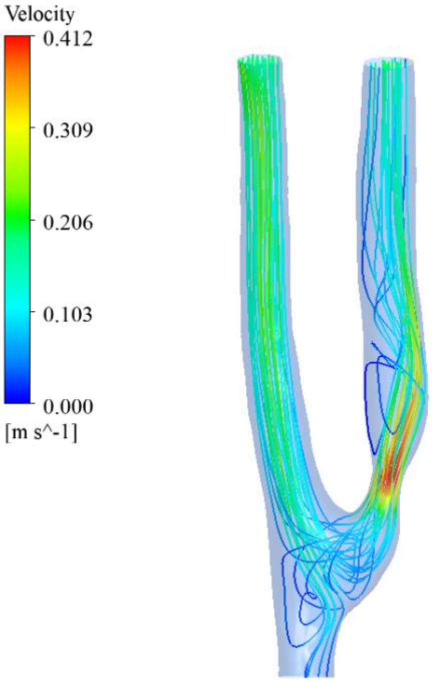

Figure 4.30. Velocity streamlines for the fistula banding model with 84/16% split flow. From left to right: Peak systole, diastole.

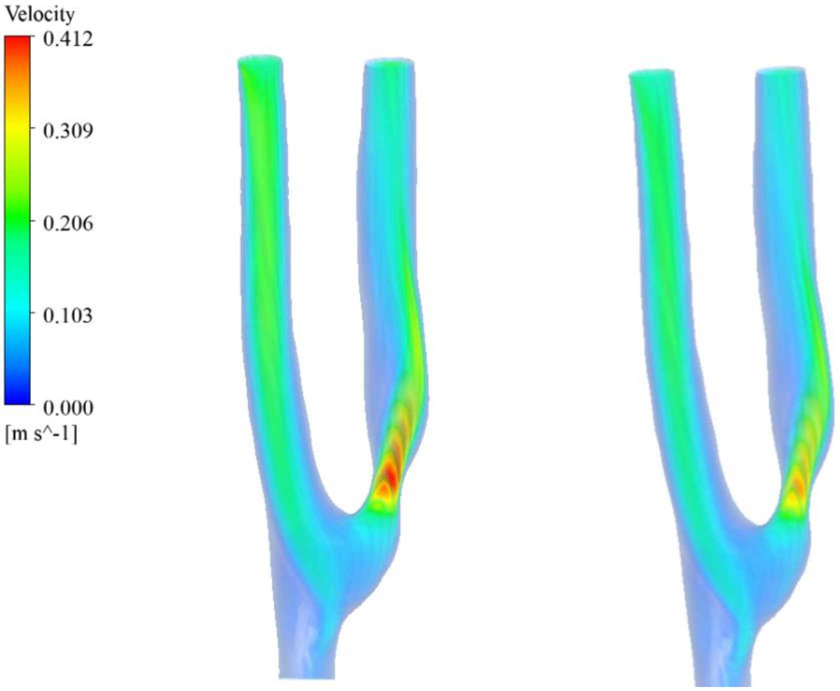

Figure 4.31. Velocity volume renderings for the fistula banding model with 84/16% split flow. From left to right: Peak systole, diastole.

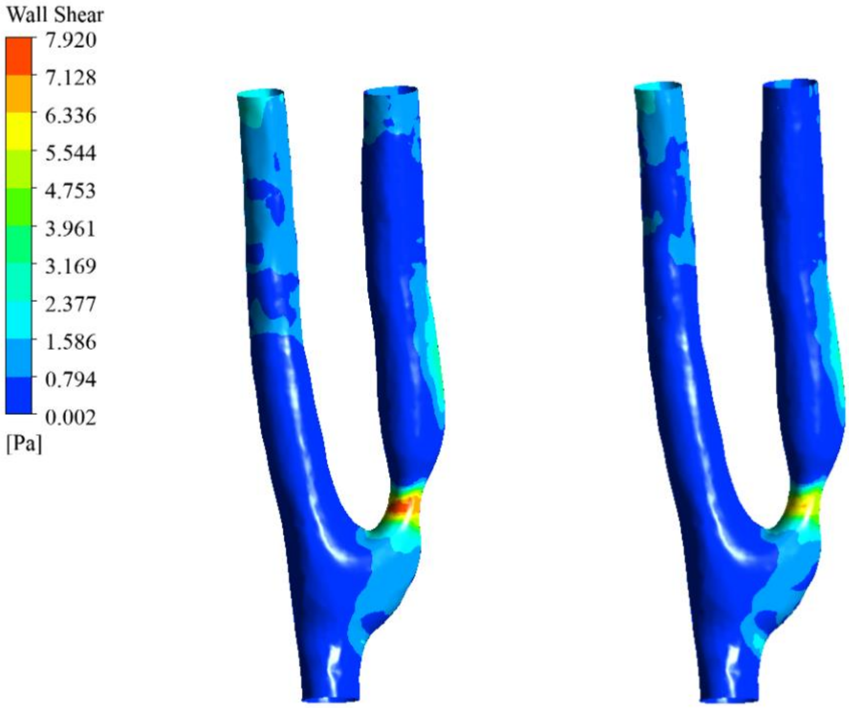

Figure 4.32. WSS contours for the fistula banding model with 84/16% split flow. From left to right: Peak systole, diastole.

Figures 4.33, 4.34, and 4.35 display the velocity streamlines, velocity volume renderings, and wall shear stress contours at peak systole and diastole for the 81% PV, 19% DA split flow model. At peak systole, the maximum velocity was 39.9 cm/s where as, at the start of diastole the maximum velocity was 35.06 cm/s. The volume weighted average velocity at peak systole and diastole was calculated at 9.67 cm/s and 8.53 cm/s, respectively. At peak systole, the maximum WSS, minimum WSS, and average WSS was calculated at 7.52 Pa, 0.00289 Pa, and 0.779 Pa. At the start of diastole, the maximum WSS, minimum WSS, and average WSS was 6.14 Pa, 0.00232 Pa, and 0.678 Pa.

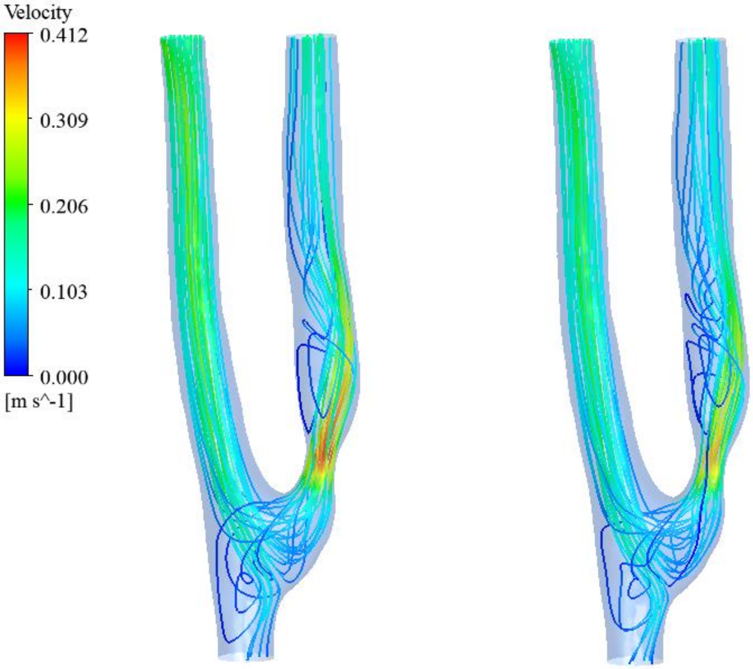

Figure 4.33. Velocity streamlines for the fistula banding model with 81/16% split flow. From left to right: Peak systole, diastole.

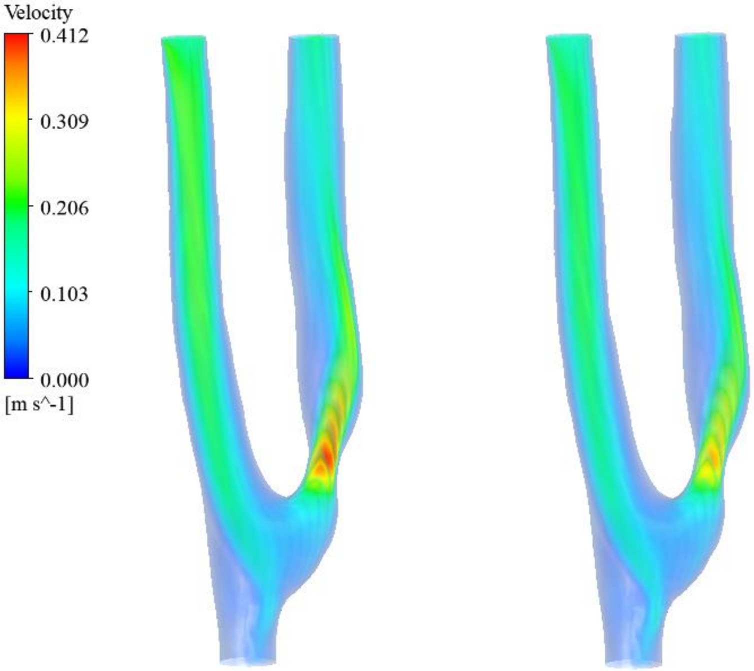

Figure 4.34. Velocity volume renderings for the fistula banding model with 81/16% split flow. From left to right: Peak systole, diastole.

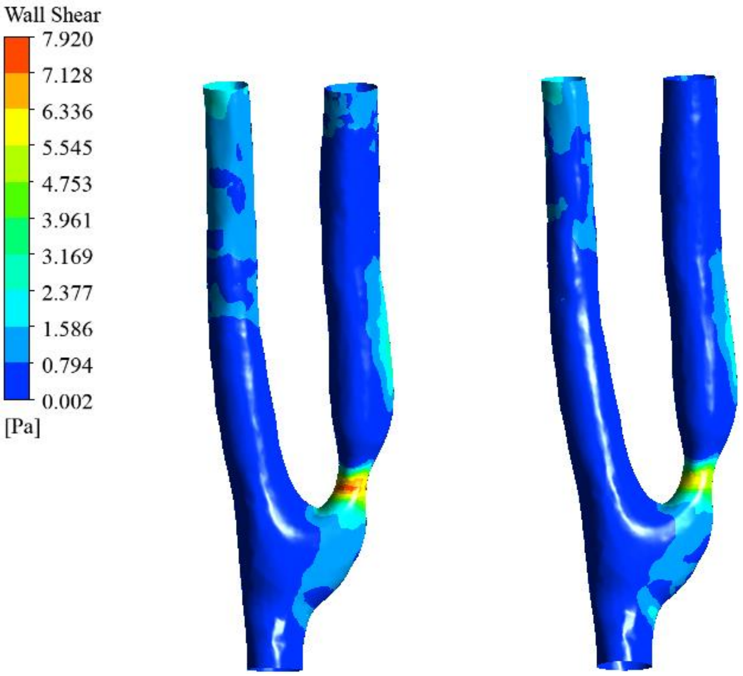

Figure 4.35. WSS contours for the fistula banding model with 81/16% split flow. From left to right: Peak systole, diastole.

Figures 4.36, 4.37, and 4.38 show the velocity streamlines, velocity volume renderings, and wall shear stress contours at peak systole and diastole for the 78% PV, 22% DA split flow model. At peak systole, the maximum velocity was 38.56 cm/s where as, at the start of diastole the maximum velocity was 33.91 cm/s. The volume weighted average velocity at peak systole and diastole was calculated at 9.51 cm/s and 8.40 cm/s, respectively. At peak systole, the maximum WSS, minimum WSS, and average WSS was calculated at 7.13 Pa, 0.00438 Pa, and 0.753 Pa. At the start of diastole, the maximum WSS, minimum WSS, and average WSS was 5.82 Pa, 0.00131 Pa, and 0.655 Pa.

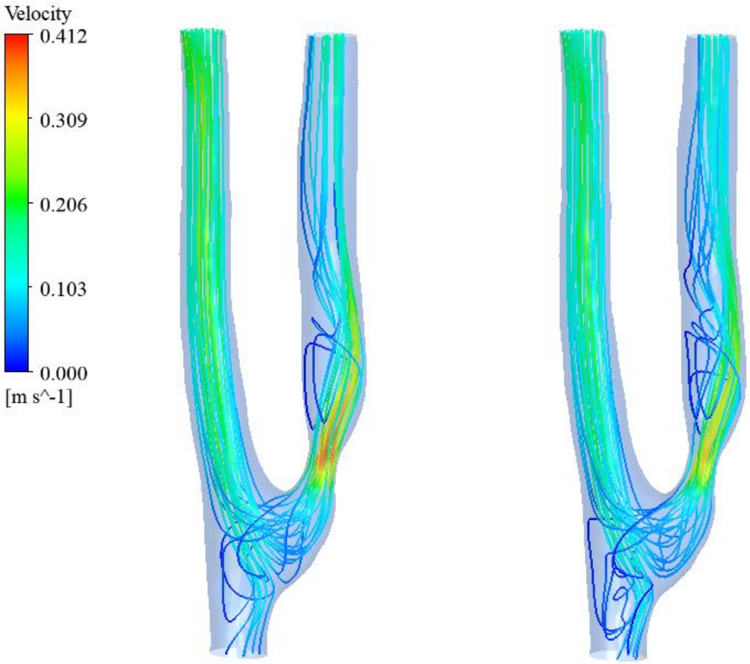

Figure 4.36. Velocity streamlines for the fistula banding model with 78/22% split flow. From left to right: Peak systole, diastole.

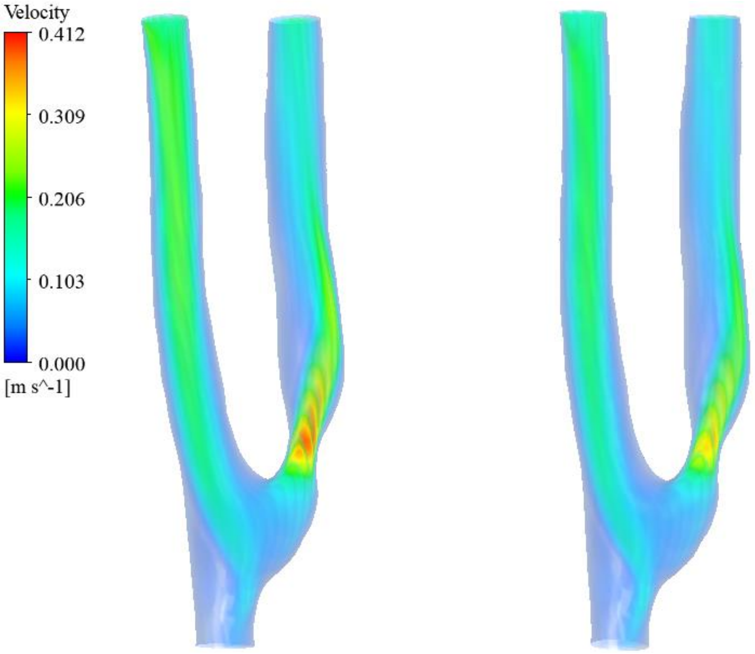

Figure 4.37. Velocity streamlines for the fistula banding model with 78/22% split flow. From left to right: Peak systole, diastole.

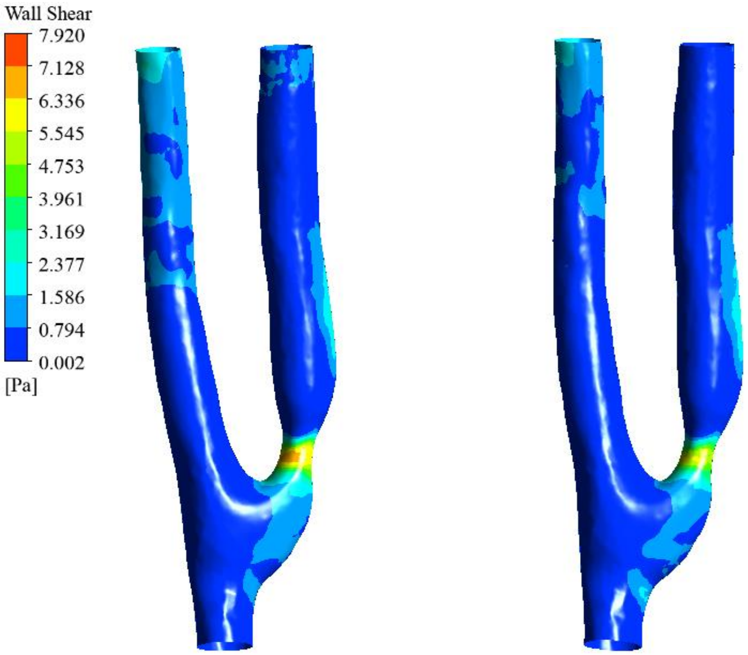

Figure 4.38. Velocity streamlines for the fistula banding model with 78/22% split flow. From left to right: Peak systole, diastole.

A summary of the findings for each flow split fistula banding model can be seen in Table 4.7. As the flow split towards the proximal vein decreased, all parameters of interested decreased as well, such as maximum velocity and WSS. Maximum velocity and WSS values were found at the banding location along the proximal vein. Additionally, areas of circulation occurred directly after the banding on the inner wall of the proximal vein.

Table 4.7. Summary of fistula banding split flow model resutls.

		Peak Systole				Diastole
Banding Split Flow Model	**Run Time (hh:mm)**	**Maximum Velocity (cm/s)**	**Volume Weighted Average Velocity (cm/s)**	**Maximum WSS (Pa)**	**Area Averaged WSS (Pa)**	**Minimum WSS (Pa)**
84% PV, 16% DA	6:40	41.23	9.83	7.92	0.806	0.00385
81% PV, 19% DA	6:32	39.9	9.67	7.52	0.779	0.00232
78% PV, 22% DA	6:27	38.56	9.51	7.13	0.753	0.00131

Table 4.8 provides results to compare the patient specific split flow model and the respective banding model (84% PV, 16% DA). The banding model presents elevated velocity and WSS values at peak systole and the start of diastole compared to the non banded model. More specifically, there is a 57.4% and 35.0% increase in peak systolic maximum velocity and WSS. Inversely, there was a 43.8% decrease in diastolic minimum WSS for the banded model.

Table 4.8. Patient specific split flow (84/16%) and banding model comparison results.

		Peak Systole				**Diastole**
Split Flow: 84% PV, 16% DA	**Run Time (hh:mm)**	**Maximum Velocity (cm/s)**	**Volume Weighted Average Velocity (cm/s)**	**Maximum WSS (Pa)**	**Area Averaged WSS (Pa)**	**Minimum WSS (Pa)**
Non-banded	8:49	26.19	8.95	2.442	0.597	0.00685
Banding	6:40	41.23	9.83	7.92	0.806	0.00385

Maximum and average WSS over the third cardiac cycle for the patient specific split flow and banding model are plotted in Figures 4.39 and 4.40. The averaged TAWSS and OSI for the banding model were calculated to be 0.586 Pa, and 0.173.

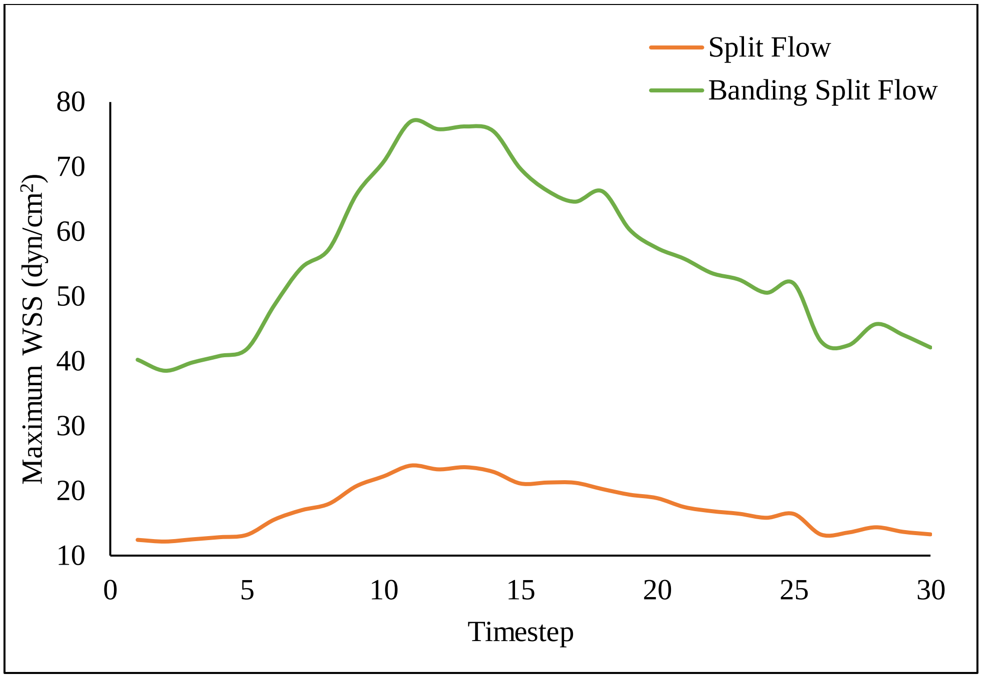

Figure 4.39. Maximum WSS for the split flow banding model, plotted across 30 time points for the third cardiac cycle.

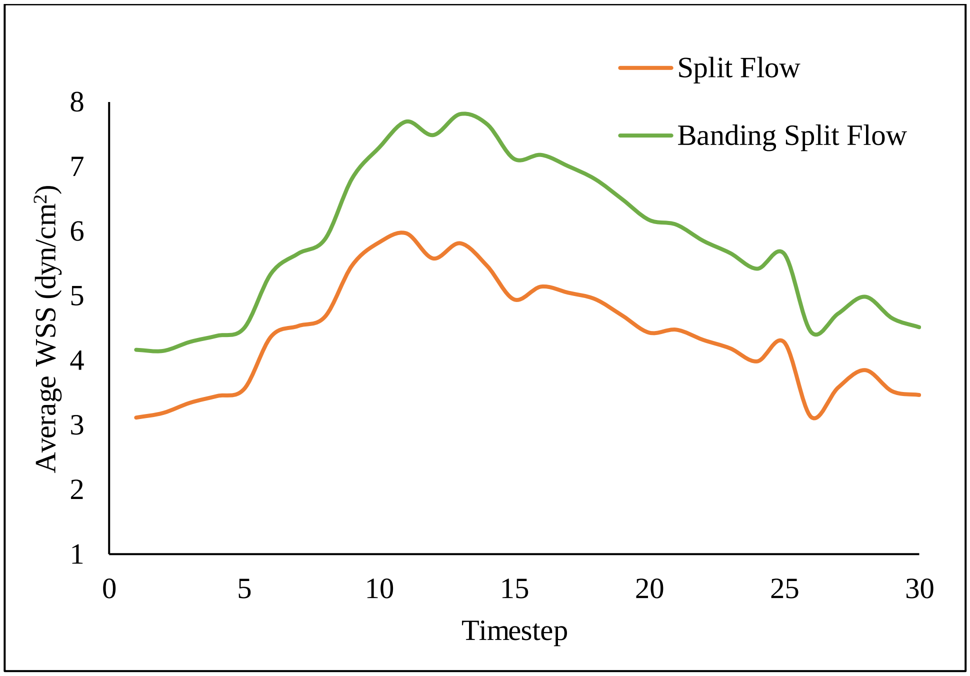

Figure 4.40. Average WSS for the split flow banding model, plotted across 30 time points for the third cardiac cycle.

4.8 Pulmonary Artery Model

CFD models of the pulmonary artery were previously computed by Pearce et al. [10]. Velocity streamlines, velicity volume renderings and WSS contours for the pulmonary artery of the same patient can be seen in Figures 4.41, 4.42, and 4.44. The pulmonary artery had a maximum velocity of 0.725 m/s. At peak systole this model had an average maximum velocity of 0.731 m/s and a volume weighted average velocity of 0.223 m/s. The maximum WSS at peak systole was 33.8 Pa and the minimum WSS found for the model was 0.0262 Pa. Across all three cardiac cycles, the model has an average maximum WSS of 33.8 and an average WSS of 3.714 Pa.

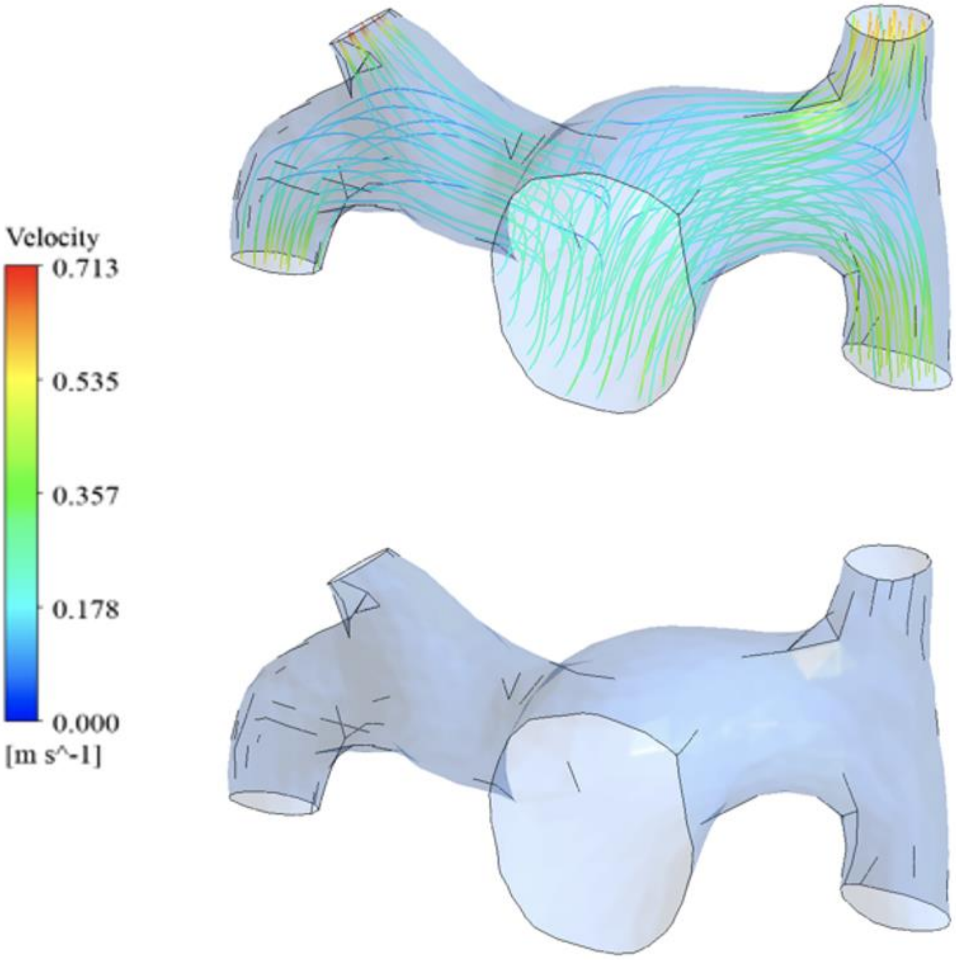

Figure 4.41. Velocity streamlines for the pulmonary artery. From top to bottom: Peak systole, start of diastole.

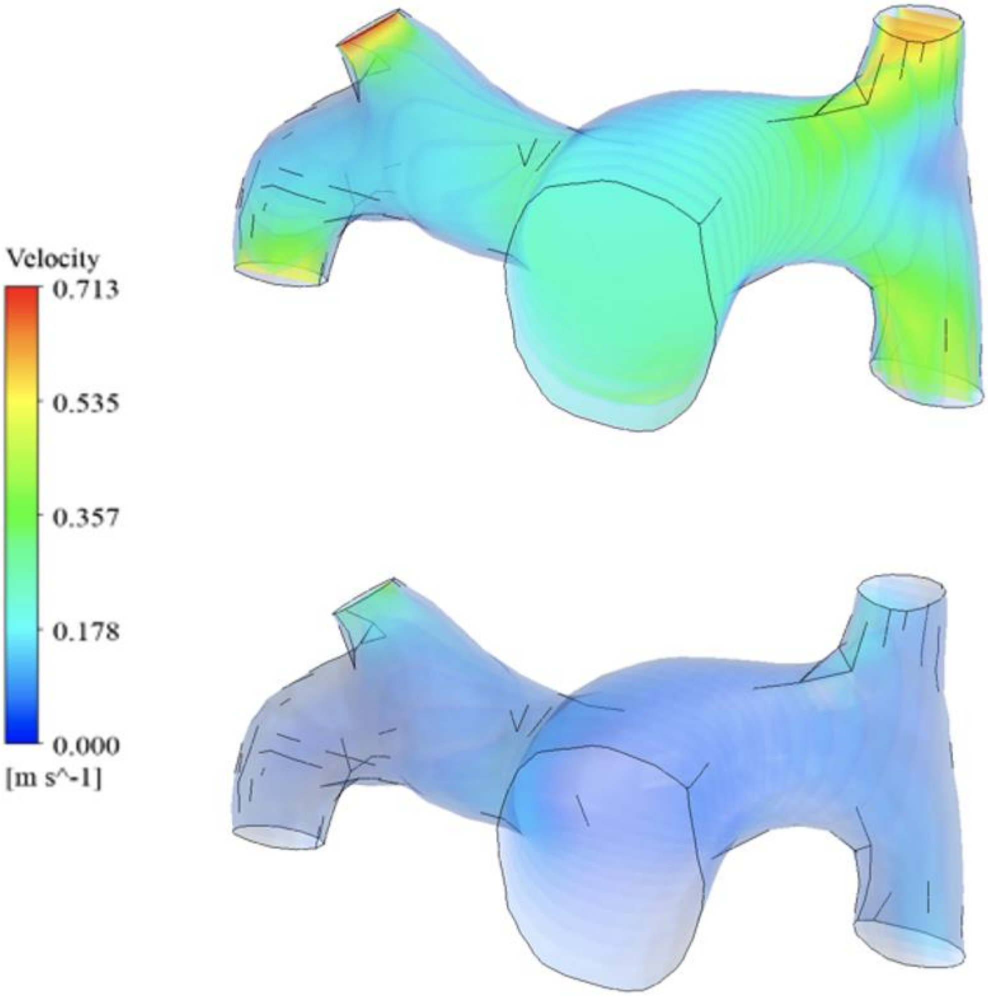

Figure 4.42. Velocity volume rendering for the pulmonary artery. From top to bottom: Peak systole, start of diastole.

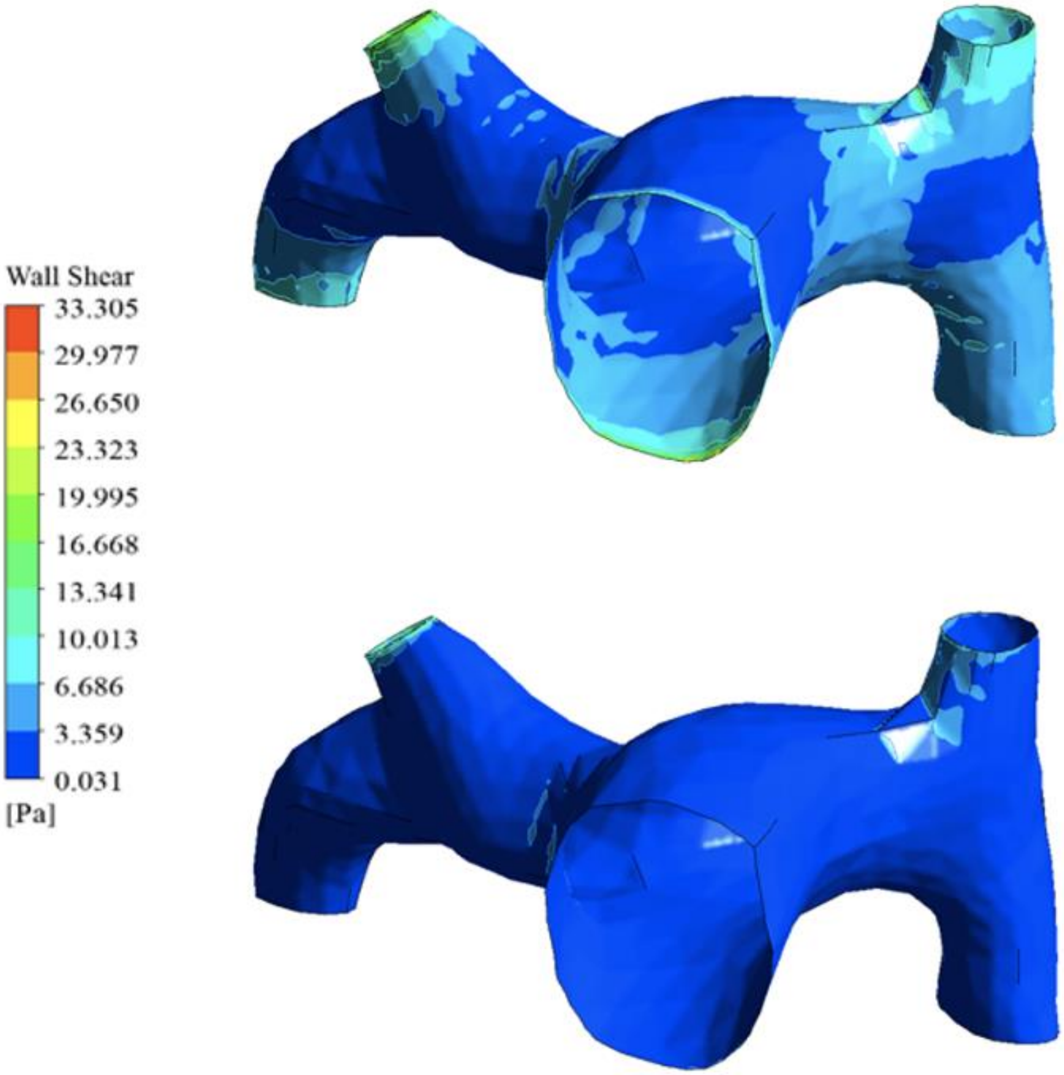

Figure 4.43. WSS contours for the pulmonary artery. From top to bottom: Peak systole, start of diastole.

Maximum and average WSS across the third cardiac cycle for the pulmonary artery can be seen in Figures 4.44 and 4.45, respectively. The PA model returned an averaged TAWSS value of 1.48 Pa throughout the cardiac cycle.

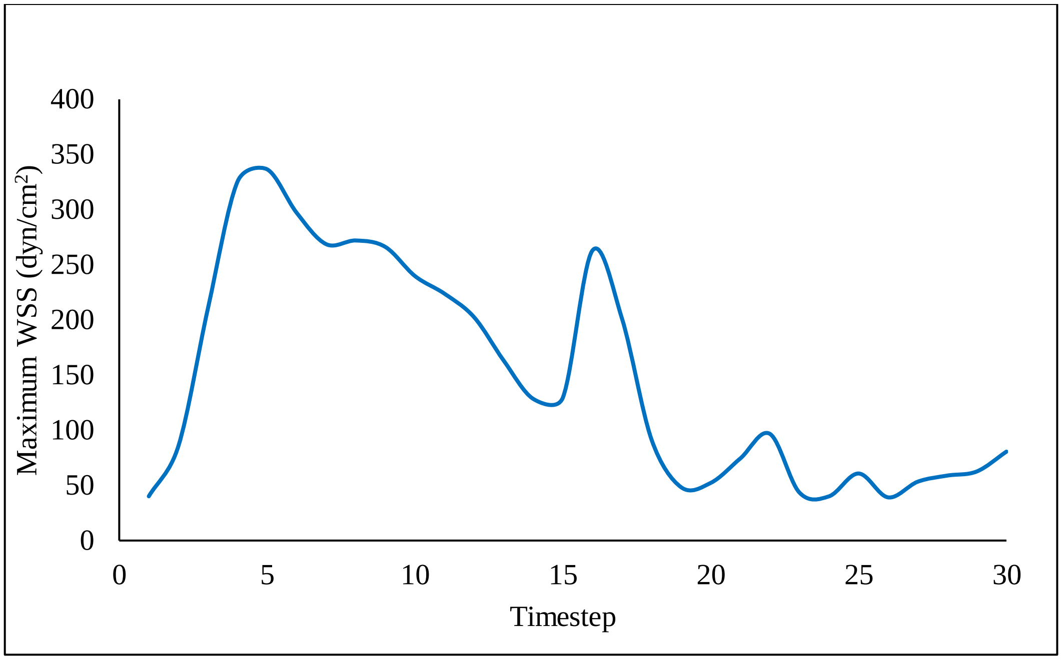

Figure 4.44. Maximum WSS for the pulmonary artery model, plotted across 30 time points for one cardiac cycle.

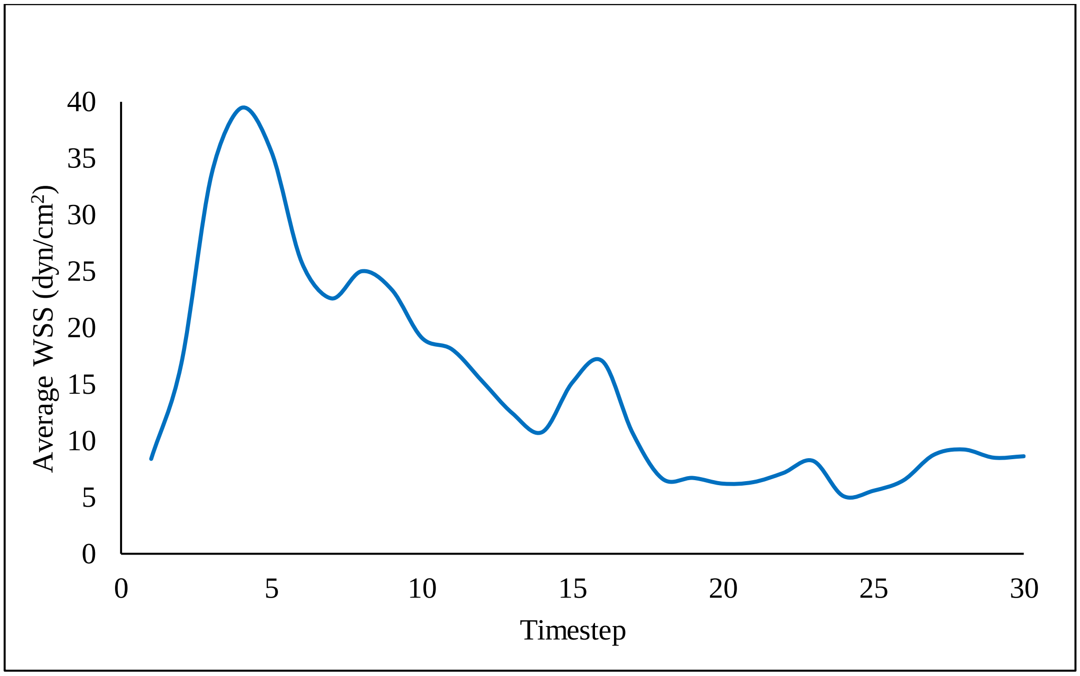

Figure 4.45. Average WSS for the pulmonary artery model, plotted across 30 time points for one cardiac cycle.

CHAPTER 5. DISCUSSION

Over 50 million Americans suffer from chronic kidney disease, which is a gradual loss of kidney function overtime [1]. If not treated properly, CKD can eventually progress to end stage renal disease, which is a life-threatening condition characterized by severely impaired renal function. Treatments for ESRD include replacement therapy by hemodialysis, with the creation of an arteriovenous fistula, peritoneal dialysis, and kidney transplant. AVFs are created by surgically connecting an artery and a vein to help facilitate dialysis. Even though this form of treatment is effective for blood filtration, recent studies have suggested connections between fistula creation (size and shape) and the development of pulmonary hypertension. Prominently 30–50% of CKD and ESRD patients have PH diagnosed via right heart catheterization [3]. In the case of those with ESRD developing PH, patients may be removed from the kidney transplant list. Consequently, an accurate prediction of those patients with AVFs at risk for developing PH is essential to establish an effective monitoring and intervention program. The aims outlined for this study were: 1) Develop a protocol for creating subject-specific computational fluid dynamics models of fistulas in patients with PH; 2) Correlate fistula hemodynamics with clinical measures of PH; and 3) Investigate the impact of fistula banding on fistula hemodynamics.

5.1 Aim 1: Develop a protocol for creating subject specific CFD models of fistulas in patients with PH

To address the first aim, geometry length, boundary condition, and 2D model comparisons were made to recommend the best protocol for CFD models of AVFs in PH patients. These mini studies were performed to determine the best approach for computationally modeling patient specific AVF hemodynamics and to ultimately provide a protocol for analyzing future patients.

Before analyzing models, model validation was performed. Due to the predictive limitations of computational modeling, validation is sought to check the accuracy of the model's representation of the real system. As previously discussed, PCMRI taken along the midplane of the proximal vein was used to validate the model. However, a portion of the data extracted from these images was used in the simulation setup. To calculate an accurate split flow between the two outlets (proximal vein and distal artery) the flowrate calculated at the proximal vein outlet was subtracted from the flowrate at the proximal artery inlet, which were both obtained from the PCMRI data. Despite this limitation the model remains an accurate predictor of fistula blood flow. Figure 4.4 compares the MATLAB and FLUENT generated velocity contours taken at two time points along the cardiac cycle. In the figure, there are some dissimilarities for the maximum velocity's location. The maximum velocity for the FLEUNT contours is at the center of the cross-section, whereas the maximum velocity for the MATLAB generated contours is towards the posterior side of the vein wall. Similar to the validations results along the pulmonary artery by Pearce et al., at Point A (peak systole) the two velocity contours are similar qualitatively and quantitatively, but the FLUENT model predicted slightly lower velocities [10]. This observation was also true for Point B (start of diastole). These results indicate similarities between the CFD modeling and the realistic blood flow through the AVF, but there are indeed differences. It is important to note that phase contrast imaging measures the thru plane velocity and the FLUENT contours demonstrate velocity magnitude at the slice. The thru plane velocity is the velocity of the fluid perpendicular to a specific cross-section, while the velocity magnitude incorporates all three (x, y, and z) components [10]. This discrepancy is measurement style could explain the small differences between the validation results.

The geometry length comparison simulations were performed as a preliminary step for this study. Evaluation of the simulation results with a more simplified geometry could provide a model with fewer mesh elements, reduced computational cost, and a more efficient simulation. Three geometry lengths were analyzed: 64 mm, 51 mm, and 36 mm. It should be noted that split flow outlet conditions were acquired from Ene-Iordache et al., where AVF geometry properties were consistent [44]. While there were significant differences in the maximum velocities for the 64 mm (37.19 cm/s), 51 mm (26.24 cm/s) and 36 mm (22.19 cm/s) models, there were minimal differences between the volume weighted average velocities for each model. Similar to maximum velocity, the 64 mm model had the highest volume weighted average velocity (9.64 cm/s), with the 51 mm (8.81 cm/s) and 36 mm (8.50 cm/s) models following slightly lower. The 64 mm and 51 mm models had almost equal area averaged velocity at peak systole and the start of diastole (7.54 cm/s v. 7.51 cm/s). Similarly, the 64 mm and 51 mm models had comparable maximum and minimum WSS values, with the 36 mm model indicating significant differences. The 64 mm model has the highest average WSS (0.647 Pa) with the 36 mm having the lowest average WSS (0.595 Pa). For additional comparison, cross sectional velocity contours were taken at the same location for each model. There were again, minimal differences in peak systolic and diastolic average planar velocity for the 64 mm (8.05 cm/s, 6.97 cm/s) and the 51 mm (8.08 cm/s, 6.99 cm/s) models. The 36 mm model had slightly higher values for peak systolic and diastolic average planar velocity (8.98 cm/s, 7.80 cm/s). The discrepancies between all models are thought to be due to the location and value of the inlet velocity waveform. To achieve the same flowrate for all models, the velocity waveform was adjusted based upon the area of the proximal artery inlet. The area of the 64 mm inlet was the smallest, creating a waveform with higher velocity values. The 51 mm model has a slightly larger inlet, with the 36 mm model having the largest inlet area, leading to slightly lower velocity values for these models. This also applies for WSS, where high WSS is a product of higher velocity. The 64 mm model had the highest velocity and WSS values. When looking at the planar average velocities, the 36 mm model had the highest velocity values, both at peak systole and the start of diastole, compared to the other two models. The difference is believed to be caused by the inlet being in closer proximity to the location of the cross-section taken for comparison. For the 64 mm and 51 mm models, the flow fully develops, which is limited for the 36 mm model. This phenomenon can be explained by calculating the entrance length (Equation 6).

$$El = 0.06\,Re \tag{6}$$

Entrance length is the distance from the entrance of the geometry, where flow begins, to the point where the flow becomes fully developed. In fully developed flow, the velocity profile remains unchanged along the direction of flow [53]. This parameter is dependent of the Reynolds number for the AVF, found to be 822.2 from PCMRI, which measures the ratio of inertial to viscous forces. The entrance length was calculated at 40.40 mm, which explains the differences for the 36 mm, compared to the 64- and 51-mm models. Ultimately, the 51 mm model was chosen to be used for the duration of the simulations. There were only slight differences between the results of the 64 mm and 51 mm models; however, the 51 mm model required less time to run to completion. A simplified model allows for increased simulation execution speed, more rapid time to CFD solution, and reduced MR scan time with insignificant impact on the results.

While the geometry length comparison study offered awareness to reducing computational cost and resources, analyzing the 51 mm model with varying boundary conditions provides fistula hemodynamic insights. Varying boundary conditions were studied to determine which user defined condition physiologically predicts the patient specific fluid flow. Three outlet boundary conditions were analyzed: zero pressure, 84% PV 16% DA split flow, and pressure with targeted mass flowrates. In each simulation, blood travels from the proximal artery to the anastomosis where it is divided (either towards the proximal vein or distal artery). With zero pressure outlet conditions, the blood flows towards either outlet assuming atmospheric pressure. This flow resulted in a flow split of 11.4% PV and 88.6% DA. Zero pressure outlets are known to be physiologically inaccurate, and do not depict realistic blood flow. On the other hand with split flow outlet boundary conditions, a user specified percentage of flow can be defined for each outlet. From the PC MRI data, a patient specific flowrate of 84% PV and 16% DA was perscribed. This boundary condition is more physiologically accurate, compared to the zero pressure conditions, supported by the MR validation results. Lastly, the outlet mass flow rates achieved from the split flow simulation were then applied to the pressure with targeted mass flow rate simulation. The mass flowrate was significant larger at the proximal vein (0.029086 kg/s) than the distal artery (0.00554 kg/s).

The outlet boundary condition simulations ran in this comparison study offered a variety of results. While there were almost no differences in peak systolic maximum velocity for the zero pressure (26.19 cm/s), split flow (26.19 cm/s), and pressure with targeted mass flow rate (26.20 cm/s) models, there were significant differences in volume weighted average velocity for the zero pressure (6.07 cm/s) compared to the other two simulations. The flow split and pressure with targeted mass flow rate models computed volume weighted average velocities of 8.95 cm/s and 8.98 cm/s, respectively. Similar maximum velocities (≈25.2 cm/s) were found by Van Trich et al. who had a comparable AVF flow rate of 1000 mL/min [40]. Maximum WSS for each simulation had little to no differences, whereas the area averaged WSS for the zero-pressure model varied by roughly 40% from the split flow and pressure with targeted mass flow rate models. Similarly, maximum WSS for each simulation was about 2.44 Pa. Minimum WSS for the zero pressure (0.00098 Pa), split flow (0.00685 Pa), and pressure with targeted mass flow rate (0.00275 Pa) simulations varied greatly. From the outlet boundary condition study, it is concluded that the patient specific outflow split condition is the most accurate for modeling patient specific flow.

Lastly, a 2D model was created to determine if fistula hemodynamics parameters discussed above could be estimated with a more computationally efficient method. Patient specific split flow outlet conditions (84% PV, 16% DA) were applied to the 2D model, and compared to the split flow 3D model. The peak systolic maximum velocity for the 3D (26.19 cm/s) and 2D (27.71 cm/s) differed minimally, whereas maximum WSS varied significantly. The maximum WSS for the 3D and 2D models was 2.442 Pa and 10.863 Pa, respectively. The 2D model overestimated the maximum WSS by 345%, which may be caused by the increased rigidity of the vessel walls in the 2D geometry. The volume weighted average velocity for the 3D (7.58 cm/s) and 2D (8.33 cm/s) models were also similar. Despite the reduced run time and similarities in velocity calculations, the 2D model significantly overestimates WSS. Also, WSS contours, volume renderings and other parameters of interest cannot be assessed with 2D modeling.

From the results presented in this section, a final protocol can be recommended. For this patient specific modeling approach, the 51 mm AVF geometry with patient specific split flow outlet boundary conditions is recommended as the best choice in modeling physiologically accurate flow. The 51 mm geometry can reduce computational cost and MR imaging time with no effect on results. The geometry length is subjective to this patient only and may not be true for further subjects. Additionally, the accuracy of the split flow outlet conditions is validated by the MRI extracted flowrate data. This recommendation is dependent only on the subject, where individualized patient split flows should be applied at the outlets. Computational results from this modeling setup can be used to determine a connection between AVF hemodynamics and the development of pulmonary hypertension.

5.2 Aim 2: Correlate fistula hemodynamics with clinical measures of PH

As previously mentioned, several studies have been completed to computationally model fistula hemodynamics. Studies by Sigovan et al. [41] and Bozzetto et al. [43] utilized non-contrast enhanced MRI to quantify blood flow through patient specific AVFs. Both groups found regions of low wall shear stress (< 1 Pa) along the inner curvature, subsequently corresponding to areas of recirculation. For the AVF model in this study, regions of low wall shear stress were also found along the anastomosis floor and heel, supported by Ene-Iordache et al. [44]. Similar to Decorato et al., maximum WSS values for the 51 mm split flow model are present along the proximal artery and the toe of the anastomosis (region of impacting flow) [54]. These areas may be subjected to wall damage induced by the high hemodynamic stress. Maximum WSS values noted by Decorato et al. were greater (9 Pa v. 2.44 Pa) than those computed in this study, which may be due to an elevated velocity waveform applied at the inlet in their study [54]. Theoretically, increased blood flow results in increased WSS for a constant vessel diameter. Van Tricht et al. stated that normal WSS values are below 0.76 Pa for veins, and for arteries it is known that they remodel to maintain WSS at about 1.5 Pa. Additionally, intimal hyperplasia is associated with WSS values in arteries below 1 Pa and above 35 Pa [55].

Oscillatory shear index and time averaged WSS are important hemodynamic parameters used to assess the risk of arteriosclerosis and endothelial dysfunction. OSI aims to quantify the deviation of WSS or flow from its average direction. Recent studies claim that low TAWSS (≤ 0.4 Pa) and high OSI (≥ 0.15) are risk factors for stenosis development, which may be related to inflammatory cell infiltration to the intima layer [56]. In this study, OSI for the zero pressure (0.0784), split flow (0.123), and pressure with targeted mass flow rate (0.0713) simulations were all in the acceptable range. Averaged TAWSS for the split flow (0.441 Pa) and pressure with targeted mass flow rate (0.517) simulations were acceptable however, the zero-pressure simulation computed averaged TAWSS of 0.264 Pa. The reduced TAWSS may be explained by the lack of flow towards the proximal vein, not allowing for adequate WSS for remodeling. Looking again at the split flow model, the anastomosis region had an OSI and averaged TAWSS of 0.109 and 0.363 Pa, respectively. The low averaged TAWSS indicated along the anastomosis could be the root cause of endothelial dysfunction and fistula failure. Bozzetto et al. developed surface maps of disturbed flow metrics, particularly OSI [43]. They found OSI values lower than 0.1 in the proximal artery and distal segment of the distal artery, with high values (0.3-0.5) located on the inner wall of the anastomosis and proximal segment of the distal artery. The OSI values obtained in this study are averaged across the full surface of the fistula (18.1 cm^2) [43]. Future work would benefit from OSI surface contours to better understand regions of recirculating flow. Parameters such as WSS spatial gradient, WSS temporal gradient, or WSS angle gradient are worth examining in future AVF patient-specific studies.

These computed areas of recirculation and low WSS can be explained by following the path of blood flow. Initially, blood flows from the proximal artery to the anastomosis. The flow directed towards the distal artery changes direction suddenly creating a wider area of recirculation and low velocity (and WSS) along the anastomosis floor, starting at the anastomosis down to the distal artery. Similar to Sigovan et al. slow flow was observed in the artery downstream of the anastomosis [41]. The flow entering the proximal vein collides against the outer wall near the anastomosis, resulting in recirculation and low velocity (and WSS) along the inner wall or heel of the anastomosis and high WSS at the point of collision [44].

To address aim 2, the findings from these computational models, both AVF and PA, can be used to hypothesize the correlation between fistulas in ESRD patients and the development of pulmonary hypertension. From literature, the hemodynamic effects of AVF implementation causes increased preload and decreased systemic vascular resistance leading to increased venous return and cardiac output [57]. Endothelial dysfunction in the vessels reduces the ability to adapt to the elevated cardiac output causing increased pulmonary artery pressures and the development of PH. As previously mentioned, the patient in this study has been diagnosed with PH, with a mPAP of 54 mmHg. This development can also be supported by the decreased systemic levels of nitric oxide found in PH patients. The production of nitric oxide, a vasodilator, is triggered by shear stress along the vessel walls [58]. With the regions of significantly low WSS along the AVF, the production of nitric oxide is then restricted, where vasoconstriction out plays vasodilation. The upsurge of vasoconstriction across all vasculatures increases pulmonary vascular resistance, again seen by the patient in this study. Most ESRD patients have preexisting left ventricular dysfunction, causing these hemodynamic changes to lead to more significant volume overload, pathologic remodeling, and eventually heart failure [57]. It is likely that PH in ESRD patients is resulted from a combination of right ventricular afterload, left-sided dysfunction, and elevated PA flow. It is important to diagnose high output fistulae in ESRD patients, especially with other risk factors like obesity, sleep apnea, and lung disease. In fact, the mortality risk for ESRD patients with or without PH is 4 times greater [58]. MR imaging also allowed for the comparison between the AVF and PA within the same prospective patient simultaneously. Previous studies by Dagli et al. [59] and Yigla et al. [3] revealed connections between end-stage renal disease patients undergoing dialysis, AVF flowrates, and onset pulmonary hypertension. Yigla et al. reported 40% of patients had increased systolic pulmonary artery pressures following AVF formation [3]. In patients with pulmonary hypertension, Dagli et al. found a mean AVF flow rate of 1.55 ± 0.207 L/min. In this study, the prospective patient has an AVF flowrate of 1.97 L/min, which is greater than the hypothesized limit of 1.5 L/min [60]. This AVF flowrate threshold is believed to be effective enough for dialysis without causing cardiac overload. Additionally, Tudoran et al. [61] found higher average AVF flow rates (≈1.2 L/min) in PH patients compared to normotensive patients (≈1 L/min). This group also found strong correlations between sPAP and AVF flowrates ($r = 0.583$, $p < 0.001$) as well as time spent on dialysis ($r = 0.702$, $p < 0.001$). With a larger patient population, including hypertensive and normotensive individuals, correlations and comparisons can be made like those computed by these studies.

From comparing AVF hemodynamics and clinical measures of PH, a few conclusions can be drawn. First, areas of low WSS and recirculation along the AVF contribute to endothelial dysfunction and fistula found in PH patients. This in turn could increase pulmonary vascular resistance or the ability of the cardiac vasculature to accommodate AVF- prompted increase in cardiac output. Additionally, the increase in cardiac output reduces systemic vascular resistance and therefore increases venous return, caused by the high output AVF, leading to increased pulmonary pressures. Again, elevated PVR and mPAP were measured via RHC for the patient in this study.

5.3 Aim 3: Investigate the impact of fistula banding on fistula hemodynamics

An initial step in treating ESRD patients with high output AVFs is to measure the effect of the AVF on PH development. Clinicians have established post diagnostic evaluation techniques to determine the relationship of AVF flow to PH by measuring pulmonary pressures before and after manually ligating the AV access. If a meaningful component of the patient's PH is related to the AVF, pulmonary hemodynamic measurements should be reduced significantly. Additionally, because WSS is considered a key factor for AVF failure and endothelial dysfunction, clinicians need a method to estimate this parameter noninvasively. The patient specific MRI-CFD protocol proposed in this study could provide physicians with a useful monitoring tool. Clinicians would be able to understand flow characteristics before and after surgical treatments to help the clinical decision-making process [62]. Additionally, a recent study by Du et al. proposed an ultrasound vector flow imaging (UVFI)-based WSS calculation technique that is more reliable than pulsed wave Doppler (PWD), especially when flow is not laminar at bifurcations [63]. The UVFI technique measures flow estimation of low velocities near the pulsating arterial wall, unlike PWD. Continuous monitoring of AVF flow can allow physicians to intervene when WSS or flow become unmanageable. Clinical manifestations associated with high output fistula include heart failure, pulmonary hypertension, which is the main focus of this study, and hand ischemia [64]. To control high-output fistulae, physicians may recommend fistula banding to regulate flow. Fistula banding involves inserting a balloon catheter in the vein with a tie placed to limit the vein to the diameter of the balloon [26]. To address aim 3, this banding technique was visualized computationally by applying a 5 mm theoretical band, and analyzing three flow splits: 84% PV, 16% DA (patient specific); 81% PV, 19% DA; and 78% PV, 22% DA. Sturm et al. claimed this band size and placement to be the most ideal [65]. Modeling the banded split flows provides insights into the hemodynamic conditions present in the banding implementation process.

The three split flow simulations presented results that were expected. As the percentage of flow towards the proximal vein decreases, velocity and WSS values also decrease, as seen by peak systolic maximum velocity for the 84% PV/16% DA (41.23 cm/s), 81% PV/19% DA (39.9 cm/s), and 78% PV/22% DA (38.56 cm/s) simulations. Significantly elevated WSS values are present at the band location (7.92 Pa), compared to the non-banded (2.44 Pa) model. Even though the banding model presented 225% higher WSS, the values are not great enough to cause damage to the vessel walls. Additionally, as the flow towards the distal artery increases, recirculating flow along the anastomosis floor and inner wall of the proximal vein subsides (Figures 4.30, 4.33, 4.36); however, it is still present, especially at the start of diastole. These regions of recirculating flow at low velocity and WSS values may be a concern for postoperative thrombosis, caused by inadequate measured flow during surgery [65]. Aschwanden et al. first recommended improving the banding technique by insonating, or using ultrasound guidance, to determine the adequate band distance from the anastomosis where less turbulent flow is expected [66]. CFD modeling by Lee et al., also indicated that a band placed further away from the anastomosis resulted in reduced post band turbulence. Additional studies reported significant changes in AVF output with only 0.5 mm variations in vessel banding diameter [64].

From this study it was learned that the size and location of the band determines the amount of flow reduction and its effect on cardiac output. Many studies have seen immediate improvements in cardiac output directly after AVF banding procedures. Chang et al. reported an initial and post-operative CO of 6.4 L/min and 4.27 L/min, respectively [57]. Additionally, there are limitations by applying split flow boundary conditions, where the amount of flow towards each outlet is controlled. With controlling the flow split it is difficult to determine how effective the band actually is to divert blood more distally. To overcome this limitation, pressure outlets can be applied to determine this effectiveness of banding for this patient. This ligation technique is promising, however, more research is needed to determine optimal size and shape of the band, to address the concerns over recorded high post-surgical thrombosis rates.

5.4 Limitations

The limitations of this work should be noted. First, there are many limitations with the use of computational modeling. While extremely useful in providing a fast and predictive alternative to simulate realistic fluid flow, *in silico* experiments are limited by simplifications and assumptions. Computational methods provide numerical approximations of the model, meaning an exact answer is not reached. Where this estimated solution is dependent upon a series of user-defined approximations. User-defined settings such as boundary conditions are limited by the knowledge about the specific mechanical properties of the vasculature being studied. For example, a pulsatile velocity waveform was applied at the inlet, unlike a blunt profile, because blood flow due to the pumping motion of the heart is considered pulsatile in nature. This also includes applying rigid wall assumptions to the vessel wall. No part of the AVF vessel wall is rigidly bound in the human body, however it was prescribed for increased numerical stability. Only one study to date, performed by Decorato et al. has proposed boundary conditions that allow for wall deformations with the use of FSI [54] The group found that WSS was overestimated by 10–13% in their rigid wall simulations however, the higher computational cost of FSI modeling reduces routine clinical use. Similarly, Colley et al. reported that rigid wall and non-slip condition assumptions are acceptable for modeling AVF hemodynamics, with expectations that WSS will be overestimated by up to 10% [67]. Furthermore, model validation was included to provide some support for the accuracy of the model's results.

Additionally, the imported patient specific geometries help to provide more clinically relevant solutions, but they are still limited by the spatial resolution of imaging machines. The reduced image quality of MRI compared to CT scans is a limitation in this study. Kharboutly et al. [68] utilized CT imaging with injected contrast bolus to reconstruct a 3D AVF geometry. This image modality allowed for more anatomically accurate geometry and the recognition of calcification zones along the vasculature. Despite the enhanced imaging capabilities with CT, MRI allows for velocity profile calculations through a cardiac cycle without the use of ionizing agents, which may risk harm to ESRD patients thought to develop PH. To improve the lack of clarity and image quality, a 3.0 T MR Machine could be utilized, with its higher signal to noise ratio and reduced scan time, compared to the claimed minimum standard 1.5 T magnetic strength.

Lastly, it is difficult to justify any statistical significance in the results due to only one subject being enrolled in the study. A larger and more diverse subject population should be used for future studies. A larger sample size will provide more convincing statistical analysis to justify clinical applications. With the current COVID-19 response measures, including vaccines, and the decline in the number of cases, subject recruitment should resume shortly.

5.5 Future Work

Based on the findings from this study and the existing limitations and gaps in literature, there are a few options for future studies moving forward. First, it is still unknown what influence the fistula has on the development of pulmonary hypertension. As mentioned beforehand, clinicians can manually compress the AVF and measure pulmonary pressures to observe immediate effects. However, to computationally model this relationship, future work should be done to create a patient specific lumped parameter model for the arteriovenous fistula and pulmonary artery. A generalized distributed lumped parameter (DLP) framework could be developed to compute flow and pressure dynamics for the PA and AVF simultaneously by considering various sources of energy dissipation [69]. Assuming the inclusion of a larger patient population, more justifiable comparisons can be made. Additionally, future studies should be completed to examine the effects of banding size and location for this patient. Sturm et al. reported desirable outlet pressures needed for adequate banding flow, which could be used as boundary conditions instead of the current flow split conditions [65]. Optimization of the band shape and location could further increase effectiveness and reduce post-operative malfunctions.

When correlated with PA measures, AVF hemodynamics may offer further insight into how AVF creation and its use during dialysis affects pressures in the right heart and PA. If a large and diverse patient population is recruited and analyzed, some of these metrics may offer physicians improved understanding about AVF monitoring and to make more informed surgical interventions to prevent the development of PH. This improvement could lead to fewer incidences of PH development in this patient population, more desirable healthcare outcomes, an enhanced quality of life, and a reduction of health disparities associated with this condition.

CHAPTER 6. CONCLUSION

Chronic kidney disease effects over 15% of adults in the United States and is associated with severely impaired renal function. Over time CKD can eventually progress and worsen into ESRD, resulting in permanent kidney failure that requires some form of replacement therapy. A full kidney transplant is the most ideal treatment but there are a limited number of donors, poor success rates for more obese patients, and several key restrictions on kidney recipients. Hemodialysis and peritoneal dialysis are the more common methods of ESRD management – with hemodialysis being the most common. Arteriovenous fistulas are crucial in delivering hemodialysis for ESRD patients, however adverse effects are exerted on the heart from increased workload demanded by the AV access output. The prevalence of pulmonary hypertension and onset heart failure is increasing in CKD and ESRD patients, insisting a better understanding of the relationship between both conditions for improved detection and prevention. The CFD-MRI protocol outlined in this study could allow physicians to model patient specific blood flow pre- and post- operatively to inevitably predict the effectiveness of surgical interventions. Additional methods, such as the ultrasound vector flow imaging based WSS calculation technique, could be implemented to monitor areas of low or high WSS. Providing physicians with clinically useful parameters for monitoring fistulas in patients at risk of developing PH is crucial for preventative surgical intervention. Fistula banding and venous flow management are promising techniques to control high outputs AVFs and divert more flow distally, however more research is needed to determine optimal size and location of the band. Prevention of PH is crucial not only for elevated arterial pressure, but also because ESRD patients with pulmonary hypertension are removed from the kidney transplant list.

REFERENCES

[1] Webster, Angela C, Associate Prof *et al*, "Chronic Kidney Disease," *Lancet (British Edition)*, vol. 389, *(10075)*, pp. 1238-1252, 2016; 2017.

[2] K. B. Quencer and M. Arici, "Arteriovenous Fistulas and Their Characteristic Sites of Stenosis," *American Journal of Roentgenology (1976)*, vol. 205, *(4)*, pp. 726-734, 2015.

[3] M. Yigla *et al*, "Pulmonary Hypertension in Hemodialysis Patients: An Unrecognized Threat: PULMONARY HYPERTENSION IN HEMODIALYSIS PATIENTS," *Seminars in Dialysis*, vol. 19, *(5)*, pp. 353-357, 2006.

[4] G. Simonneau and M. M. Hoeper, "The revised definition of pulmonary hypertension: Exploring the impact on patient management," European Heart Journal Supplements, vol. 21, (K), pp. K4-K8, 2019.

[5] C. A. O'Callaghan, *The Renal System at a Glance*. (4th;4th; ed.) 2017; 2016.

[6] Les Laboratoires Servier, “SMART - Servier Medical ART - 3000 free medical images. Licensed under a creative commons attribution 3.0 license,” 2018. [Online]. Available: https://smart.servier.com/. [Accessed: 22-May-2019].

[7] B. Long, A. Koyfman and C. M. Lee, "Emergency medicine evaluation and management of the end stage renal disease patient," *American Journal of Emergency Medicine*, vol. 35, *(12)*, pp. 1946-1955, 2017.

[8] C. Nickson, “Pulmonary Hypertension Echocardiography • LITFL • CCC.” [Online]. Available: https://litfl.com/pulmonary-hypertension-echocardiography/. [Accessed: 22- October-2021].

[9] G. Simonneau *et al.*, “Haemodynamic definitions and updated clinical classification of pulmonary hypertension.,” *Eur. Respir. J.*, vol. 53, no. 1, 2019.

[10] D. Pearce, S. George, and East Carolina University. Department of Engineering, *Fluid-Structure Interaction Modeling of Pulmonary Artery Blood Flow in End-Stage Renal Disease Patients.* 2020.

[11] M. R. Fisher *et al*, "Accuracy of Doppler Echocardiography in the Hemodynamic Assessment of Pulmonary Hypertension," *American Journal of Respiratory and Critical Care Medicine,* vol. 179, *(7),* pp. 615-621, 2009.

[12] G. Acarturk *et al*, "The relationship between arteriovenous fistula blood flow rate and pulmonary artery pressure in hemodialysis patients," *International Urology and Nephrology,* vol. 40, *(2),* pp. 509-513, 2008.

[13] A. Unal *et al.*, “The long-term effects of arteriovenous fistula creation on the development of pulmonary hypertension in hemodialysis patients,” *Hemodial. Int.*, vol. 14, no. 4, pp. 398–402, Oct. 2010.

[14] P. Amelia *et al*, "Role of echocardiography in evaluating patients with pulmonary hypertension secondary to congenital heart diseases in economically developing countries," *Progress in Pediatric Cardiology,* vol. 64, pp. 101449, 2022.

[15] M. R. Fisher *et al,* "Accuracy of Doppler Echocardiography in the Hemodynamic Assessment of Pulmonary Hypertension," *American Journal of Respiratory and Critical Care Medicine,* vol. 179, *(7),* pp. 615-621, 2009.

[16] A. Shujaat, A. A. Bajwa, F. Al-Saffar, J. Bellardini, L. Jones, and J. D. Cury, "Diagnostic accuracy of echocardiography combined with chest CT in pulmonary hypertension," Clin. Respir. J., vol. 12, no. 3, pp. 948–952, Mar. 2018, doi: 10.1111/crj.12610.

[17] D. X. Augustine et al, "Echocardiographic assessment of pulmonary hypertension: a guideline protocol from the British Society of Echocardiography," Echo Research and Practice, vol. 6, (3), pp. X1, 2019.

[18] A. Lungu *et al,* "Diagnosis of Pulmonary Hypertension from Magnetic Resonance Imaging–Based Computational Models and Decision Tree Analysis," *Pulmonary Circulation,* vol. 6, *(2),* pp. 181-190, 2016.

[19] C. S. Johns *et al,* "Diagnosis of Pulmonary Hypertension with Cardiac MRI: Derivation and Validation of Regression Models," *Radiology,* vol. 290, *(1),* pp. 61-68, 2019.

[20] A. Lungu, J. M. Wild, D. Capener, D. . Kiely, A. Swift, and D. R. Hose, "MRI model- based non-invasive differential diagnosis in pulmonary hypertension," J. Biomech., vol. 47, no. 12, pp. 2941–2947, Sep. 2014, doi: 10.1016/J.JBIOMECH.2014.07.024.

[21] V. O. Kheyfets *et al,* "4D magnetic resonance flow imaging for estimating pulmonary vascular resistance in pulmonary hypertension," *Journal of Magnetic Resonance Imaging,* vol. 44, *(4),* pp. 914-922, 2016.

[22] M. M. Sieren *et al*, "Comparison of 4D Flow MRI to 2D Flow MRI in the pulmonary arteries in healthy volunteers and patients with pulmonary hypertension," *PloS One,* vol. 14, *(10),* pp. e0224121-e0224121, 2019.

[23] L. Antiga et al, "An image-based modeling framework for patient-specific computational hemodynamics," *Medical & Biological Engineering & Computing,* vol. 46, (11), pp. 1097-1112, 2008.

[24] P. D. Morris et al, "Computational fluid dynamics modelling in cardiovascular medicine," Heart (British Cardiac Society), vol. 102, (1), pp. 18-28, 2016.

[25] J. Tu, K. Inthavong, and K. K. Wong, "Computational hemodynamics – theory, modelling and applications," *Biological and Medical Physics, Biomedical Engineering*, 2015. doi:10.1007/978-94-017-9594-4

[26] FDA, "Benefits and Risks | FDA," 2017. https://www.fda.gov/radiation-emitting-products/mri-magnetic-resonance-imaging/benefits-and-risks (accessed May 22, 2019).

[27] V. O. Kheyfets *et al*, "Considerations for Numerical Modeling of the Pulmonary Circulation—A Review With a Focus on Pulmonary Hypertension," *Journal of Biomechanical Engineering,* vol. 135, *(6),* pp. 61011-15, 2013.

[28] "What is the source of mesh quality spectrum? - ANSYS learning forum," Ansys Innovation Space, https://forum.ansys.com/forums/topic/what-is-the-source-of-mesh-quality-spectrum/ (accessed Jun. 7, 2023).

[29] LEAP CFD Team, “Tips & Tricks: Convergence and mesh independence study,” Computational Fluid Dynamics CFD Blog, https://www.computationalfluiddynamics.com.au/convergence-and-mesh-independent-study/ (accessed Jun. 7, 2023).

[30] I. E. Vignon and C. A. Taylor, “Outflow boundary conditions for one-dimensional finite element modeling of blood flow and pressure waves in arteries,” *Wave Motion*, vol. 39, no. 4, pp. 361–374, 2004. doi:10.1016/j.wavemoti.2003.12.009

[31] “ANSYS FLUENT 12.0 User’s Guide.” ANSYS Inc., Jan. 30, 2009

[32] “What is Convergence?” NAFEMS, https://www.nafems.org/publications/guidelines-for-good-convergence-in-cfd/what-is-convergence/ (accessed Jun. 7, 2023).

[33] M. Kuron, “3 criteria for assessing CFD Convergence,” Engineering.com, https://www.engineering.com/story/3-criteria-for-assessing-cfd-convergence (accessed Jun. 7, 2023).

[34] T. Papaioannou and C. Stefanadis, “Vascular Wall Shear Stress: Basic Principles and Methods,” Hell. J. Cardiol., vol. 46, pp. 9–15, 2005, Accessed: May 31, 2019. [Online]. Available: https://www.researchgate.net/publication/7929606.

[35] L. H. Timmins et al., “Focal Association Between Wall Shear Stress and Clinical Coronary Artery Disease Progression,” Ann. Biomed. Eng., vol. 43, no. 1, pp. 94–106, Jan. 2015, doi: 10.1007/s10439-014-1155-9.

[36] P. D. Morris et al, "Computational fluid dynamics modelling in cardiovascular medicine," *Heart (British Cardiac Society)*, vol. 102, (1), pp. 18-28, 2016.

[37] D. Pike et al, "High resolution hemodynamic profiling of murine arteriovenous fistula using magnetic resonance imaging and computational fluid dynamics," *Theoretical Biology and Medical Modelling,* vol. 14, (1), pp. 5-5, 2017.

[38] G. T. Carroll et al, "Wall Shear Stresses Remain Elevated in Mature Arteriovenous Fistulas: A Case Study," *Journal of Biomechanical Engineering,* vol. 133, (2), pp. 021003-021003, 2011.

[39] T. A. Manos *et al*, "Local Hemodynamics and Intimal Hyperplasia at the Venous Side of a Porcine Arteriovenous Shunt," *IEEE Transactions on Information Technology in Biomedicine,* vol. 14, *(3),* pp. 681-690, 2010.

[40] I. Van Tricht *et al*, "Comparison of the hemodynamics in 6 mm and 4–7 mm hemodialysis grafts by means of CFD," *Journal of Biomechanics,* vol. 39, *(2),* pp. 226-236, 2006.

[41] M. Sigovan et al, "Vascular Remodeling in Autogenous Arterio-Venous Fistulas by MRI and CFD," *Annals of Biomedical Engineering*, vol. 41, (4), pp. 657-668, 2013.

[42] L. Jia et al, "Effects of wall shear stress in venous neointimal hyperplasia of arteriovenous fistulae," Nephrology (Carlton, Vic.), vol. 20, (5), pp. 335-342, 2015.

[43] M. Bozzetto, B. Ene-Iordache, P. Brambilla, and A. Remuzzi, “Characterization of the flow-field in a patient-specific model of arteriovenous fistula for hemodialysis,” 2016. Accessed: March 16, 2022. [Online]. Available: http://villacamozzi.marionegri.it/~bogdan/downloads/Bozzetto_CAE_2016.pdf.

[44] B. Ene-Iordache and A. Remuzzi, "Disturbed flow in radial-cephalic arteriovenous fistulae for haemodialysis: Low and oscillating shear stress locates the sites of stenosis," Nephrology, Dialysis, Transplantation, vol. 27, (1), pp. 358-368, 2012.

[45] S. Sivanesan, T. V. How and A. Bakran, "Sites of stenosis in AV fistulae for haemodialysis access," Nephrology, Dialysis, Transplantation, vol. 14, (1), pp. 118-120, 1999.

[46] H. Kim et al., “Arteriovenous graft modeling and Hemodynamic Interpretation,” Open Journal of Fluid Dynamics, vol. 02, no. 04, pp. 324–330, 2012. doi:10.4236/ojfd.2012.24a040

[47] C. Cunnane, E. M. Cunnane and M. T. Walsh, "A Review of the Hemodynamic Factors Believed to Contribute to Vascular Access Dysfunction," Cardiovascular Engineering and Technology, vol. 8, (3), pp. 280-294, 2017.

[48] C. Cunnane *et al*, "The presence of helical flow can suppress areas of disturbed shear in parameterized models of an arteriovenous fistula," *International Journal for Numerical Methods in Biomedical Engineering,* vol. 35, *(12),* pp. e3259-n/a, 2019.

[49] J. Moon et al, "Considerations of blood properties, outlet boundary conditions and energy loss approaches in computational fluid dynamics modeling," Neurointervention, vol. 9, (1), pp. 1-8, 2014.

[50] N. Rao *et al.*, “Effects of arteriovenous fistula ligation on cardiac structure and function in kidney transplant recipients,” *Circulation*, vol. 139, no. 25, pp. 2809–2818, 2019. doi:10.1161/circulationaha.118.038505

[51] H. Lee et al, "Dynamic Banding (DYBAND) Technique for Symptomatic High-Flow Fistulae," Vascular and Endovascular Surgery, vol. 54, (1), pp. 5-11, 2020.

[52] Theresa, “How to keep the Courant number below 1,” SimScale, https://www.simscale.com/knowledge-base/what-is-a-courant-number/ (accessed Jun. 7, 2023).

[53] C. Young, “Entrance length in fluent: Understanding its impact on flow simulations,” EngineerExcel, https://engineerexcel.com/entrance-length-in-fluent/ (accessed Jun. 8, 2023).

[54] I. Decorato *et al*, "Numerical study of the influence of wall compliance on the hemodynamics in a patient-specific arteriovenous fistula," in 2011.

[55] I. Van Tricht et al, "Hemodynamics and complications encountered with arteriovenous fistulas and grafts as vascular access for hemodialysis: a review," Annals of Biomedical Engineering, vol. 33, (9), pp. 1142-1157, 2005.

[56] A. M. Moerman *et al*, "The Correlation Between Wall Shear Stress and Plaque Composition in Advanced Human Carotid Atherosclerosis," *Frontiers in Bioengineering and Biotechnology*, vol. 9, pp. 828577-828577, 2022.

[57] E. D. WARNER *et al*, "High-Output Heart Failure, Pulmonary Hypertension and Right Ventricular Failure in Patients with Arteriovenous Fistulas: A Call to Action," *Journal of Cardiac Failure*, vol. 29, *(6)*, pp. 979-981, 2023.

[58] J. Devasahayam *et al*, "Pulmonary hypertension in end-stage renal disease," *Respiratory Medicine*, vol. 164, pp. 105905-105905, 2020.

[59] C. E. Dagli *et al*, "Prevalence of and Factors Affecting Pulmonary Hypertension in Hemodialysis Patients”, *Respiration,* vol. 78, *(4),* pp. 411-415, 2009.

[60] C. Basile *et al,* "The relationship between the flow of arteriovenous fistula and cardiac output in haemodialysis patients," *Nephrology, Dialysis, Transplantation,* vol. 23, *(1),* pp. 282-287, 2008.

[61] M. Tudoran *et al*, "Pulmonary hypertension in patients with end stage renal disease undergoing hemodialysis," *Nigerian Journal of Clinical Practice,* vol. 23, *(2),* pp. 198-204, 2020.

[62] B. Chung and J. R. Cebral, "CFD for Evaluation and Treatment Planning of Aneurysms: Review of Proposed Clinical Uses and Their Challenges," *Annals of Biomedical Engineering,* vol. 43, *(1),* pp. 122-138, 2015.

[63] Y. Du *et al*, "Wall Shear Stress Measurements Based on Ultrasound Vector Flow Imaging: Theoretical Studies and Clinical Examples," *Journal of Ultrasound in Medicine,* vol. 39, *(8),* pp. 1649-1664, 2020.

[64] G. A. Beathard, E. D. Dillavou, I. Davidson, and K. A. Collins, “High-flow hemodialysis arteriovenous access,” *UpToDate*, May 2022.

[65] M. Sturm *et al*, "The haemodynamic effect of an adjustable band in an arteriovenous fistula," *Computer Methods in Biomechanics and Biomedical Engineering,* vol. 20, *(9),* pp. 949-957, 2017.

[66] M. Aschwanden et al, "Dialysis access-associated steal syndrome: The intraoperative use of duplex ultrasound scan," Journal of Vascular Surgery, vol. 37, (1), pp. 211-213, 2003.

[67] E. Colley *et al*, "A longitudinal study of the arterio-venous fistula maturation of a single patient over 15 weeks," *Biomechanics and Modeling in Mechanobiology,* vol. 21, *(4),* pp. 1217-1232, 2022.

[68] Z. Kharboutly *et al*, "Investigations into the relationship between hemodynamics and vascular alterations in an established arteriovenous fistula," *Medical Engineering & Physics,* vol. 29, *(9),* pp. 999-1007, 2007.

[69] A. M. Moerman *et al*, "The Correlation Between Wall Shear Stress and Plaque Composition in Advanced Human Carotid Atherosclerosis," *Frontiers in Bioengineering and Biotechnology,* vol. 9, pp. 828577-828577, 2022

APPENDIX A: SUPPLEMENTAL TABLES AND FIGURES

The section provides supplementary tables and figures pertaining to this study. More specific details related to the methodology and employed models can be found here. Table 8.1. provides the mesh independence analysis results performed for the 64 mm model geometry. Table 8.2. provides the mesh independence analysis results for the 51 mm model geometry. For both models a mesh size of 0.275 mm was implemented.

Table 8.1 64 mm model mesh independence analysis results.

Mesh #	Element Size (mm)	Elements	Average Element Quality	Average Skewness	Average Orthogonal Quality	Maximum Velocity at Peak Systole (cm/s)	Difference
1	0.5	248,217	0.471	0.236	0.763	31.35	-
2	0.425	363,400	0.507	0.221	0.778	31.55	0.64%
3	0.35	619,632	0.553	0.209	0.79	31.7	0.48%
4	0.275	1,243,742	0.608	0.199	0.8	31.68	-0.06%
5	0.2	2,856,699	0.662	0.195	0.804	31.8	0.38%

Table 8.2. 51 mm model mesh independence analysis results.

Mesh #	Element Size (mm)	Elements	Average Element Quality	Average Skewness	Average Orthogonal Quality	Maximum Velocity at Peak Systole (cm/s)	Difference
1	0.5	209,783	0.483	0.226	0.7774	25.6	-
2	0.425	311,378	0.517	0.214	0.785	25.82	0.86%
3	0.35	529,256	0.565	0.203	0.796	26.04	0.85%
4	0.275	1,071,531	0.617	0.196	0.803	26.23	0.73%
5	0.2	2,468,863	0.67	0.193	0.806	26.36	0.50%

Even though a more course mesh size provided results with less than 1% difference, fistula banding models with a mesh size of 0.275 mm provided the best convergence outcomes. The mesh size was chosen to make sure all model conditions were equal when comparing computational results.

Tables 8.3 and 8.4. show the results for the time step independence analysis for the 64 mm and 51 mm models, respectively, A total of 4006 timesteps were used to evaluate both models.

Table 8.3. 64 mm model time step independence analysis results.

Timesteps	Timestep Size (s)	Step Number (#)	Maximum Velocity at Peak Systole (cm/s)	Difference
2671	0.0008772	2177	31.79	-
3116	0.00075126	2542	31.83	0.13%
3651	0.000657961	2903	31.68	-0.47%
4006	0.000584873	3267	31.32	-1.14%

Table 8.4. 51 mm model time step independence analysis results.

Timesteps	Timestep Size (s)	Step Number (#)	Maximum Velocity at Peak Systole (cm/s)	Difference
2671	0.0008772	2177	26.19	-
3116	0.00075126	2542	26.24	-0.19%
3651	0.000657961	2903	26.2	0.15%
4006	0.000584873	3266	26.23	-0.11%

Table 8.5. provides the complete set of extract MRI data outputted by the in-house MATLAB codes. This data was used to create the patient specific velocity waveform, applied at the proximal artery inlet.

Table 8.5. MRI analysis MATLAB output, used to create the proximal artery velocity waveform.

Point in Cycle	Time (s)	Vessel Area (cm^2)	Velocity (m/s)	Velocity (cm/s)	Flow Rate (ml/min)	Flow Rate (cm^3/s)	Diameter (cm)	Maximum WSS (dyne/cm^2)
1	0.0260333	0.0803	0.1337	13.3701	1609.9827	26.8331	0.3197	29.8593
2	0.0520667	0.0728	0.1355	13.5497	1478.6459	24.6441	0.3044	31.7871
3	0.0781	0.0677	0.1371	13.7110	1393.0556	23.2176	0.2937	33.3355
4	0.1041333	0.0677	0.1400	14.0015	1422.5695	23.7095	0.2937	34.0417
5	0.1301667	0.0728	0.1487	14.8749	1623.2640	27.0545	0.3044	34.8960
6	0.1562	0.0728	0.1677	16.7681	1829.8612	30.4977	0.3044	39.3373
7	0.1822333	0.0702	0.1739	17.3950	1832.8126	30.5469	0.2991	41.5303
8	0.2082667	0.0790	0.1831	18.3069	2170.0088	36.1669	0.3172	41.2078
9	0.2343	0.0753	0.2018	20.1830	2278.4723	37.9746	0.3096	46.5528
10	0.2603333	0.0728	0.2191	21.9067	2390.6251	39.8438	0.3044	51.3923
11	0.2863667	0.0715	0.2230	22.2979	2391.3630	39.8561	0.3017	52.7670
12	0.3124	0.0753	0.2186	21.8562	2467.3612	41.1228	0.3096	50.4121
13	0.3384333	0.0740	0.2231	22.3131	2476.9532	41.2826	0.3070	51.9001
14	0.3644667	0.0715	0.2255	22.5456	2417.9255	40.2988	0.3017	53.3531
15	0.3905	0.0715	0.2054	20.5366	2202.4741	36.7080	0.3017	48.5990
16	0.4165333	0.0715	0.1994	19.9450	2139.0192	35.6504	0.3017	47.1988
17	0.4425667	0.0677	0.1969	19.6950	2001.0418	33.3508	0.2937	47.8844
18	0.4686	0.0715	0.1912	19.1194	2050.4775	34.1747	0.3017	45.2451
19	0.4946333	0.0753	0.1903	19.0327	2148.6112	35.8103	0.3096	43.8995
20	0.5206667	0.0753	0.1801	18.0131	2033.5070	33.8919	0.3096	41.5478
21	0.5467	0.0778	0.1772	17.7230	2067.4480	34.4575	0.3147	40.2139
22	0.5727333	0.0778	0.1724	17.2423	2011.3716	33.5229	0.3147	39.1231
23	0.5987667	0.0765	0.1720	17.1970	1973.7414	32.8958	0.3121	39.3391
24	0.6248	0.0778	0.1650	16.4959	1924.3056	32.0718	0.3147	37.4296
25	0.6508333	0.0765	0.1679	16.7856	1926.5192	32.1087	0.3121	38.3979
26	0.6768667	0.0891	0.1480	14.7970	1976.6928	32.9449	0.3367	31.3748
27	0.7029	0.0765	0.1433	14.3298	1644.6615	27.4111	0.3121	32.7801
28	0.7289333	0.0803	0.1522	15.2206	1832.8126	30.5469	0.3197	33.9920
29	0.7549667	0.0803	0.1467	14.6691	1766.4063	29.4402	0.3197	32.7604
30	0.781	0.0715	0.1439	14.3860	1542.8386	25.7140	0.3017	34.0437

APPENDIX B: IRB APPROVAL

EAST CAROLINA UNIVERSITY
University & Medical Center Institutional Review Board
4N-64 Brody Medical Sciences Building· Mail Stop 682
600 Moye Boulevard · Greenville, NC 27834
Office **252-744-2914** · Fax **252-744-2284** ·
rede.ecu.edu/umcirb/

Notification of Initial Approval: Expedited

From: Biomedical IRB
To: Veeranna Maddipati
CC:
Date: 11/5/2019
Re: UMCIRB 19-000708
ESRD-Hemodynamics-cMRI

I am pleased to inform you that your Expedited Application was approved. Approval of the study and any consent form(s) occurred on 11/4/2019. The research study is eligible for review under expedited category # 4,5,7. The Chairperson (or designee) deemed this study no more than minimal risk.

Changes to this approved research may not be initiated without UMCIRB review except when necessary to eliminate an apparent immediate hazard to the participant. All unanticipated problems involving risks to participants and others must be promptly reported to the UMCIRB. The investigator must submit a Final Report application to the UMCIRB prior to the Expected End Date provided in the IRB application. If the study is not completed by this date, an Amendment will need to be submitted to extend the Expected End Date. The Investigator must adhere to all reporting requirements for this study.

Approved consent documents with the IRB approval date stamped on the document should be used to consent participants (consent documents with the IRB approval date stamp are found under the Documents tab in the study workspace).

The approval includes the following items:

Name	Description
Consent Form	Consent Forms
Grant Application	Study Protocol or Grant Application
HIPAA-Authorizationv2.docx	HIPAA Authorization
MRI Protocol	Other Medical Procedures/Considerations
MRI Safety Questionnaire	Surveys and Questionnaires
Preparation for research.pdf	HIPAA Authorization
Research on Decedents Form	HIPAA Authorization
Waiver of HIPPA	HIPAA Authorization

For research studies where a waiver of HIPAA Authorization has been approved, each of the waiver criteria in 45 CFR 164.512(i)(2)(ii) has been met. Additionally, the elements of PHI to be collected as described in items 1 and 2 of the Application for Waiver of Authorization have been determined to be the minimal necessary for the specified research.

The Chairperson (or designee) does not have a potential for conflict of interest on this study.

IRB00000705 East Carolina U IRB #1 (Biomedical) IORG0000418
IRB00003781 East Carolina U IRB #2 (Behavioral/SS) IORG0000418